INFORMATION TO USERS

This manuscript has been reproduced from the microfilm master. UMI films the text directly from the original or copy submitted. Thus, some thesis and dissertation copies are in typewriter face, while others may be from any type of computer printer.

The quality of this reproduction is dependent upon the quality of the copy submitted. Broken or indistinct print, colored or poor quality illustrations and photographs, print bleedthrough, substandard margins, and improper alignment can adversely affect reproduction.

In the unlikely event that the author did not send UMI a complete manuscript and there are missing pages, these will be noted. Also, if unauthorized copyright material had to be removed, a note will indicate the deletion.

Oversize materials (e.g., maps, drawings, charts) are reproduced by sectioning the original, beginning at the upper left-hand corner and continuing from left to right in equal sections with small overlaps. Each original is also photographed in one exposure and is included in reduced form at the back of the book.

Photographs included in the original manuscript have been reproduced xerographically in this copy. Higher quality 6" x 9" black and white photographic prints are available for any photographs or illustrations appearing in this copy for an additional charge. Contact UMI directly to order.

UMI

A Bell & Howell Information Company
300 North Zeeb Road, Ann Arbor MI 48106-1346 USA
313/761-4700 800/521-0600

Downloaded from SHAREOK. Persistent Handle URL: https://hdl.handle.net/11244/5655

NOTE TO USERS

The original manuscript received by UMI contains pages with indistinct and/or slanted print. Pages were microfilmed as received.

This reproduction is the best copy available

UMI

UNIVERSITY OF OKLAHOMA

GRADUATE COLLEGE

ULTRAGIANT AEROSOL GROWTH BY COLLECTION WITHIN A WARM CONTINENTAL CUMULUS CONGESTUS

A Dissertation

SUBMITTED TO THE GRADUATE FACULTY

in partial fulfillment of the requirements for the

degree of

Doctor of Philosophy

By

SONIA G. LASHER-TRAPP

Norman, Oklahoma
1998

UMI Number: 9839789

UMI Microform 9839789
Copyright 1998, by UMI Company. All rights reserved.

This microform edition is protected against unauthorized
copying under Title 17, United States Code.

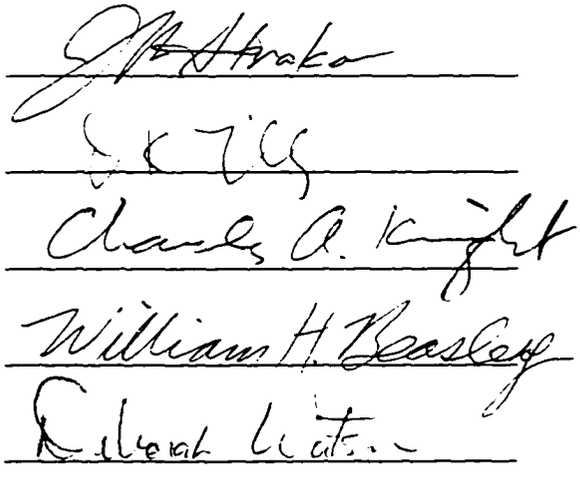
UMI
300 North Zeeb Road
Ann Arbor, MI 48103

© Copyright by SONIA LASHER-TRAPP 1998
All Rights Reserved.

ULTRAGIANT AEROSOL GROWTH BY COLLECTION
WITHIN A WARM CONTINENTAL CUMULUS CONGESTUS

A Dissertation APPROVED FOR THE
SCHOOL OF METEOROLOGY

BY



ACKNOWLEDGMENTS

During my graduate studies, I have come to learn how critical the choice of one's advisor is. I have been very fortunate to have Dr. Charles Knight of NCAR as my advisor and mentor throughout the course of this project. He has worked hard to instill in me an appreciation for the fundamentals, which has not only enhanced my critical thinking but also has helped me develop a sense of scientific intuition (a possession of his which I admire so much).

I also thank my other committee members, Dr. Jerry Straka (who has worked to keep me funded throughout this project, and to acquire the computer I needed), Dr. Doug Lilly, Dr. Bill Beasley and Dr. Deborah Watson. Their questions and comments have added strength to this study.

Dr. Rich Carpenter was very gracious in allowing me to use his nested-version of Jerry's model, as well as his analysis programs. His trajectory code was the backbone around which I built the collection model. One can accomplish more, in a shorter amount of time, if she can build on the work of others, which Rich allowed me to do.

Special thanks also go to those people at NCAR who have helped me analyze the SCMS data. I'd like to particularly mention L. Jay Miller, who supplied the PPI radar analysis software and spent quite a bit of time discussing the "ins and outs" of radar data and other data from SCMS. Rachel Ames also supplied aircraft data analysis software including ACANAL and 2D, and helped me learn to run them. Darrel Baumgardner and Krista Laursen, of RAF, were always ready to answer my questions about the aircraft data, and helped supply me with references on instrumentation. Dr. Tammy Weckworth supplied sounding and surface flux data. All

of these people helped me, putting aside their own work. Selfless acts like these make science much more enjoyable.

I also want to thank all the participants of the SCMS, who allowed me to help in the many types of data collection. Conversations in the field about science with all of you reminded me why I started down this track in the first place. And your advice on research and careers is something I'm always ready to hear.

The MMM division of NCAR supplied me with visitor's funds not only to participate in the SCMS, but also to visit NCAR five times throughout this project. Without this aid, this project would have been much more difficult, and much less fun for Charlie and myself. I heartily thank them for this support.

Funding for tuition and salary was supplied by several means throughout the course of this project. Tuition wavers were supplied by the Graduate College as a result of being named a Patricia Roberts Harris Fellow. Portions of support also came from NSF grants ATM-9311911 and ATM-9200001, and the Center for Analysis and Prediction of Storms (CAPS). The ECAS steering committee granted me time on the Cray, without which this research would not have been possible. I am grateful for all this support.

Finally, and most heartily, I thank my husband Jeff for always believing in me and lending me support, as well as my family and friends. I couldn't have made it through this process without encouragement, and all of you supplied it when it was needed, without fail. I LOVE YOU GUYS-- WE DID IT!

TABLE OF CONTENTS

	Page
Abstract	viii
1. THE ULTRAGIANT NUCLEUS HYPOTHESIS	1
1.1 Observations of Ultragiant Aerosol	2
1.2 Warm Rain Calculations Involving Giant or Ultragiant Aerosol	5
2. STUDY DESIGN AND CASE DESCRIPTION	12
2.1 Basic Design and Limitations	12
2.2 Initial Tests of Collection Models	15
2.3 The Observed Cloud	22
3. CLOUD SIMULATION	34
3.1 Cloud Model Description	34
3.2 Model Initialization and Cloud Initiation	34
3.3 Cloud Simulation Results	40
4. DESCRIPTION OF COLLECTION-TRAJECTORY MODEL	58
4.1 Numerical Technique for Solving Trajectory Equation	58
4.2 Collection Model	59
4.2.1 Collection Equation	59
4.2.2 New Packet Initialization	59
4.2.3 Spatial and Temporal Scales	60
4.2.4 Size Distribution of UGA	60
4.2.5 Collection Efficiencies	61
4.2.6 Terminal Velocity	61
4.2.7 Cloud Droplet Radii	61
4.2.8 Reflectivity Calculations	67
5. RESULTS	70
5.1 Reflectivity Evolution	70
5.1.1 Cloud water	70
5.1.2 Primary run	70

5.1.3 Noise Tests 84
5.1.3a Time Step and Packet Initiation 84
5.1.3b Simulated Fields Frequency 87
5.1.3c Packet Size and Initiation Sites 87
5.1.4 UGA Concentration Sensitivity 92
5.1.5 Cloud Droplet Radius Sensitivity (homogeneous mixing) 96
5.1.6 Cloud Droplet Concentration Sensitivity 96
5.1.7 Sensitivity to Coalescence Efficiencies 97
5.1.8 Sensitivity to Cloud Liquid Water Content 101
5.2 Raindrop Concentration 102
5.3 Drop Spectra 107
5.4 Growth Trajectories 109

6. DISCUSSION 145
6.1 General Importance of UGA 145
6.2 Discussion of Model Results 146
6.3 Extension of Model Results to Other Cumuli 147
6.4 Comparison of Model Results and Observations 149
6.5 Future Work 155

REFERENCES 157
APPENDIX A. Cloud Model Equations 161

ABSTRACT

Ultragiant aerosol (UGA) have been proposed as important initiators of coalescence in warm cumuli. When these particles are ingested at cloud base, they can immediately collect the smaller cloud droplets, thereby reducing the time needed to initiate coalescence in the cloud. Observational studies have documented the existence of UGA near the ground at concentrations greater than 1000 m^{-3}. The concentrations decrease with altitude. Whether or not these UGA concentrations are large enough to affect warm rain formation has been the subject of long-standing debate. Past modeling studies have been limited by one-dimensional treatments of the problem and inadequate observational data with which to compare the results.

The present study models the growth of UGA by collection within a cloud observed during the Small Cumulus Microphysics Study (SCMS). The observed cloud grew within a continental air mass (cloud base drop concentration ~600 cm^{-3}), reached a depth of 4.5 km and produced a 10 dBZ radar echo within 12 minutes.

The nested-grid version of the Straka Atmospheric Model is used to simulate the three-dimensional wind and cloud water fields at a spatial resolution of 50 m. The cloud simulation replicates the gross features (height of cloud base, cloud width, cloud top ascent rate) well. Within the simulated fields, "packets" of UGA are released at cloud base and grow in a Lagrangian framework by continuous collection. A history of radar reflectivity factor, as well as drop size spectra and trajectory information, is produced.

Multiple sensitivity studies are conducted, both to address uncertainties in measured (and unmeasured) quantities and to facilitate the extension of the results to other clouds. The radar echo and raindrop production are found to be very sensitive to coalescence efficiencies and cloud liquid water content.

Results suggest that UGA are only marginally important for warm rain formation in a short-lived cloud such as that studied here. Although the cloud has a very high liquid water content (> 5 g m^{-3}) and the maximum observed number of UGA are used, raindrop production is only 300 m^{-3} maximum. No drop recirculation or breakup processes enhance the production of rain in the modeled cloud, because the cloud lifetime is very short. Although little rain is produced in the modeled cloud, the reflectivity factor reaches 40 dBZ within 12 minutes, demonstrating the danger in using the radar echo alone to define significant amounts of rain, particularly when UGA are present in the cloud.

Comparison of the modeled cloud to that observed suggests UGA are not responsible for initiating the warm rain process in the study cloud. The number of UGA required to match the observed radar echo at early times produces a 40 dBZ echo at later times, when only a 10 dBZ echo was observed. An uncertainty in the observed Rayleigh echo early in the lifetime of the cloud, as well as uncertainties in the amount of UGA ingested by the cloud and the amount of cloud water present near cloud top, make this conclusion less firm. A comparison of observed and modeled raindrops shows the modeled raindrops form later and higher in the cloud than those observed, also suggesting UGA are not responsible for the warm rain formed in this cloud.

1. THE ULTRAGIANT NUCLEUS HYPOTHESIS

Rainfall is one of the most important parameters meteorologists forecast for the public, yet basic questions about rainfall formation remain unanswered. A long-standing enigma has been warm rain formation, in particular the method by which nature "bridges the gap" between the cloud droplets grown by condensation and the larger cloud drops required to initiate coalescence (and ultimately spawn rain). Simple calculations suggest the gap cannot be closed by condensation in reasonable amounts of time, so much effort has been spent discerning what complexities must be added to the calculations to explain the observed time of warm rain formation. A lack of useful observations of warm clouds and the conditions under which rain forms has only compounded the problem.

One hypothesis suggests ultragiant aerosol (UGA) may be the answer. When these large particles are ingested into the cloud, they are immediately able to start collecting smaller cloud droplets, acting as "coalescence nuclei" (Ludlam 1951, Johnson 1976, 1982). Traditionally, atmospheric aerosol (and cloud condensation nuclei) have been divided into three size regimes[1] (here using radius, R): Aitken/small ($R<0.1$ μm), large ($0.1<R<1$ μm) and giant ($R>1$ μm), but Johnson (1976) proposed another size classification, *ultragiant*, for those particles with $R>10$ μm. UGA are distinct from other sizes in that they do not require any growth by condensation in order to have appreciable collision efficiencies, particularly if they are larger than 25 μm radius. Although solubility initially speeds growth by condensation of any size particle, it is not required for UGA to begin collection immediately. Thus, UGA (soluble or insoluble) present an enticing solution to the problem of coalescence initiation in warm clouds. The feasibility of this solution depends on two issues: the

[1]Aerosol sizes discussed in this study are dry sizes. For soluble particles, the actual sizes in clear air may be the sizes of the equilibrium haze droplets, or smaller if the equilibrium has not yet been achieved.

number of UGA present in the air (particularly at cloud base), and this number being large enough to have an important effect on warm rain formation.

1.1 Observations of Ultragiant Aerosol

Woodcock (1952,1953) established the presence of giant[2] and some ultragiant sea salt particles in marine air at multiple sites around the world: the Hawaiian Islands, the coast of Australia, the Florida coast and the coast of New England. He collected these particles by exposing small glass sides from the aircraft, upon which the particles adhered, and later counted and measured the particles using a microscope in a laboratory. He documented a decrease in sea salt particle concentration with increasing altitude (Fig. 1.1), but still found some particles at and above cloud base level. Woodcock's initial chemical analyses of salt particles and raindrops suggested giant salt particles might be important in warm rain formation, which spurred interest in finding similar particles in continental air masses as well[3]. Woodcock (1952) sampled concentrations of giant and ultragiant salt particles in a maritime air mass that had moved inland 110 km into Florida, and found number concentrations comparable to those sampled over the ocean.

Much farther inland, Reitan and Braham (1954) collected particles in Illinois to evaluate the transport of salt particles inland from the coasts. They collected airborne aerosol from a ground-based site for nine months, sampling an estimated 24 m^3 per day. For aerosol greater than 10 μm in diameter (mass $>10^{-9}$ g), they reported an

---

[2]Giant sea salt particles, as well as ultragiant sea salt particles, can collect cloud droplets immediately upon entering the cloud, or very soon thereafter, because of their large equilibrium radius in a humid environment. The smallest ultragiant sea salt particle has a weight of about 10^{-8} grams, but as shown in Fig. 1, smaller particles can have an equilibrium radius in 99% humidity of 20-25 μm or larger.

[3]Woodcock *et al.* (1971) did a more robust chemical analysis comparing chlorine to iodine ratios in the salt nuclei to those in raindrops, and concluded that giant sea salt particles were not important for warm rain formation in maritime clouds as his earlier work with only chlorine had suggested. Their analysis suggested that large salt nuclei were the most important, although their study could not rule out the possibility that gaseous iodine in the atmosphere was tainting their results.

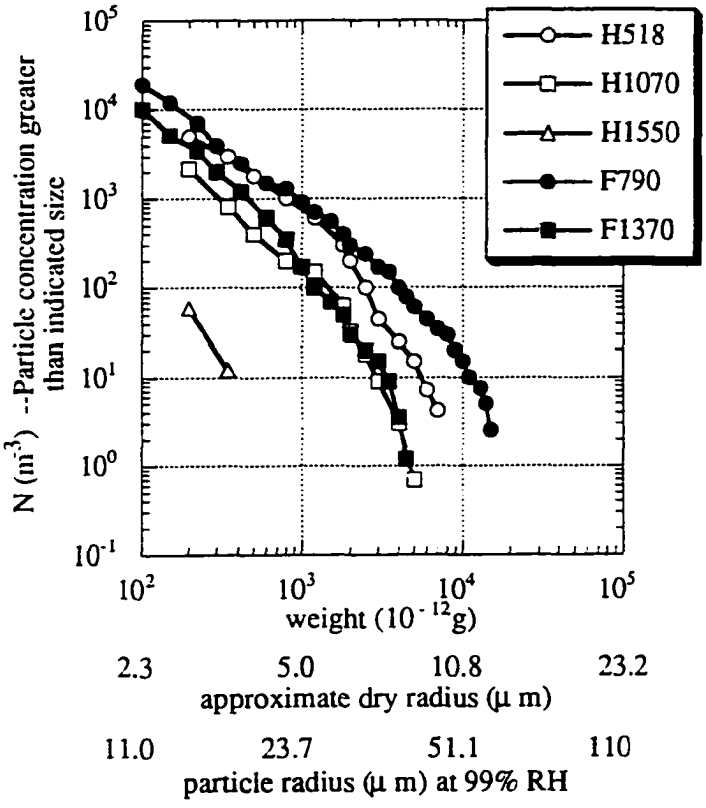


Figure 1.1 Variation of observed salt particle concentration with altitude, adapted from Woodcock (1953). Labels correspond to observations collected in Hawaii (H) or Florida (F), with numbers indicating height in meters above ocean surface where data were collected.

average daily concentration of 2 m^{-3}, with the highest daily concentration of giant and ultragiant salt particles rarely exceeding 20 m^{-3}. These concentrations are several orders of magnitude lower than those reported by Woodcock, and Reitan and Braham reasoned that giant sea salt particles probably were not important for warm rain production at such distances from the oceans.

Although giant sea salt were lacking, numerous studies documented the presence of non-hygroscopic, ultragiant particles in continental air[4]. Okita (1955) collected ultragiant, non-hygroscopic particles in concentrations of thousands per cubic meter at a ground-based sampling site 1050 m MSL in Hokkaido, Japan. Rosinski (1966,1967b) and Rosinski and Kerrigan (1969) found large numbers of insoluble, ultragiant particles in raindrops and hailstones from thunderstorms in Colorado and Nebraska. Nelson and Gokhale (1968) collected giant and ultragiant particles by aircraft in the mixed boundary layer below cloud base for three days over New York State, and found particles of mixed composition (with the primary material being non-hygroscopic) in concentrations of thousands per cubic meter for R>10 μm, and hundreds per cubic meter for R>25 μm. Noll and Pilat (1971) collected ultragiant particles from ground-based sites at various heights in the polluted air of Seattle, Washington as well as the cleaner, maritime air coming off the ocean, and found UGA to be more plentiful in the city air than in the ocean air. Johnson (1976) reported typical concentrations of aerosol (at 300 m AGL) with diameters larger than 10 μm of 7500 m^{-3} upwind of St. Louis, and 11,000 m^{-3} downwind, and for particles with diameters between 30 and 55 μm, the concentrations were 200 m^{-3} upwind and 425 m^{-3} downwind.

From the observations discussed here, some general characteristics of UGA can be summarized. They appear to be present regularly in the atmosphere in

[4]Junge (1972) notes that ultragiant, insoluble particles appear to be a feature of marine air as well.

maximum concentrations of 10^3 to 10^4 m^{-3} (Fig. 1.2); the concentration decreases as the size of the particle increases. They exist in both maritime and continental air, but are more numerous and predominantly insoluble in continental air. They are especially numerous in polluted air, suggesting anthropogenic activities can increase their number, at least locally. Their presence has been established not only near the earth's surface but also in the lower levels of the atmosphere, allowing them to be drawn into cloud base and participate in the production of rain within a cloud.

1.2 Warm Rain Calculations Involving Giant or Ultragiant Aerosol

The number of UGA present in the air has been addressed as well as current observational techniques permit, and awaits advances in instrumentation for further evaluation. The question of their importance in initiating rain, however, while having been addressed by several past studies, is now shown to deserve renewed attention.

Takahashi (1976) was motivated by Woodcock *et al.*'s (1971) negative result[3] to investigate the importance of giant salt particles in warm rain formation using a cloud model. His model incorporated elaborate microphysics (nucleation, condensation, quasi-stochastic collection, drop breakup, aerosol scavenging, salt content tracking) and simple dynamics (1-D cylindrical model at 200 m resolution). He initialized the "maritime case" with a full spectrum of sea salt particles based on Woodcock's work, terminated at a dry radius of 10 μm. For his "continental case", he used the same salt aerosol size distribution with the concentrations simply multiplied by a factor of five. Both cases were initialized with a sounding from the Hawaiian Islands. The simulated clouds were not vigorous: their depths were less than 2 km and maximum updraft speeds less than 4 m s^{-1}, although the maximum cloud liquid water contents were nearly 2 g m^{-3}. Takahashi found that when he ran the model with

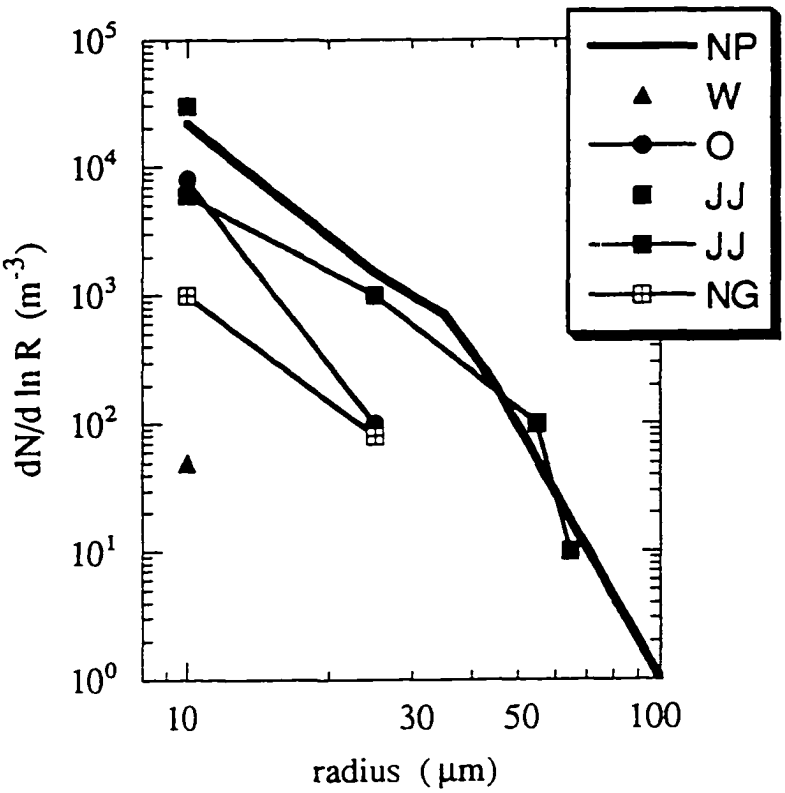


Figure 1.2 Observed concentrations of ultragiant particles sampled around the world, adapted from Noll and Pilat (1971). Legend: observations in Washington State by Noll and Pilat (NP), observations over the ocean by Woodcock (W), observations in Japan by Okita (O) , observations in Germany by Jaenicke and Junge (JJ), observations over New York State by Nelson and Gokhale (NG).

and without giant aerosol it made little difference in the amount of time to produce rain, regardless of whether the average cloud drop concentration was low (71 cm^{-3} in his maritime case) or high (350 cm^{-3} in his continental case). He reported that the giant salt particles grew by condensation to radii of about 20 μm and did not grow much further. He also stated that the smaller drops (formed by condensation on the smaller salt particles) were more effective in collecting each other (presumably because of their high number) to produce larger cloud drops, and that "the effect of giant aerosol becomes obscure within a short distance above cloud base". Presumably what is happening in his clouds is that while the giant salt particles are growing by condensation to reach sizes with appreciable collection efficiencies, the smaller and more numerous drops are forming larger cloud droplets (with higher collection efficiencies) by quasi-stochastic growth, and dominate the precipitation process. While his results shed some light on the importance of soluble, giant aerosol to warm rain formation, the importance of insoluble UGA was not addressed. Giant salt particles must undergo growth by condensation to become effective collector drops, whereas UGA can immediately start collecting droplets upon entering the cloud. Because of this difference, the importance of insoluble, ultragiant particles is indeterminable from this study.

Ochs and Semonin (1979) studied the differences in urban and rural clouds in the St. Louis area, and included the effects of UGA. They used a closed parcel model that neglected entrainment, mixing and drop sedimentation but included activation, condensation, quasi-stochastic coalescence and drop breakup. The model was initialized with a spectrum of completely soluble particles out to 80 μm radius (using Noll and Pilat's (1971) observed concentrations) and had a prescribed updraft speed of 1 m s^{-1}. During the course of their study, they found that eliminating all ultragiant particles from the CCN distribution increased the amount of time for the cloud to

attain a given reflectivity value by 300 to 400 s over a range of -15 to 30 dBZ, and removing those particles with radii between 5 and 40 μm made the most difference. When particles up to 40 μm radius were included, the model produced a 0, 10, and 20 dBZ echo in ~20, 22.5 and 24.25 min, respectively. They also found that the speed of reflectivity development was dependent upon the solubility of the UGA; decreasing their solubility from 100% to nearly 0% slowed the reflectivity growth by nearly 300 s. They attributed this latter result to the initial decrease in growth by collection, due to the smaller drop sizes from slower growth by condensation of less soluble particles. Observational evidence (refer back to Sec. 1.1) suggests these ultragiant particles are predominantly insoluble in continental air masses, and so their results for completely soluble particles are not representative. In addition, the absence of drop sedimentation in their parcel model unrealistically prolongs the influence of very large drops within the parcel (some would have fallen out before the computations stopped). For both reasons, then, the calculated reflectivity values from this study cannot be compared meaningfully with radar observations of continental cumuli.

Johnson (1982) performed the most thorough study to date on the importance of UGA to warm rain formation, showing how a 10 dBZ echo could be formed in both maritime and continental clouds in less than 20 min. He used calculated cloud drop spectra from a condensation model initialized with observed aerosol distributions extended to 100 μm radius (with realistic solubility fractions) to initialize several closed-parcel collection models. Within the collection models, he designated "small drop" and "large drop" categories to isolate the effects of the UGA on the collection process. Results from his continuous and quasi-stochastic parcel models (with a constant updraft of 2 m s^{-1}) were very similar, showing the dominance of the UGA on the calculated reflectivity. As the initial drop distribution was truncated at smaller radii, the time required for the development of the 10 dBZ reflectivity factor increased,

more drastically for the continental cases than for the maritime cases. His continuous collection trajectory model that allowed for sedimentation (the others did not) required approximately 25 minutes to develop the 10 dBZ echo, and particles with radii from 35 to 50 μm contributed the most to the reflectivity for the continental case (20 to 40 μm for the maritime case). He also found that a stronger updraft decreased the time required to produce a given reflectivity factor, and decreasing the liquid water content increased the time required. Johnson's study rectified some of the shortcomings of previous studies, such as showing the importance of including sedimentation in the calculations, and the similarity of continuous and quasi-stochastic collection when applied to this problem (although no explicit tests were reported).

Caylor and Illingworth (1987) observed large ratios of Z_{DR} to Z in cumuli scanned by a dual-polarization radar in the UK[5], and proposed the source of the large drops were UGA. To investigate the consistency of these ratios with the growth of ultragiant particles, they initialized a continuous collection model (that neglected sedimentation) with UGA from Junge (1972), and calculated the resulting ratios of Z_{DR} to Z. The calculated ratios had the same slope as the observed ratios, and so they argued that radar echo development was consistent with the growth of UGA by collection. However, they reported that the observed cumuli extended several kilometers above the freezing level, so they could not eliminate the possibility that ice in the upper parts of the cloud was melting and produced the large drops from collection during descent. Because of a lack of further information about the cloud and the simplicity of their collection model, they did not try to compare the speed of development of the Z_{DR} to Z ratio with that observed. Illingworth (1988) reported

[5] The reflectivity factor is denoted by z, equivalent to the concentration of particles per cubic meter multiplied by their diameter in mm raised to the sixth power. Z_{DR} is ten times the base-ten logarithm of z_h/z_v, where z_h is the reflectivity factor for horizontally-polarized radiation, and the z_v is the reflectivity factor for vertically-polarized radiation. When the horizontal dimension of a particle is greater than its vertical dimension, as is the case for large drops as they fall through the air, $Z_{DR} > 0$.

similar radar observations in clouds in the Tennessee-Alabama area observed during the Microburst and Severe Thunderstorm (MIST) project. Using the same collection model he found the development of the Z_{DR} to Z ratio to be consistent with that calculated from the growth of UGA. Unfortunately, this second study did not rectify the shortcomings of the first, in particular the possibility of ice as the source of the large drops.

Cooper *et al.* (1997) investigated the effects of seeding clouds with large and giant particles of potassium chloride from flares. Their adiabatic parcel model that included detailed formulations of condensation and coalescence showed that giant, soluble particles were effective in producing drizzle and precipitation much faster (after 15 minutes, only 12% of the condensate was converted to rain in the unseeded case, while for the seeded case 53% of the condensate had been converted to rain) in continental clouds. When the calculations were performed for seeding with fewer soluble particles at the large end of the giant particle regime (5 μm radius), precipitation was created even more quickly, but drizzle production was reduced, which they cited as a possibly adverse effect on precipitation production within a more realistic and longer-lasting cloud. This study provided some insight into the growth of soluble, giant particles, as that of Takahashi (1976), but did not address the issue of insoluble, ultragiant particles.

While all the studies discussed here have contributed to the base of knowledge on the effects of UGA on warm rain formation, additional progress can now be made. The standard approach of past studies has been to use detailed microphysics but simple cloud dynamics to model the coalescence process. The present study explores the ultragiant nucleus hypothesis with a different philosophy: the complex three-dimensional dynamics of a developing cumulus are included, while simplifying the microphysics as much as possible. This more detailed representation of the cloud

allows for a more rigorous comparison between calculations and detailed observations, which are now available from the Small Cumulus Microphysics Study (SCMS). Although Caylor and Illingworth have attempted to explore this realm, they had limited radar observations and still used simple parcel model calculations. The relative abundance of data collected on developing cumuli during the SCMS, along with high-resolution, three-dimensional cloud modeling capabilities, allows for a more robust study of the ultragiant nucleus hypothesis than has ever been possible.

2. STUDY DESIGN AND CASE DESCRIPTION

2.1 Basic Design and Limitations

The design of this study is to model the development of precipitation when UGA are the dominant initiators of coalescence, to better understand their potential for influencing warm rain formation. A comparison between the modeled results and observations of warm rain development within a continental cumulus is also conducted. A review of the literature in the previous chapter has shown that a study modeling the growth of UGA in a more realistic, three-dimensional cumulus cloud, and making use of extensive observations as well, is lacking. This study takes the first steps toward filling this void.

A well-observed cloud from the SCMS is selected for study, and the data are reduced to useful forms and summarized. The cloud is numerically simulated with a fully three-dimensional cloud model including bulk condensation but neglecting rain production. By varying parameters within the cloud model (discussed in Chapter 3), the simulated cloud is made to agree reasonably with aircraft and radar observations. A separate collection-trajectory model ingests the simulated cloud fields, and models the growth of insoluble UGA by the collection of cloud water along trajectories within the cloud. Specifically, "packets" of UGA are released directly below the base of the simulated cloud, where they are ingested into the cloud by the updraft. [The use of packets within a Lagrangian framework was used to investigate ice particle nucleation and growth within a developing cumulus by Knight (1990)]. The particles within each packet grow by continuous collection (justification for using the continuous collection model is presented in Section 2.2) along trajectories determined by the three-dimensional cloud winds and the fall speed of the drops. The reflectivity attributable to the cloud

water and the growing drops is calculated at one minute intervals, and compared with the observed radar echo development. Trajectory information and drop distributions within the modeled cloud illustrate the sizes of UGA most important for the evolution of the reflectivity as well as precipitation formation.

The philosophy of this study is to keep the microphysical calculations as simple as possible. Because the purpose of the modeling is so focused on the growth of insoluble UGA, several well-founded simplifications are possible. The growth of the UGA is modeled as continuous collection. Tests are presented in Section 2.2 that justify this simplification by the large difference in sizes and number concentrations between the UGA and the cloud droplets. Collection events between drops formed on UGA are neglected: the drops grow only by collecting cloud water. This simplification is justified by the paucity of UGA in the cloud. Drops formed on UGA are not permitted to influence the dynamics of the cloud. While the exact amount of drag the drops have on the buoyancy force is not calculated, estimates of the terms for cumulus convection as presented by Houze (1993) show that the temperature, pressure and vapor perturbation terms dominate the contribution by precipitation formed in these calculations.[1] Drop breakup is neglected. Spontaneous breakup is known to occur for drops greater than 4.5 mm in radius, which do not occur in the present calculations. Breakup due to collisions is not significant unless the collector drops start to collect each other, which has already been shown negligible for this study. Finally, the quasi-stochastic growth among the smaller cloud droplets is neglected. The cloud droplet radii are monodisperse (all one size) at a given height in the present framework, and so would not collect each other (except for turbulent or electrical effects, which are not included in the model).

---

[1]From Houze's estimates of these terms, a 1° temperature perturbation, a 3 mb pressure perturbation, a 3 g kg^{-1} vapor perturbation and 3 g kg^{-1} of liquid water are equivalent sources and sinks to the buoyancy acceleration. Three g kg^{-1} of liquid water is equivalent to 2-mm radius drops in excess of 50 m^{-3}, a number concentration which is never achieved in the calculations presented here.

Some limitations of this study are the unrealistic homogeneity of the simulated cloud, and the limited number of packets/trajectories. Approximating the real cloud wind and liquid water content fields by simulated fields is not ideal: the resolution of the simulated cloud is fifty meters yet real clouds have been observed to have inhomogeneities at scales as small as 1 cm (Baker 1992). Nonetheless, by using these three-dimensional cloud fields for the coalescence calculations, this study accounts for more variation within the cloud than any previous study of the growth of UGA, and thus shifts future studies toward more realistic situations. The finite number of packets/trajectories represented will undoubtedly neglect the trajectories of many individual drops, but tests presented later show a low sensitivity of the results to this simplification.

Yet another source of uncertainty is the observations themselves, but this source is small in comparison to those cited above. The uncertainty in the radar reflectivity has been determined with some confidence at 2-3 dB, but that from the aircraft-mounted instrumentation cannot be so easily quantified. Instrumentation mounted on aircraft have to sample highly inhomogeneous conditions within a cloud at speeds around 100 m s^{-1}. While calibrations of instruments can provide an estimate of measurement uncertainty, this number is usually a "best case" scenario and does not represent accurately the difficult conditions to which the instruments are subjected during a cloud penetration. Thus, the best confidence that can be had in the measurements comes from redundant measures by different instruments and physical reasoning (such as adiabatic limits), both of which are used here. Of course, the fraction of the cloud actually sampled by the aircraft is very small, so that even if the measurements were completely accurate, it is impossible to capture all the detail throughout the cloud. Thus, a "rough" agreement of the calculations with the aircraft observations is all that is practical.

2.2 Initial Tests of Collection Models

No published studies have quantified the sizes and concentrations at which different models of the collection process are valid. It is thus necessary to justify the use of the continuous collection model under the conditions of the present study. A brief review of the different types of collection models is presented first.

The simplest model of droplet growth by collection is the *continuous collection model;* all drops of the same size grow at the same rate. The discreteness of the collection process is neglected, so that collector drops can collect "fractions" of drops in a given time step as if the collected water were a continuum. A growth equation for continuous collection may be written

$$\frac{dM}{dt} = \frac{4}{3}\pi\rho_w \int K(R,r)n(r)r^3 dr \qquad (1)$$

where M is the mass of the collector drop, ρ_w is the density of liquid water, n(r) is the number concentration of the collected droplets, r is the radius of the collected droplet, and K is the collection kernel given by

$$K(R,r) = \pi(R+r)^2\left[V_t(R) - V_t(r)\right]E(R,r) \qquad (2)$$

where R is the radius of the collector drop, r is the radius of the collected cloud droplet, V_t are their terminal velocities and E is the collection efficiency[2]. The continuous collection formulation is known to underestimate the rate of growth for interactions between small droplets, where the collection kernel is very small. It is more appropriate

[2]The collection efficiency is the collision efficiency multiplied by the coalescence efficiency. Often, the coalescence efficiency is assumed unity, because of a lack of data.

when the collector drops are much larger and fewer than the collected cloud droplets, and thus is a good candidate for the present study involving UGA.

Telford (1955) introduced[3] a stochastic model of coalescence (later called the *quasi-stochastic model* by Gillespie 1975) that accounts for the random nature of drop collisions and the discreteness of droplet capture, which are both neglected in the continuous model. The stochastic collection equation (SCE) may be written as

$$\frac{dn_k}{dt} = \frac{1}{2}\sum_{i=1}^{k-1} K_{i,k-i} n_i n_{k-i} - n_k \sum_{i=1}^{\infty} K_{ik} n_i \tag{3}$$

where n_k is the number of drops of size k per unit volume, and K_{ik} is the collection kernel given by (3). The first term represents the creation of drops of size category k due to the coalescence of two drops smaller than k (the factor of one half preventing double-counting), and the second term represents the decrease in drops of size k due to coalescence with another droplet. From this equation, the importance of number concentration of drops as well as the collection kernel is evident. Even if the collection kernel is very small (as in the case of collisions between small drops), some drops will still grow very quickly if the number concentration of the collector drops is large. The continuous model has no such dependence on the number of collector drops.

Gillespie (1975) provides a more illuminating analysis of the difference between the coalescence models by showing how the quantity

$$K(R,r)n(r)dt \tag{4}$$

[3]According to Rogers and Yau (1989), this model was first applied to the problem of rain formation by Melzak and Hitschfeld (1953). However, due to poor collision efficiency data and a lack of high speed computers at their disposal (they did their computations by hand) their progress was impaired greatly. Telford is usually credited with bringing the model into the forefront of the field.

is interpreted differently in the two models. For the continuous model, (4) is the number of droplets collected in time dt by all drops of size R, even if the number is a fraction. Thus all similar-sized drops grow at the exact same rate, which is the average rate of quasi-stochastic growth. For the quasi-stochastic model, (4) is the fraction of the collector drops of size R that will collect one or more droplets of size r in time dt. Thus, some drops will grow slower than the average rate, but others will grow faster. Young (1975) presented two different formulations of the quasi-stochastic model, the discrete and the Poisson forms. The discrete model approximates the spatial distribution of the collected cloud droplets as uniform, so that (4) is interpreted as the expected (mean) number of collection events per collector drop per time step. The Poisson model allows the cloud droplets to be distributed randomly in space, so that the number of collection events per collector drop per time step is described by a Poisson distribution with its parameter given by (4). The discrete formulation is equivalent to the limit of the Poisson formulation as the time step is decreased to zero. Gillespie also presents the *purely stochastic model*, in which (4) is interpreted as the probability that any collector drop of size R will collect a droplet of size r in time dt. He shows that the quasi-stochastic model result is equivalent to the average of the results of many purely stochastic experiments.

Calculations are now presented to justify the selection of the continuous collection model as appropriate for the present study in which there are fewer and much larger collector drops collecting much more numerous, smaller droplets. These circumstances are appropriate to the situation of UGA growing by collection in a continental cumulus. Three types of coalescence models were tested: the continuous collection model, the discrete quasi-stochastic model and the Poisson quasi-stochastic model. The more accurate but computation-intensive Poisson model is only used here for insuring the accuracy of the discrete model for the time step used. The calculations

are initialized with a number of equal-sized collector drops, and the collector drops fall through an infinite column of smaller, equal-sized cloud droplets until the calculations are halted. The collector drops collect the cloud droplets but are not allowed to collect each other[4]. Each calculation quantifies the droplet growth using reflectivity factor (expressed in dBZ):

$$dBZ = 10 \log \sum_{i} N_i D_i^6 , \tag{5}$$

where N is the number concentration of the collector drops per cubic meter, and D is diameter of the collector drops in mm. The calculations are carried out for 1500 seconds. Cloud droplets are all 9 μm radius in concentrations of 400 cm^{-3} (equal to a liquid water content of 1.2 g m^{-3}). The number of collector drops is based on the observations of UGA discussed in Section 1.1. Collection events as small as 1 in 10^6 m^3 per time step are counted. Table 2.1 lists the experiments and conditions.

The plots of reflectivity factor versus time for the Poisson, discrete, and continuous collection models (Fig. 2.1) show a difference less than 1 dB in the discrete and continuous models for 15 μm collector drops: this difference increases to 3-4 dB for collector drops of 20 and 25 μm radius and then decreases again for larger collector drops. The small difference in the two models at R=15 μm is simply because the collision efficiencies are so small that little growth occurs in either model. As the collector drop size increases, the collision efficiencies increase and the difference in the models is more pronounced. By the time the collector drops are 30 μm and larger, the field of cloud droplets appears "continuous" to the collector drop, i.e., so many droplets are collected and the mass they add individually is so small that the discreteness of a

[4] This approximation was validated in independent experiments in which the collection kernels between different bins of collector drops were evaluated at each step of the calculations. This approximation often fails if the initial concentration of collector drops is greater than 10^4 m^{-3}; this limiting concentration decreases as the initial size of the collector drops increases.

Table 2.1 Initial collector drop radii (R), collector drop concentrations (N) and time steps used in collection model tests.

Model type	Initial R (μm)	N (m^{-3})	time step (sec)
Continuous	15	1000	5
Discrete	15	1000	5
Poisson	15	1000	5
Continuous	20	1000	5
Discrete	20	1000	5
Poisson	20	1000	2.5
Continuous	25	100	5
Discrete	25	100	5
Poisson	25	100	2.5 [800 sec], 0.25 [700 sec]
Continuous	30	100	2.5
Discrete	30	100	2.5
Poisson	30	100	2 [800 sec], 0.1 [700 sec]
Continuous	35	100	2.5
Discrete	35	100	2.5
Poisson	35	100	0.5 [800 sec], 0.05 [700 sec]

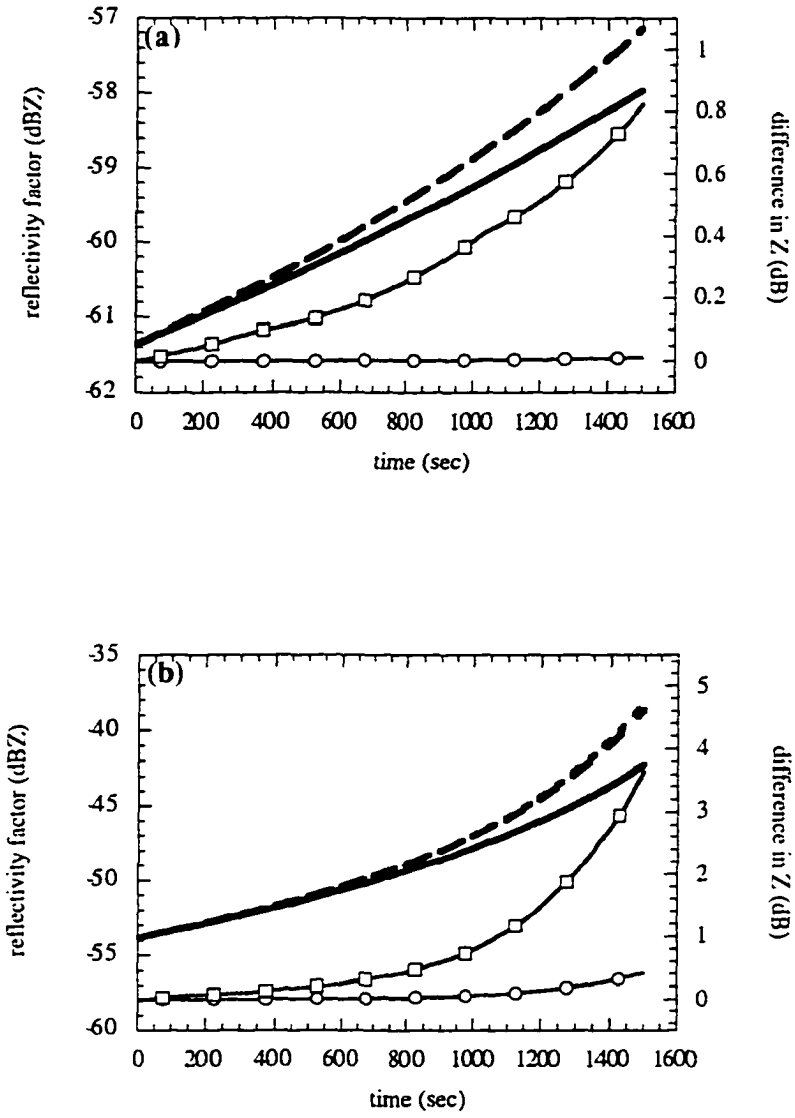


Figure 2.1 Reflectivity factor of collector drops as a function of time for three different collection models, corresponding to experiments listed in Table 2.1. Initial collector drop radii are (a) 15 μm, (b) 20 μm, (c) 25 um, (d) 30 μm and (e) 35 μm. Solid line: continuous model, long dashed line: discrete quasi-stochastic model, short dashed line: Poisson quasi-stochastic model, solid line with squares: difference in discrete and continuous model results, solid line with circles: difference in Poisson and discrete model results.

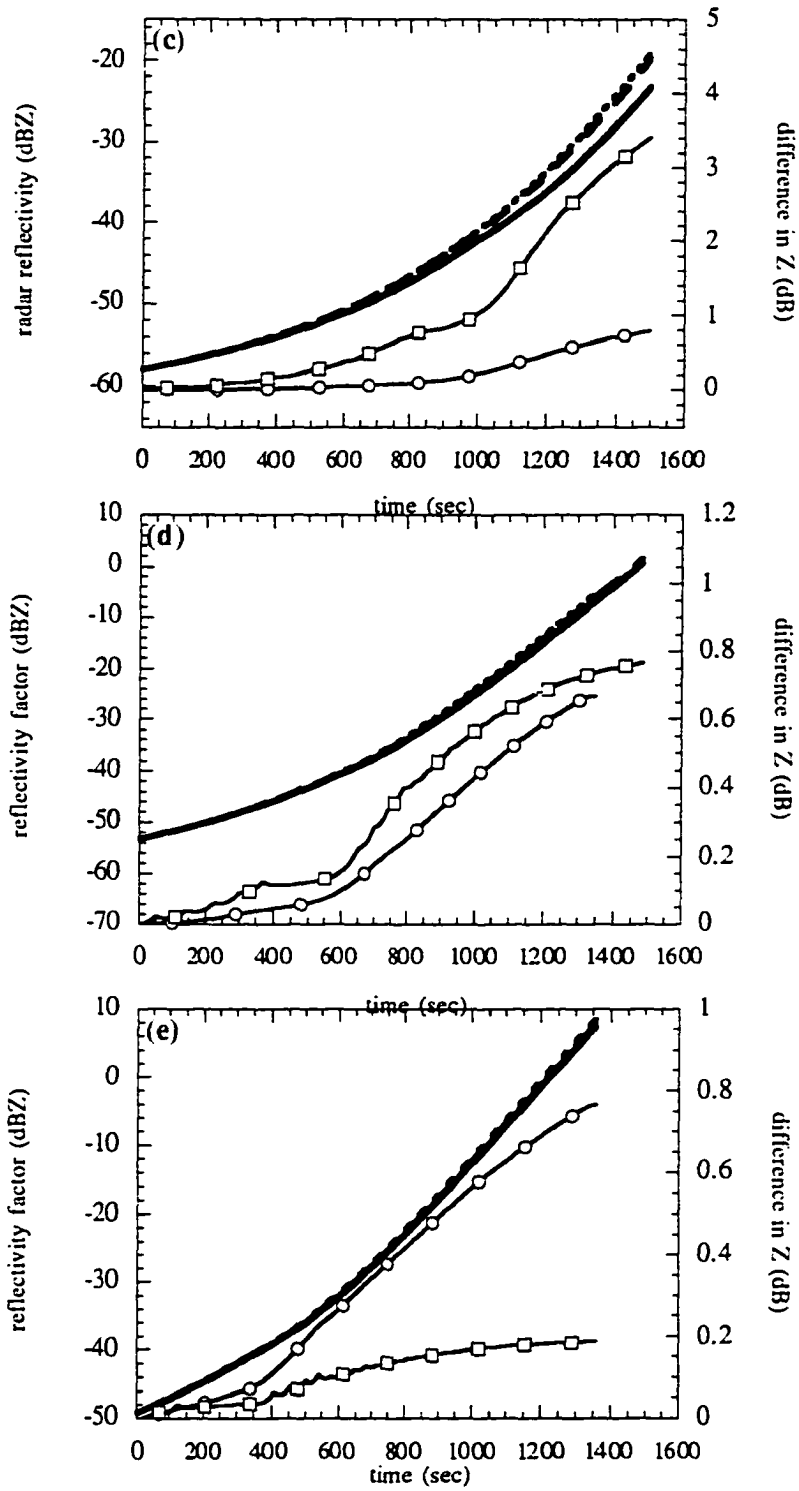


Figure 2.1 (continued)

droplet collection becomes unimportant, and the continuous model then becomes a good approximation for growth by collection. For collector drops of 30 μm radius and larger, the difference in the continuous and discrete model is less than 1.5 dB; this difference is allowable for the present study since the SCMS radar reflectivity observations themselves are only accurate to 2-3 dBZ.

A final set of experiments tests the sensitivity of the continuous collection equation to the time step. Using the simple model of collector drops falling through an infinite column of cloud droplets, a fast growing case is explored, in which truncation error might have the greatest impact. The collector drops are 50 μm in radius at a concentration of 100 m^{-3}, and the collected cloud droplets are 9 μm in radius at a concentration of 500 cm^{-3}. The results after 700 and 1500 sec (Table 2.2) show that the accumulated error is still within the error of the radar when the time step is enlarged to 5 s, and is even smaller when the calculations are carried to 700 seconds, which is nearly the duration of the calculations (720 s) used later in this study.

2.3 The Observed Cloud

The cloud selected for this study was observed during the Small Cumulus Microphysics Study (SCMS), conducted in the summer of 1995 near Cape Canaveral, Florida (Fig. 2.2) to collect data on the earliest stages of cumulus clouds. The principle goal of the study was to collect observations relevant to problems of warm rain initiation, including the onset of coalescence, the evolution of cloud droplet size distributions, and entrainment and mixing processes. This author was a participant in the field study. Data from the SCMS include reflectivity factor fields from dual-wavelength (S and X-band, or 10 and 3 cm) radar, frequent environmental soundings, time-laps video and still photographs of the clouds and wind, thermodynamic and

Table 2.2 Continuous collection model sensitivity to time step. Shown is radius of collector drops after 700 s and 1500 s, and associated radar reflectivity factor.

time step (sec)	radius (μm), 700s	reflectivity (dBZ), 700s	radius (μm), 1500s	reflectivity (dBZ), 1500s
0.5	246	-9	1781	43
1.0	245	-9	1772	43
2.0	243	-9	1757	43
5.0	237	-9	1708	42

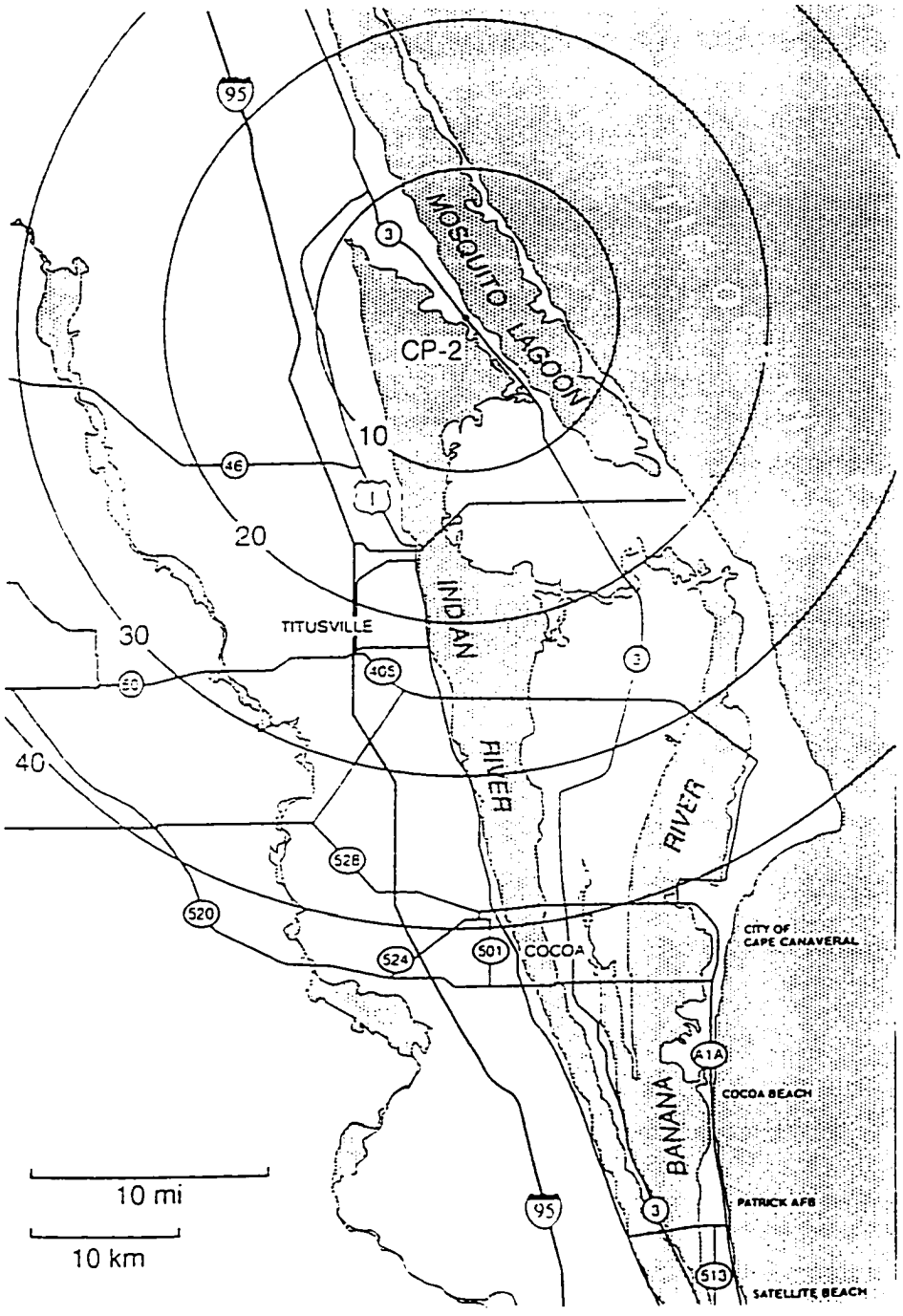


Figure 2.2 Location of the CP-2 radar on the Florida coast during the SCMS (from the SCMS operations plan, 1995).

microphysical data collected from aircraft penetrations through clouds that were synchronously scanned by the radar[5].

Dual-wavelength radar has proven useful in the past for distinguishing between radar echoes resulting from Rayleigh and Bragg scattering (Knight and Miller 1993b). Rayleigh scattering is the backscatter of the incident radiation by particles (within the cloud, water droplets) that are much smaller than the wavelength of the incident radiation, and is independent of the radiation wavelength when expressed in terms of the reflectivity factor. Bragg scattering is a constructive interference effect due to gradients in the index of refraction of the air at scales that are half of the wavelength of the incident radiation; it has a power of 11/3 dependence on the wavelength of the incident radiation (assuming the turbulence follows the -5/3 Kolmogorov law). When the difference in the radar echoes of the S and X-band radars is 19 dB, the echoes are from pure Bragg scattering, and when the difference in the echoes is 0 dB, the echoes are from pure Rayleigh scattering. Any difference in the S and X-band echoes between 0 and 19 dB is a mixture of Bragg and Rayleigh scattering, which can in theory be separated into the Bragg and Rayleigh components for each radar echo. The Bragg scattering dominates the S-band echo early in the cloud's lifetime, and particularly at the cloud edges. It is useful for determining the shape of the cloud. The Rayleigh scattering occurs within the cloud edges, often dominating the X-band echo (the Bragg scattering being much less due to the smaller wavelength) and is the echo of most interest for determining the development of cloud droplets to precipitation within the cloud. Thus, the X-band echo is used primarily in this study to indicate the development of precipitation in the study cloud.

---

[5] Additional data includes aerosol concentrations, estimated from particle probe data, from pre-cloud flight legs over the ocean; these data have proven problematic, however, and thus are not used in the present study. Future work will include an analysis of these data to determine their reliability and usefulness for estimating the concentrations of UGA present on this day.

The 1545 UTC sounding on 22 July 1995 showed a conditionally unstable environment above a well-mixed boundary layer with a superadiabatic lapse rate (Fig. 2.3). The height of cloud base estimated from the sounding was 890 m ASL (~920 mb), at a temperature of 21.7° C, and the freezing level was located at 5 km ASL. The winds from the surface up to about 2 km were mostly westerly, backing to southerly up to 6 km. No sea breeze front was present. The low-level winds had been westerly for several days due to the presence of a high pressure system in the eastern Gulf of Mexico, advecting continental air into the observation region. The maximum FSSP concentration at cloud base is approximately 600 cm^{-3}, a high number indicative of a continental air mass.

The cloud selected for study was a simple, isolated cloud. It consisted of a single turret that behaved much like a thermal, ascending and then collapsing. The S-band radar showed a strong mantle echo[6] at 1513 UTC (Fig. 2.4a), accompanied by a -20 to -15 dBZ echo on the X-band radar. The turret shot upward and developed a 0 dBZ echo around 1520 UTC (Fig 2.4b). Some uncertainty exists concerning the origin of this 0 dBZ echo on X-band radar, because the pattern matches the Bragg echo shown on S-band. If the X-band 0 dBZ echo is indeed a result of Rayleigh scattering of water droplets, a simple reflectivity factor calculation using adiabatic drop size attributes this echo to the formation of drops by coalescence[7]. By 1526 UTC (Fig 2.4c), a 10 dBZ echo has appeared and is descending within two minutes afterward. By 1531 (Fig. 2.4d) a weak precipitation shaft is extending toward the ground. Visually, the cloud's base has mostly evaporated by this time and only the upper part of the turret is visible. (Clouds were often observed to erode in this manner during the SCMS). During the

---

[6] This mantle echo originates from Bragg scattering due to index of refraction gradients at the cloud edges.

[7] The adiabatic liquid water content at a height of 4 km is approximately 5.5 g m^{-3}. So if absolutely all of this condensed water is distributed among 600 drops cm^{-3} (the average cloud drop concentration at cloud base), the radius of these drops would be 13 μm and their calculated reflectivity factor would be -7 dBZ.

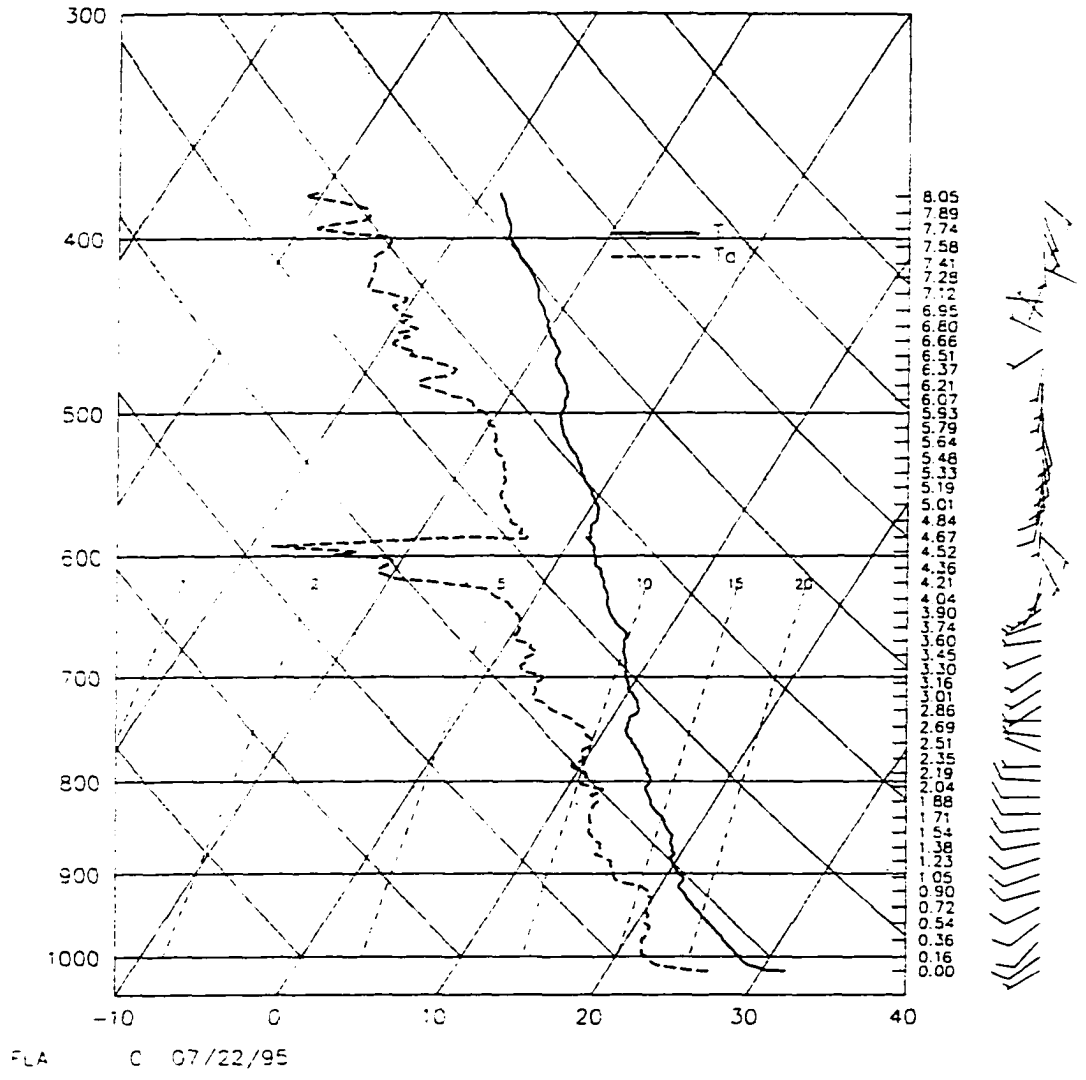


Figure 2.3 The 1545 UTC sounding on 22 July 1995, taken 20 km to the southwest of the radar.

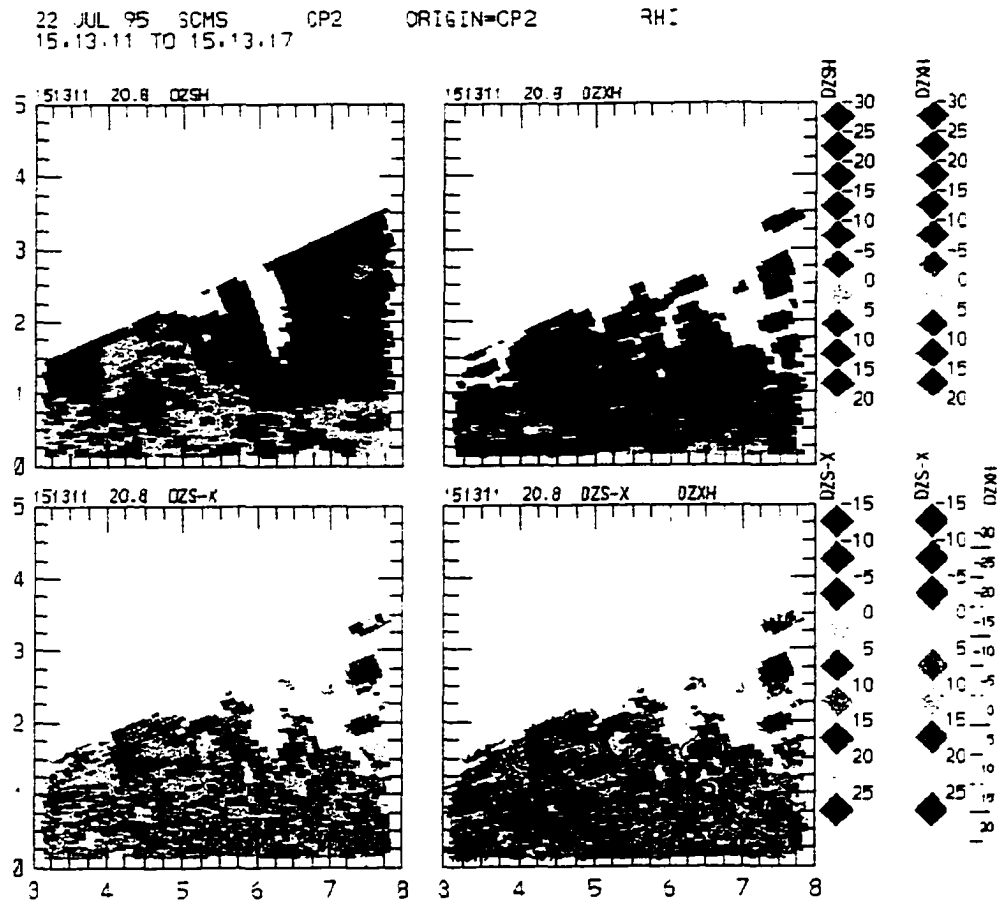


Figure 2.4a Radar echo development for the 22 July cloud: S-band radar echo (upper left), X-band radar echo (upper right), difference in S and X-band echoes (lower left), and difference in S and X-band echoes with X-band contours overlayed (lower right). Mantle echo at 1513 UTC on S-band radar.

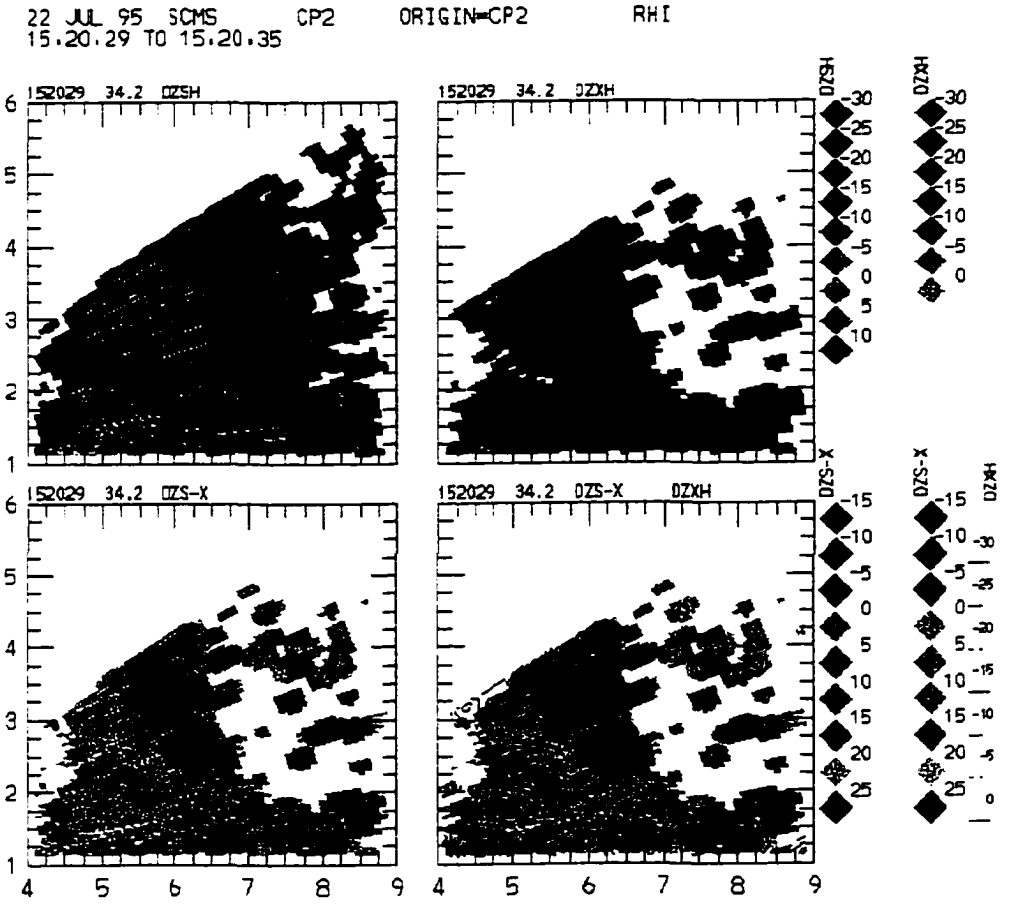


Fig. 2.4b As in Fig. 2.4a, except at 1520 UTC showing 0 dBZ echo on X-band radar.

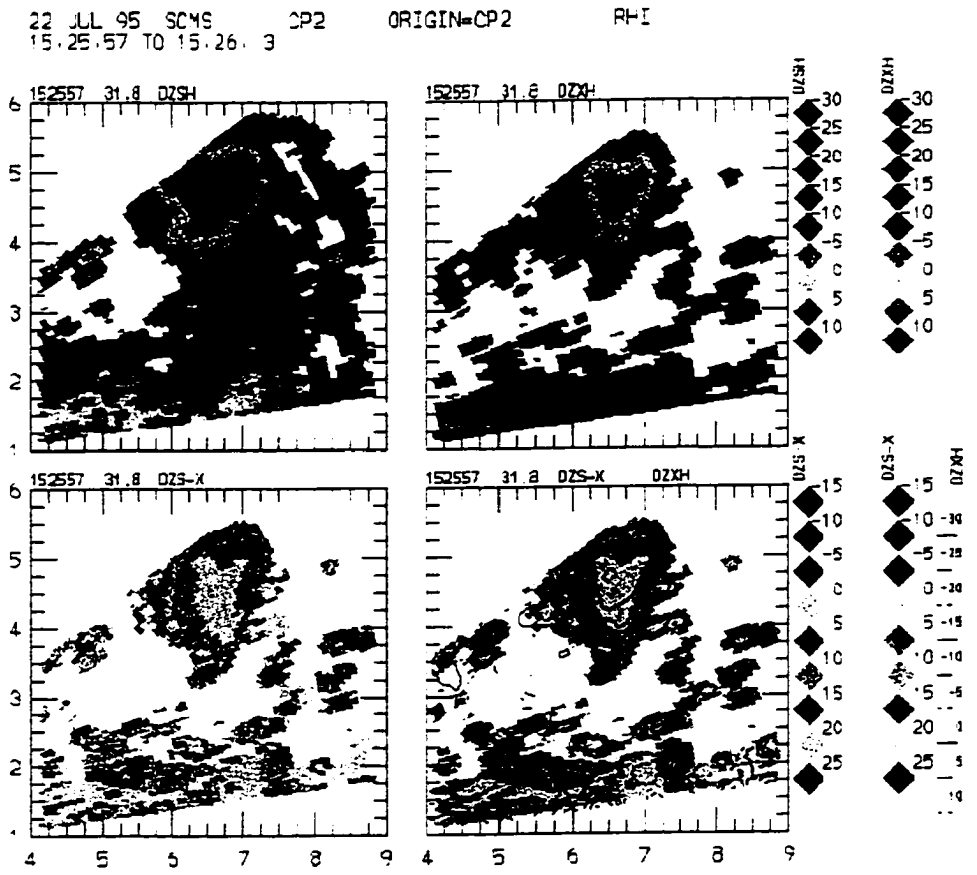


Fig. 2.4c As in Fig. 2.4a, except at 1526 UTC showing 10 dBZ echo on both S and X-band radars.

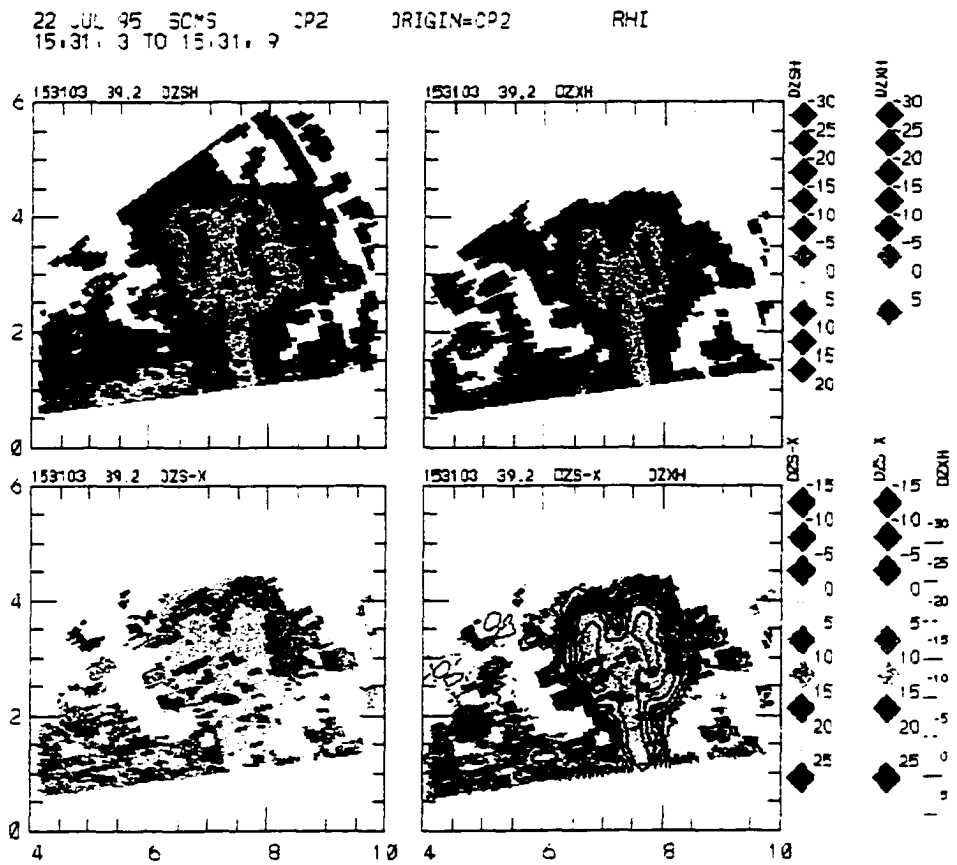


Fig. 2.4d As in Fig. 2.4a, except at 1531 UTC showing 0 dBZ precipitation shaft extending toward the ground on both S and X-band radars.

cloud's evolution, an aircraft penetrated the target cloud twice. Those measurements of updraft speed, cloud liquid water content and drop size distributions will be referenced throughout this study. A summary of the radar echo evolution and cloud penetration times is shown in Fig. 2.5.

For studying the warm rain process, clouds without any ice are desirable. The probability of substantial ice being present in this cloud is low. The maximum radar-observed cloud top height was approximately 5.5 km at 1526 UTC, and had begun its descent within two minutes afterward. According to the 1545 sounding, the temperature at this observed cloud top height was -3° C, only 500 m above the freezing level. Unfortunately no microphysical data were collected at cloud top that can be used to verify that no ice was present. From a previous field study, the Florida Area Cumulus Experiment (FACE), observations of summertime cumuli showed the region of -4 to -8° C was favorable for seeding because of the large amount of supercooled drops (Sax and Keller 1980; Hallet et al. 1978). Also, a compilation by Pruppacher and Klett (1978) of the observations of four different studies on supercooled clouds and clouds containing ice indicated that the frequency of clouds containing ice particles at a temperature of -3° C is less than 15%. Thus, from past experience gained at the same location as the study cloud, as well as the support of many other observations elsewhere, it seems likely that ice was minimal or non-existent in this cloud.

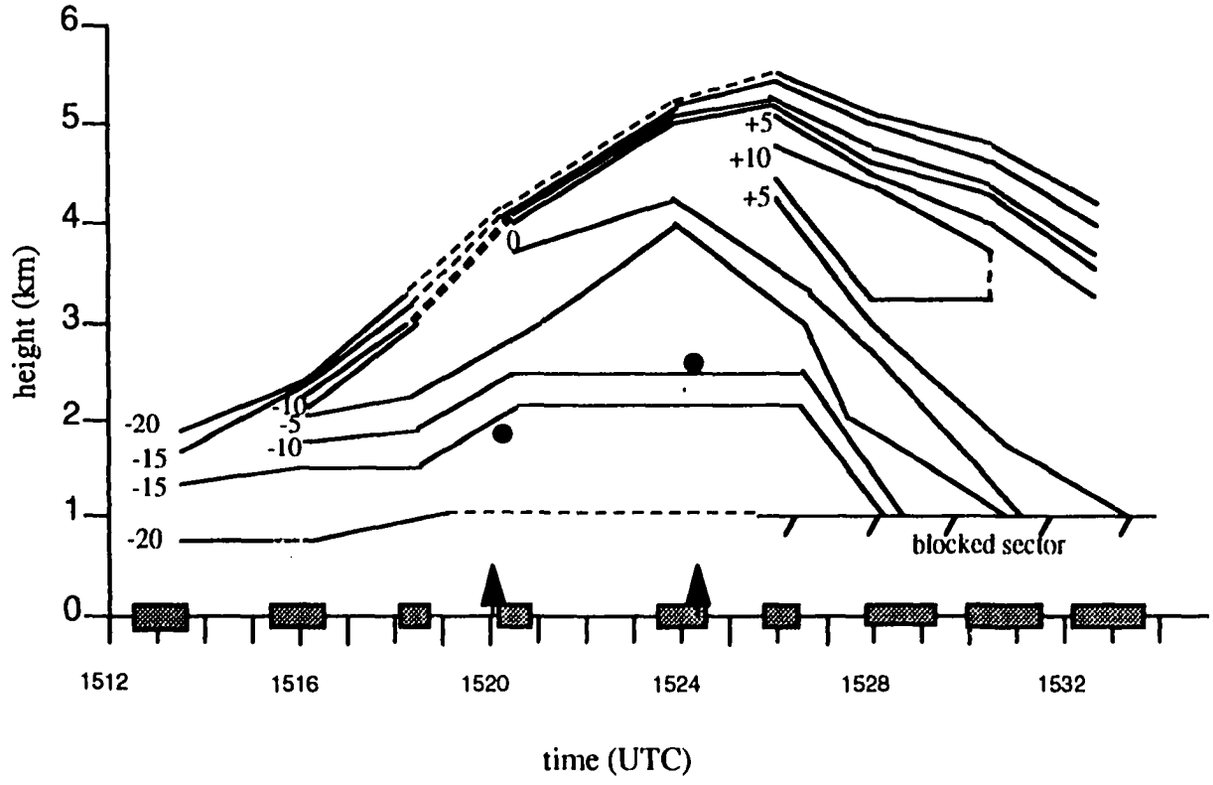


Figure 2.5 Time/height diagram of maximum echo extracted from X-band radar volumes of the 22 July cloud. Arrows denote times of aircraft penetrations and circles denote altitudes of aircraft penetrations. Grey boxes denote length of radar volume. "Blocked sector" represents an area not radiated by the radar due to restrictions from nearby Kennedy Space Center.

3. CLOUD SIMULATION

3.1 Cloud Model Description

The nested grid version of the Straka Atmospheric Model (Straka and Anderson 1993) is used to simulate the 22 July cloud. The three-dimensional cloud model solves prognostic equations for momentum, pressure, potential temperature, water vapor, cloud water and sub-grid-scale kinetic energy; model equations are provided in Appendix A. The model domain extends 8.1 km in each direction; a coarse grid covers the domain with a spatial resolution of 150 m. A fine grid nested within the coarse grid is 4 km wide and deep, and 6 km high with a spatial resolution of 50 m. The model equations are solved using a 1.5 s time step for the coarse grid, and a 0.5 s time step for the fine grid. Rigid boundary conditions are used on all 6 sides of the coarse grid, with a sponge at the top of the domain to damp vertically-propagating waves. The lower boundary condition for the nested grid is rigid; all others are interpolated from the coarse grid. Specific model schemes and constants are provided in Table 3.1 and Appendix A.

3.2 Model Initialization and Cloud Initiation

The model base state is initialized with the 1545 UTC sounding, with some modifications. The superadiabatic layer near the ground is adjusted to be nearly adiabatic. In addition, the temperature between 1 and 1.3 km is decreased by ~0.2° C to smooth out a small inversion, increasing the parcel buoyancy in the lower layers. Finally, the base state winds are set to zero, as necessary for the "rigid wall "boundary conditions on the coarse grid.

Table 3.1 Cloud model configuration and constants used in this study.

Main grid:

Computational domain: 55 x 55 x 55 grid points
Physical domain: $(8.1\ km)^3$
Model variables staggered on Arakawa C-grid
Grid spacing: 150 m
Timestep: 1.5 s, small time step 0.1875 s
Boundary conditions: rigid all six sides
Sponge: at top boundary from 6 to 8.1 km
Random velocity perturbation: at 3000 s, 0.5 m s^{-1} (maximum) every 4th gridpoint over lowest 900 m
Mean heat flux: first 3000 s only, 70 W m^{-2}
Gaussian heat flux: after 3000 s, H_G= 300 W m^{-2}, α= 100 m, σ= 1700m
Gaussian moisture flux: after 3000 s, Q_G= $1x10^{-4}$ kg m^{-2} s^{-1}

Nested grid:

Grid spawned at 4000 s
Computational domain: 81 x 81 x 121 grid points
Physical domain: 4 x 4 x 6 km
Grid spacing: 50 m
Timestep: 0.5 sec
Boundary conditions: rigid bottom, all others obtained from main grid
Spatial interpolation: parabolic scheme of Clark and Farley (1984)
Temporal interpolation: linear
Random velocity perturbation: 0.2 m s^{-1}(max) every 4th gridpoint at time of spawning, throughout entire grid

Both grids:

Sound wave integration: mode-split and super-compressible. c_s= 150 m s^{-1}
Momentum advection: box method, leapfrog in time
Scalar advection: 6th-order Crowley scheme, forward in time
Constants for subgrid turbulence parameteriztion: C_ε= 0.7, C_k= 0.09, Pr_t=0.44
Microphysics: Simple bulk condensation (Soong & Ogura 1973) no rain
Computational diffusion: 6th order , 2% of maximum allowed by stability analysis

Carpenter (1994) (hereafter, C94) suggested a special initialization procedure for producing a flat cloud base, and simulating cloud entrainment better than in previous studies. For the first hour of his simulations, C94 placed at the bottom of the domain four Gaussian-shaped heat fluxes that decayed with height (as well as a horizontally-uniform component which also decayed with height) to create four vigorous clouds. These clouds and their associated motions produced an adiabatic lapse rate and a constant water vapor mixing ratio within the boundary layer, and also produced a turbulent environment throughout the model domain. After this one-hour initialization period, the four "hot spots" were terminated, and a weaker Gaussian heat flux was placed in the center of the domain to produce the desired cloud for study. C94 was able to produce a realistic-looking cloud with a flat base that entrained more environmental air with this procedure.

C94 's procedure is used in the present study, with some modifications. Initiating the four vigorous clouds during the initialization period for the present case proved problematic. The Florida sounding used here is much more humid than the New Mexico sounding used by C94; as a result the four initial clouds took a long time to evaporate, and by the time they had, the motions they had introduced into the upper parts of the model domain had long before dissipated. As a substitute to the four initial clouds, random velocity perturbations were introduced into the boundary layer directly before initiating the study cloud, to introduce motion quickly at small scales, within the source region of the study cloud. This substitution worked well, as will be seen in the simulation results later.

Before initiating the cloud, the model is run to mix the boundary layer for producing a flat cloud base. For 3000 s, a horizontally-uniform heat flux (70 W m^{-2} maximum) that decays exponentially with height (equation (6) with $H_G=0$) is turned on, to produce an adiabatic lapse rate in the lowest levels. The modeled "base-state"

atmosphere after the initialization period is shown in Fig. 3.1. Although the mixing ratio is not constant in the boundary layer, the cloud base only fluctuates by about 50 m during the 12-minute period of interest. (In hindsight, the sounding input into the model could just have been adjusted manually to create a boundary layer with an adiabatic lapse rate and a constant water vapor mixing ratio and the observed cloud base height). The cloud is then initiated into this pre-conditioned atmosphere. A random velocity perturbation (magnitude between $\pm$ 0.5 m s^{-1}) is added to all three wind components every fourth grid point (450 m apart) within the lowest 900 m of the domain. These perturbations introduce asymmetries into the boundary layer flow. A strong Gaussian heat flux is applied at the center of the domain (within the boundary layer) as a source for the cloud (after C94):

$$H = \left[H_o + H_G \exp\left(-\frac{(x - x_o)^2 + (y - y_o)^2}{\sigma^2} \right) \right] \exp\left(-\frac{z}{\alpha} \right) \qquad (6)$$

where H_G is 300 W m^{-2}, x_o and y_o are the coordinates at the center of the domain, σ is 1700 m, and α is 100 m. A similar equation describes the moisture flux in the boundary layer, where H_G is replaced by Q_G and has a value of 1×10^{-4} kg m^{-2} s^{-1}. At 4000 s, the fine grid is inserted within the coarse grid, to capture more detail within the cloud and perhaps simulate entrainment more realistically as suggested by C94. The nested grid is also initialized at the lowest levels with a random velocity perturbation (maximum magnitude $\pm$ 0.2 m s^{-1}) to increase the turbulence within the boundary layer from which the cloud emerges.

Three characteristics of the simulated cloud are monitored: cloud top (and its ascent rate), maximum updraft speed, and maximum cloud water. These characteristics are most important for the collection calculations performed later. After some experimentation with the strength of the Gaussian heat and moisture

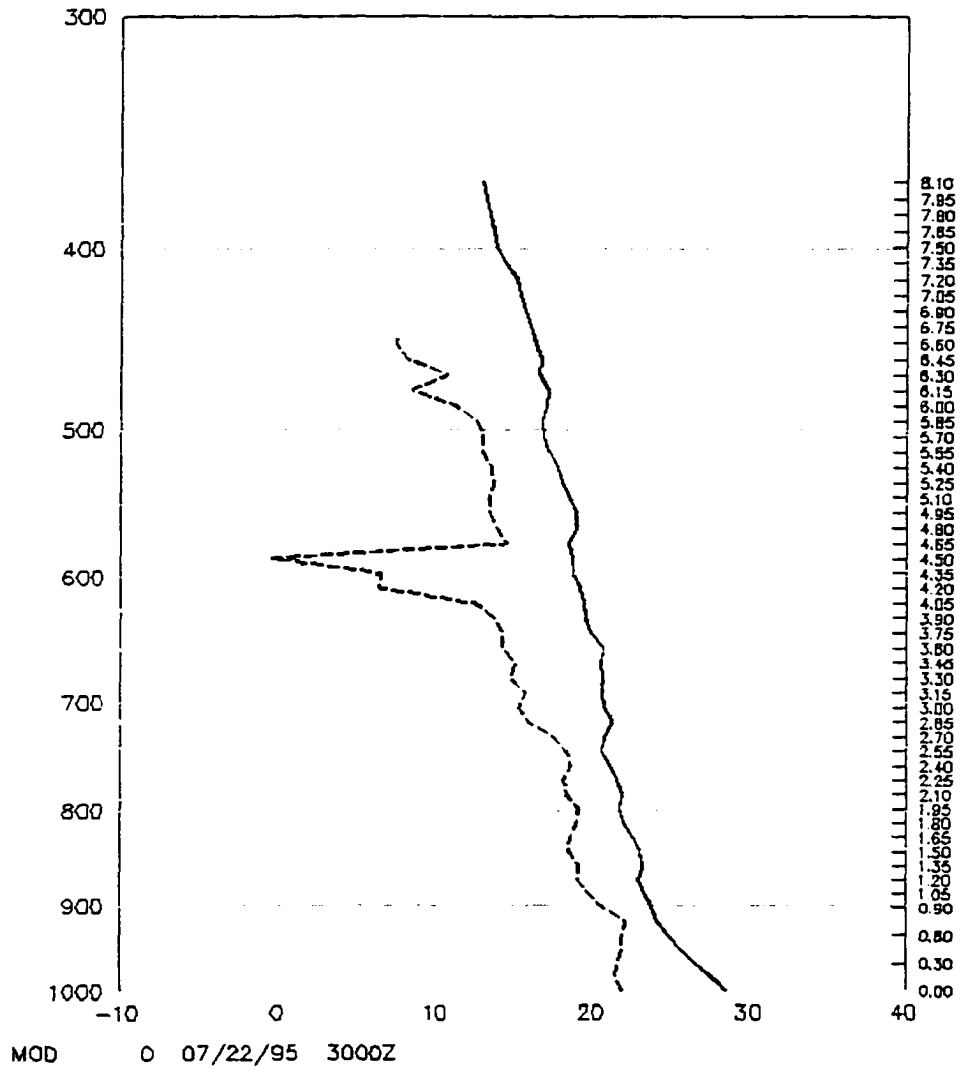


Figure 3.1 Cloud model environment sounding, after adjustments to the 1545 UTC sounding and a 3000 s initialization period.

fluxes, the simulated cloud top ascent rate matches the observed rather well (shown in Section 3.3), but the updraft speed seems high (>20 m s^{-1}), as well as the cloud water mixing ratio (> 8 g kg^{-1}), probably due to insufficient simulation of entrainment (although no observations near cloud top exist for verification).

In an attempt to increase the entrainment, some experimentation has been performed with the turbulent Prandtl number[1] used in the cloud model, over the range of 1/3 to 1 that is commonly quoted in the literature. The value used is 0.44, which is the value used by C94. When the turbulent Prandtl number was decreased to 1/3 (thereby increasing the conversion of energy to the subgrid scales for scalars, that then feeds back into the velocity as well), the cloud water and updraft speed were reduced, but the cloud lost its turbulent appearance and the cloud water field was very smooth as well. Increasing the turbulent Prandtl number had the opposite effect, making the cloud appear very turbulent, but the magnitudes of the updraft and cloud water were even higher.

Futher experimentation was performed with some of the parameters in the turbulence formulation, particularly in the equation for the eddy mixing coefficient (K_m), to increase the turbulent mixing and thereby reduce the magnitudes of the updraft speed and cloud water. Increasing C_m in equation (A9) in Appendix A increases the buoyancy and shear production of K_m while decreasing the dissipation of K_m; both effects increase the "drain" of energy to the subgrid scales. Increasing C_ε increases the dissipation of K_m, thus decreasing the conversion of energy to the subgrid scales. Using a value of C_m= 0.09 and C_ε=0.7, with a turbulent Prandtl number of 0.44, maintained the agreement between the simulated and observed cloud top ascent rate, slightly reduced the maximum updraft speed and liquid water content,

[1]The turbulent Prandtl number is the ratio of the eddy mixing coefficient for momentum, K_m, to the eddy mixing coefficient, K_h (refer to equations A6 and A7).

and preserved the turbulent cloud appearance. These values give the most favorable results for the desired cloud characteristics.

3.3 Cloud Simulation Results

The modeled cloud is a vigorously growing turret (Fig. 3.2), with dimensions similar to the observed cloud. Throughout the simulation, cloud base (here defined as cloud liquid water content of 0.001 g m^{-3}) is between 1 and 1.05 km, only 100-150 m higher than that estimated from the ground-based sounding. The maximum cloud top height during the simulation is 5.6 km, agreeing well with the 5.5 km estimated from radar data. A comparison of cloud top ascent rate between the modeled cloud and that observed on radar shows encouraging agreement (Fig. 3.3), with the modeled rate being only slightly steeper. The modeled descent rate differs from that observed more, but the collection calculations are terminated before the cloud top begins its descent. The width of the simulated cloud is approximately 2 km, also similar to that observed on radar.

The vertical velocity field of the simulated cloud is that expected of a single, localized turret. In the early part of the simulation, the cloud is primarily one big updraft, with slight downdrafts occurring directly outside the cloud (Figs. 3.4 a,b). The maximum updraft speed during the lifetime of the cloud is 22.5 m s^{-1}, which is below the maximum of 29 m s^{-1} estimated from the CAPE in the lowest 5 km of the input sounding. As the turret ascends and entrainment becomes more substantial, the cloud exhibits regions of updraft and downdraft throughout (Fig. 3.4 c). At the time of maximum cloud top height (Fig. 3.4 d), downdrafts dominate the upper two thirds of the cloud and the cloud begins its demise. (The updrafts near the bottom of the cloud at this time represent new growth occurring from the surface heat flux that is still on).

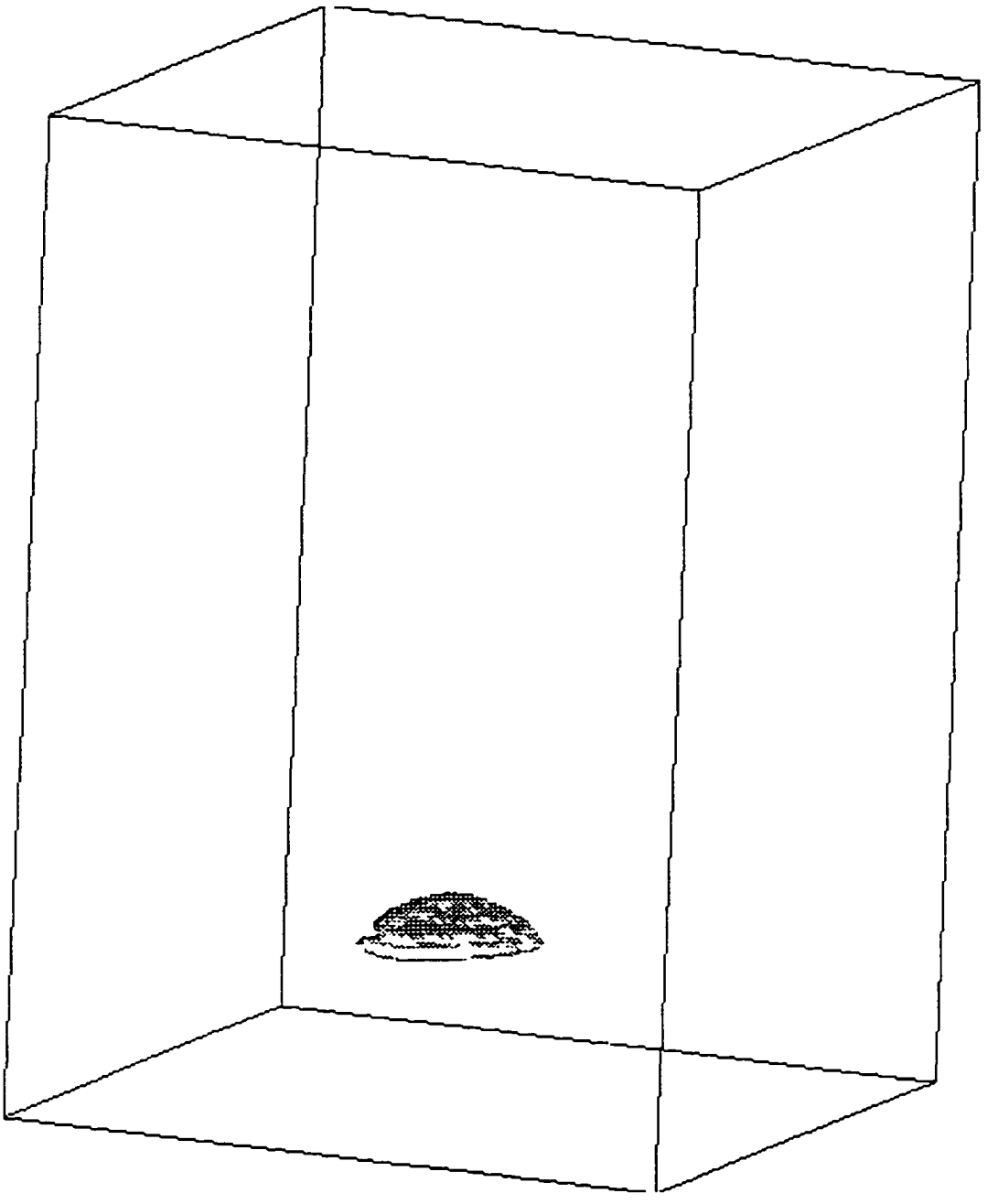


Figure 3.2 Evolution of the simulated cloud at 2 minute intervals, from two to twelve minutes. Shown is the 0.001 g kg^{-1} cloud water mixing ratio surface, as illuminated by an exterior light.

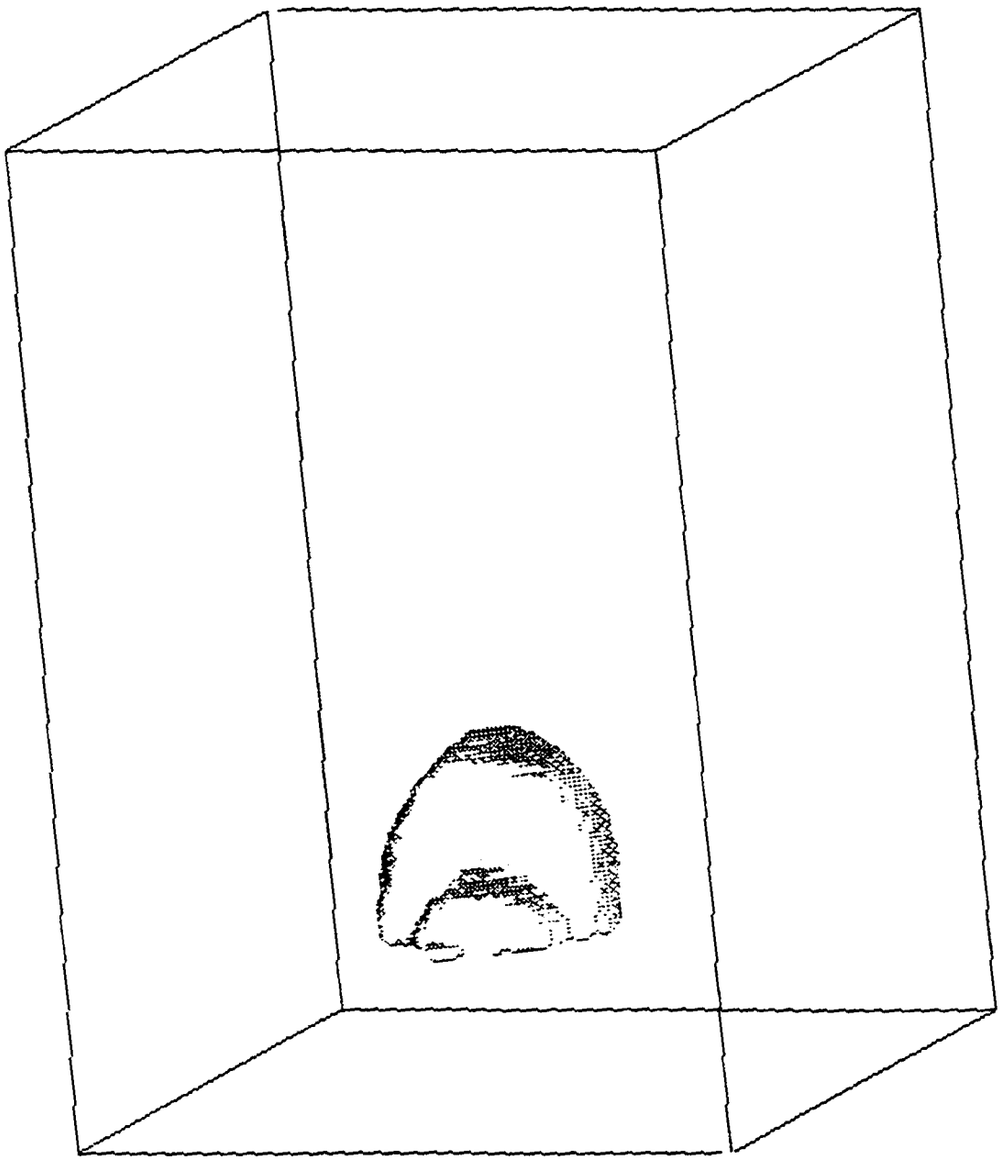


Figure 3.2 (continued)

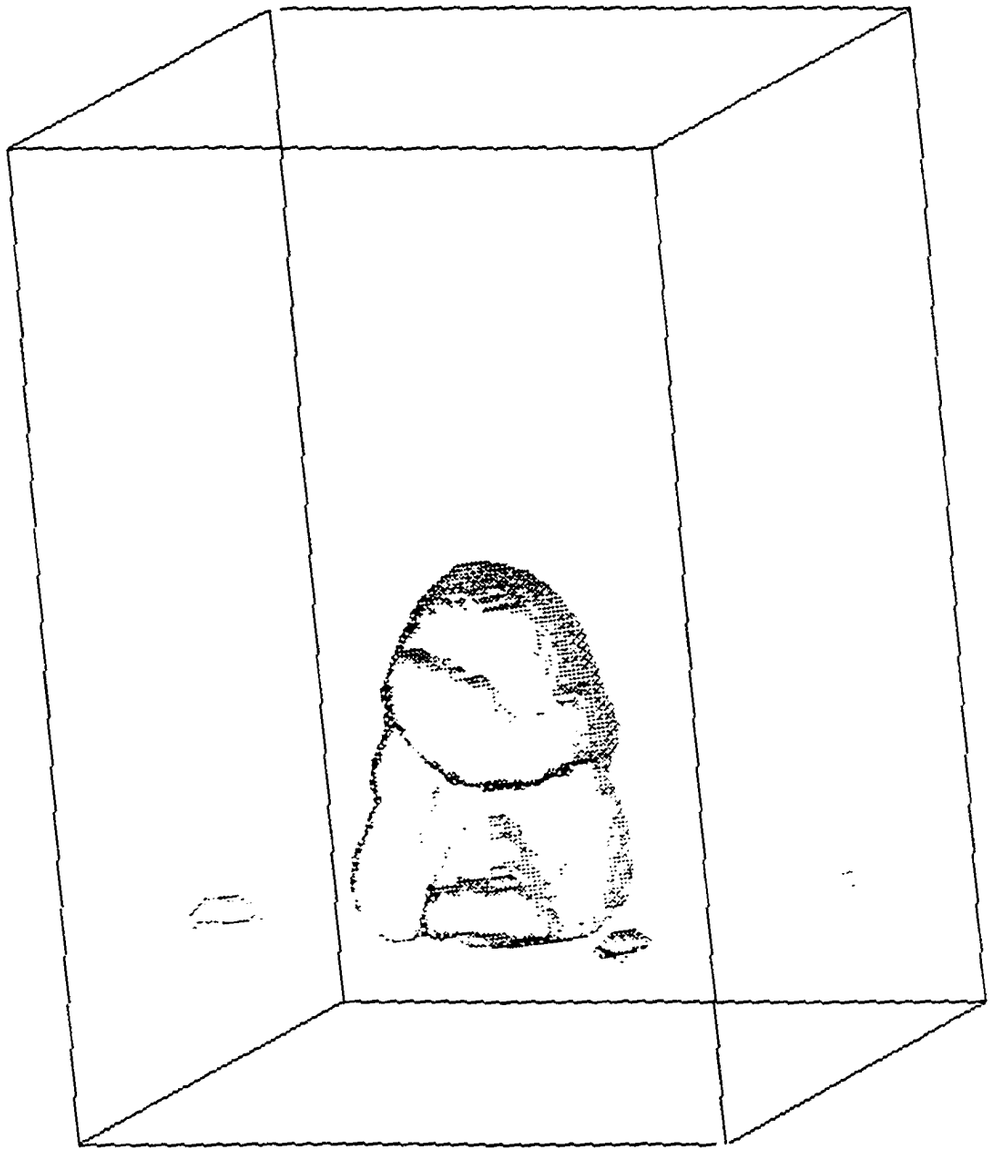


Figure 3.2 (continued)

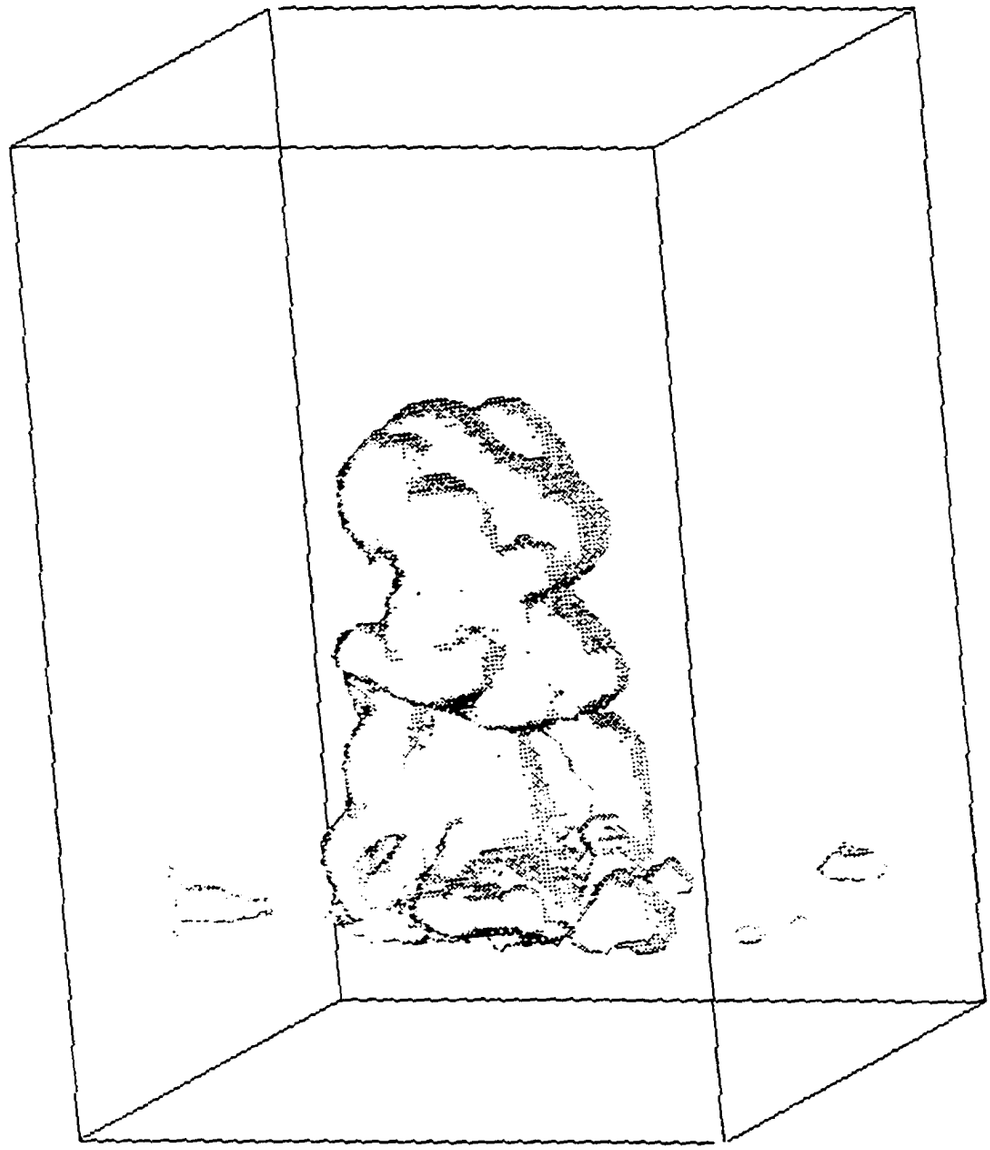


Figure 3.2 (continued)

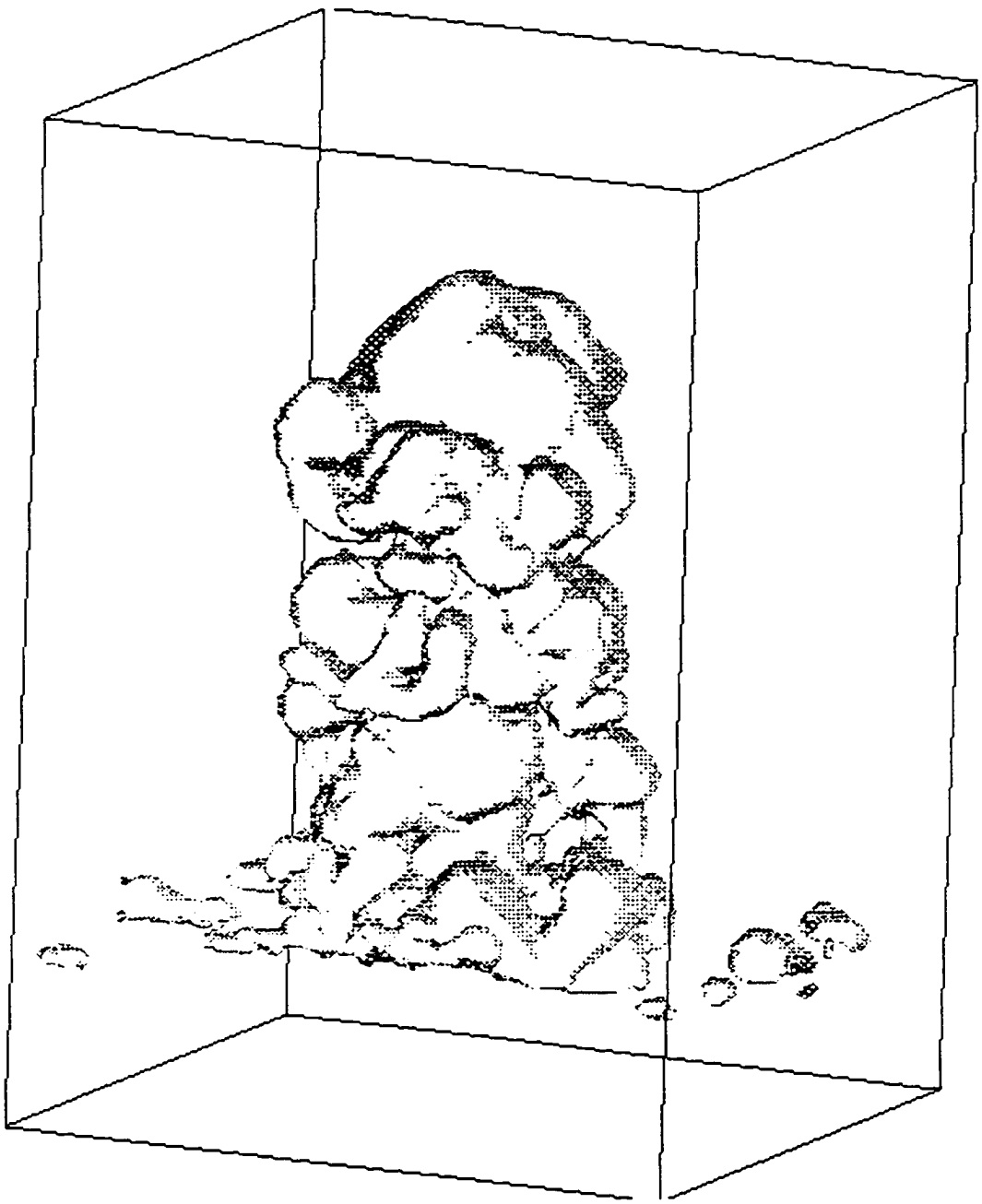


Figure 3.2 (continued)

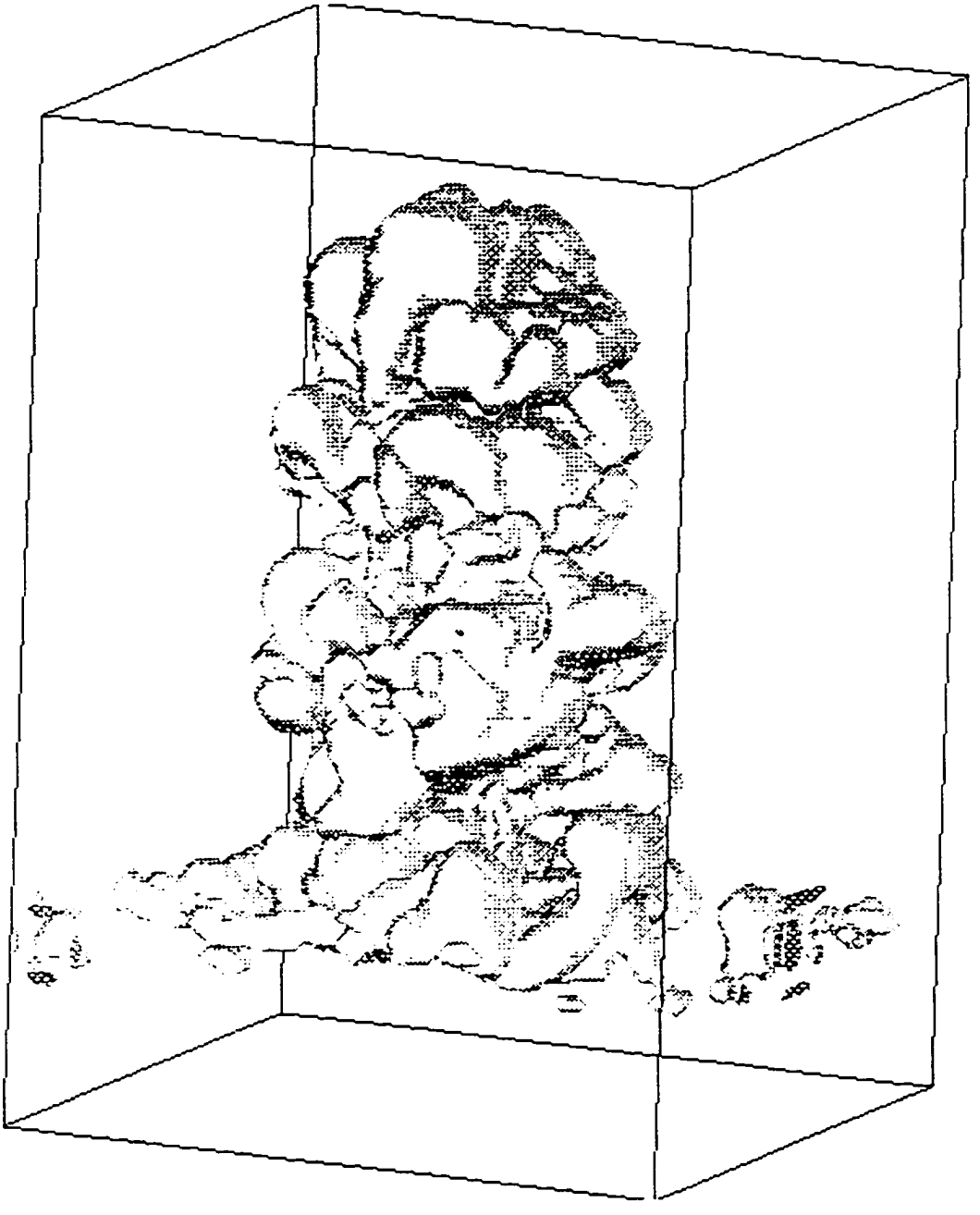


Figure 3.2 (continued)

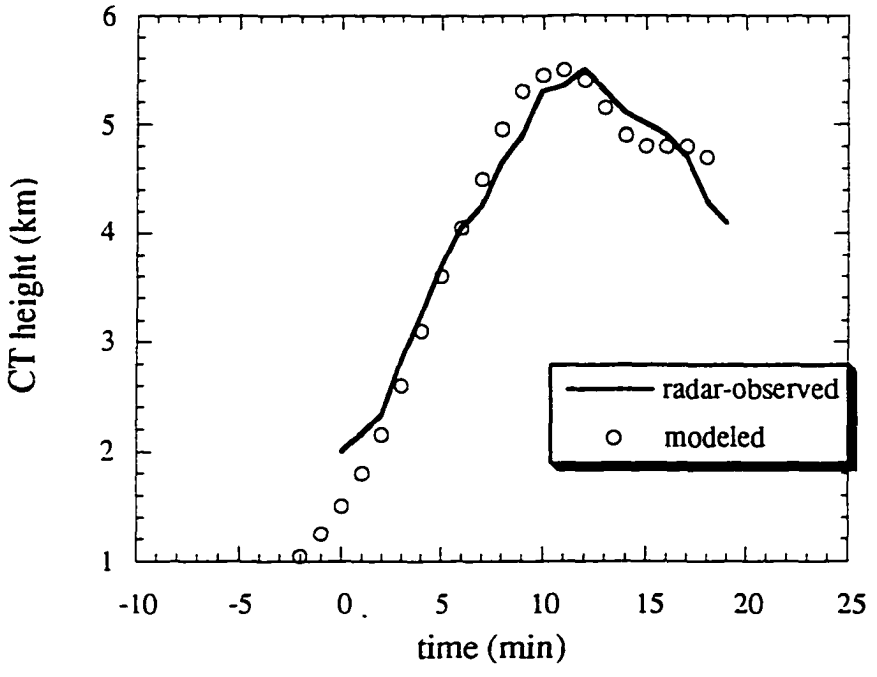


Figure 3.3 Cloud top height as a function of time, simulated and radar-observed.

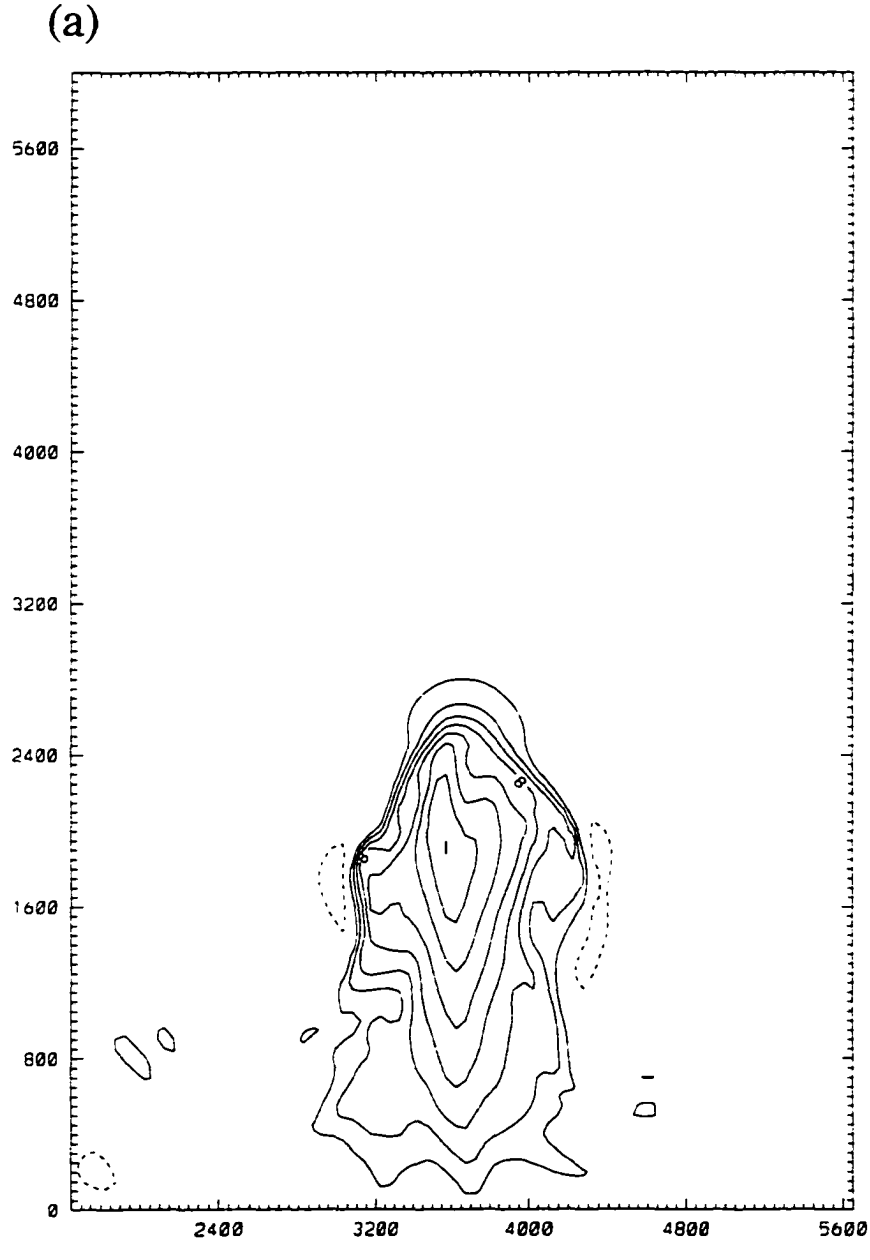


Figure 3.4 Vertical cross-sections of simulated vertical velocity (m s^{-1}) at (a) 4 minutes, (b) 7 minutes, (c) 11 minutes and (d) 12 minutes. Solid contours denote upward motion and dashed contours denote downward motion (zero contour not plotted). Contour interval is 2 m s^{-1}. Axes are distance in meters.

(b)

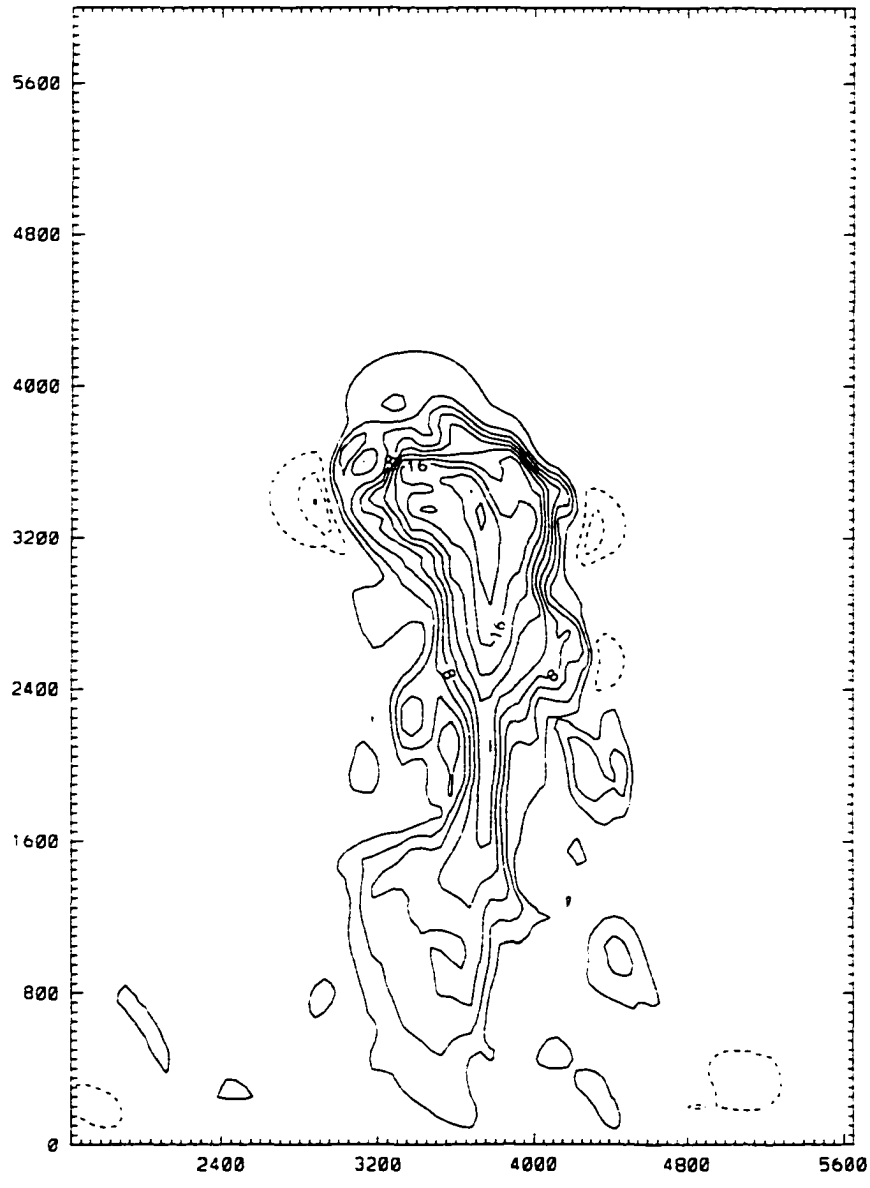


Figure 3.4 (continued)

(c)

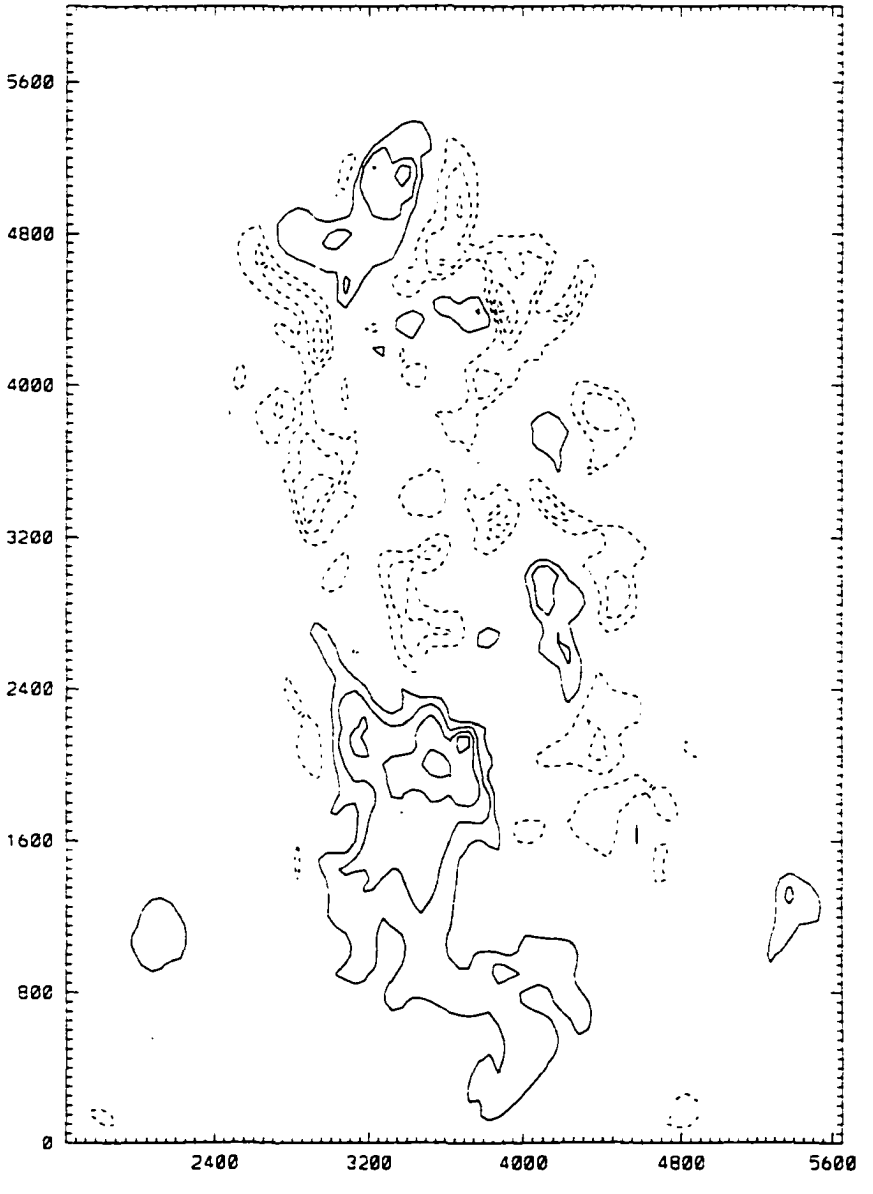


Figure 3.4 (continued)

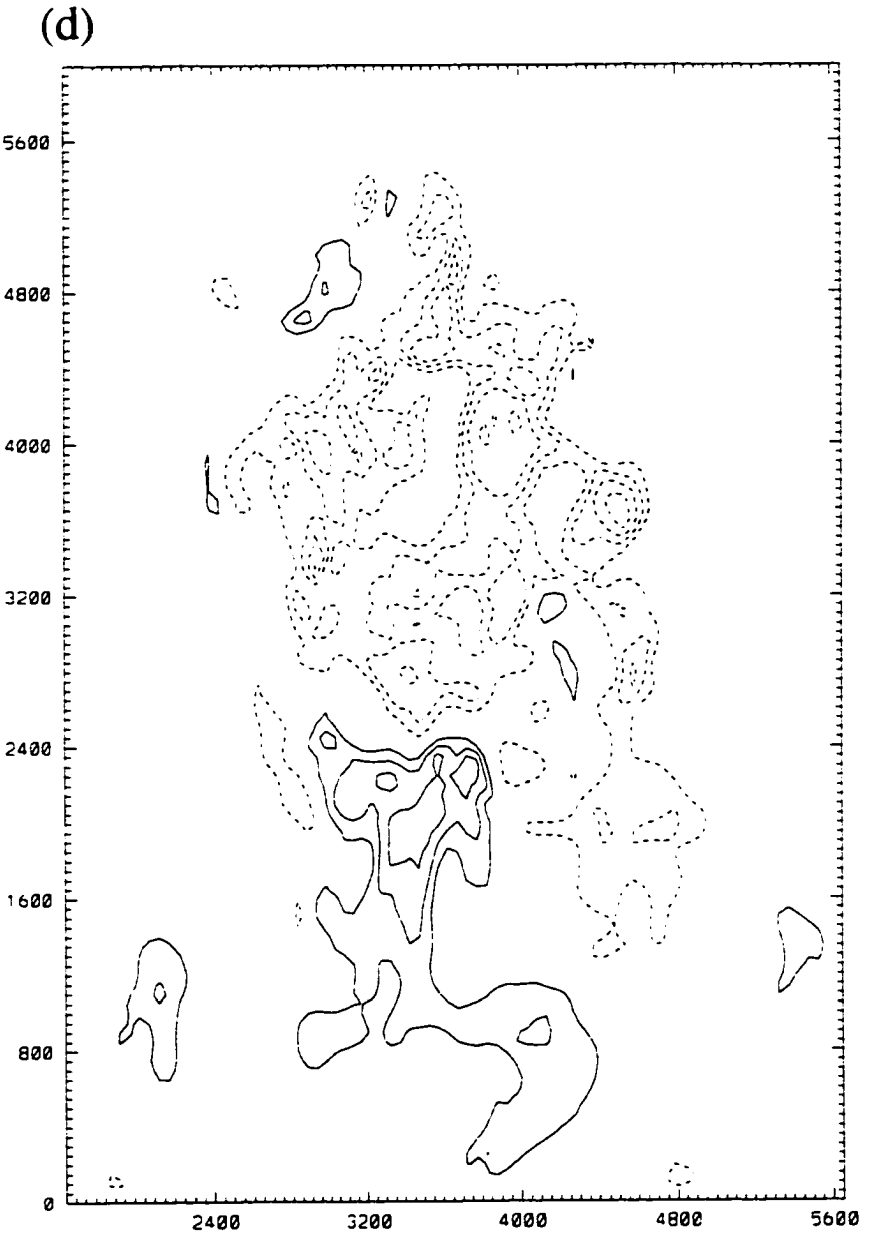


Figure 3.4 (continued)

The modeled updraft speed is in reasonable agreement with that measured during penetrations through the observed cloud. The maximum updraft speed measured at the time of the first penetration was 8 m s^{-1}. Comparing this observation to the modeled cloud at the time when the modeled and observed cloud top heights are in agreement, the modeled cloud has a very localized maximum of 10 m s^{-1} at the height corresponding to the penetration. A similar comparison between the modeled cloud updraft and that measured during the second penetration shows a similar difference of 2 m s^{-1}.

The simulated cloud liquid water content (Fig. 3.5) evolves as expected of a thermal starting from rest (Sánchez et al. 1989), with entrainment becoming more important as time progresses. Early in the simulation the liquid water content is small and very near its adiabatic value (Fig. 3.5 a), but the effects of entrainment soon become evident at the cloud edges (Fig. 3.5 b). At later times (Figs. 3.5 c,d) the cloud water maximum near cloud top is less than its adiabatic value with no adiabatic pockets visible. The modeled cloud erodes at the mid-levels first, where very dry air in the environment at that altitude (refer back to Fig. 2.4) has mixed with the cloudy air and evaporated the cloud water. The observed cloud was noted to decay from the base upward, as was observed often in clouds during the SCMS. (Note that the modeled cloud has new development at cloud base, unlike the real case, because the cloud forcing is never shut off. As stated earlier, the collection calculations are halted before this new growth can contaminate the results).

The simulated cloud liquid water content is probably greater than that which occurred in the real cloud. The maximum cloud liquid water content near cloud top is greater than 5 g m^{-3}. The aircraft penetrations for this cloud were never made at the upper levels of the cloud. Sax and Keller (1980) reported finding 3-3.5 g m^{-3} during penetrations near cloud top of cumulus congestus in Florida, although these values

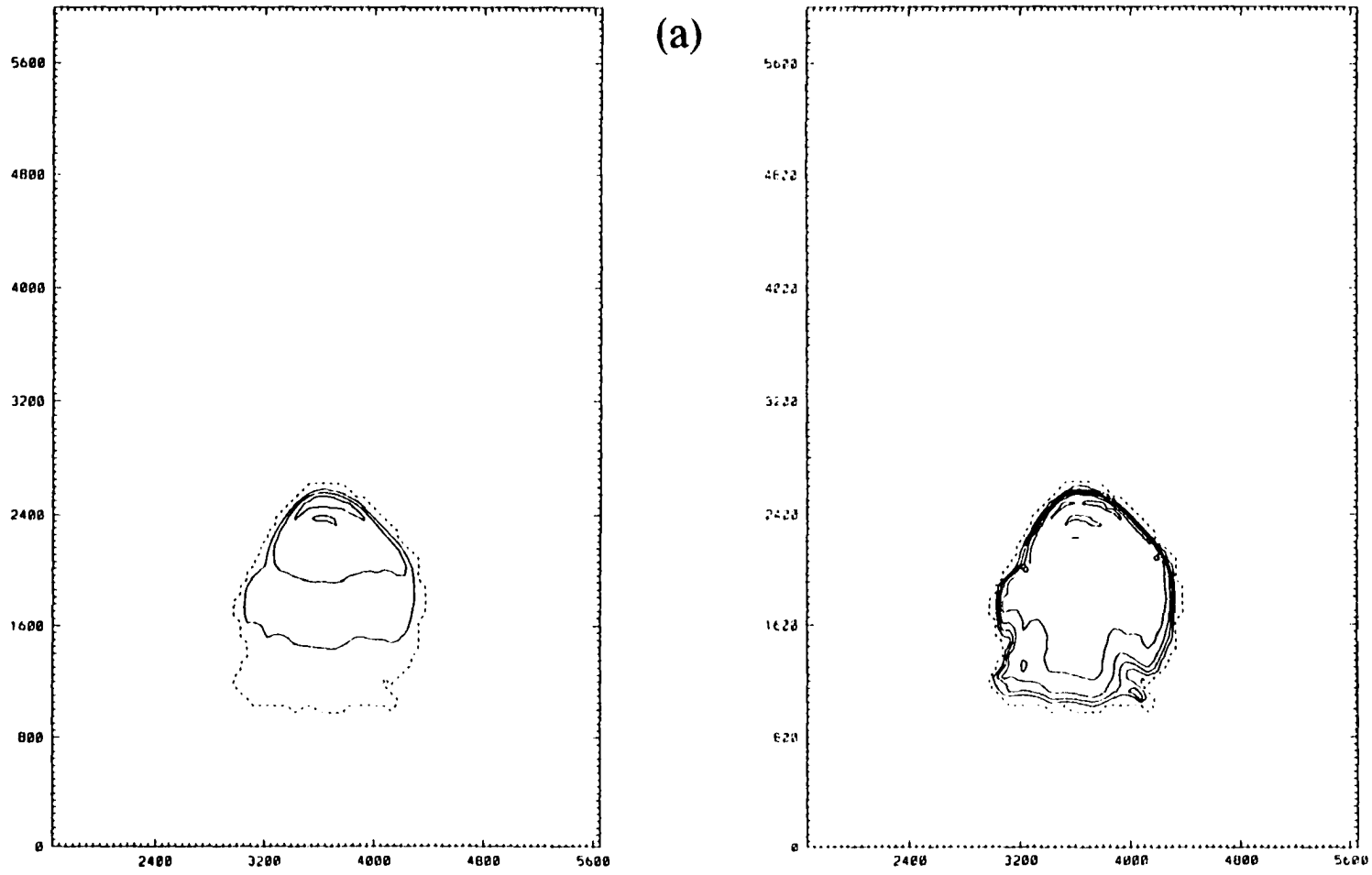


Figure 3.5 Vertical cross-sections of simulated cloud water content (g m^{-3}) (left) and fraction of adiabatic water content (right) at (a) 4 minutes, (b) 7 minutes, (c) 11 minutes and (d) 12 minutes. Dashed contour denotes liquid water content of 0.01 g m^{-3}. Contour interval of solid contours is 1 g m^{-3}. Axes are distance in meters.

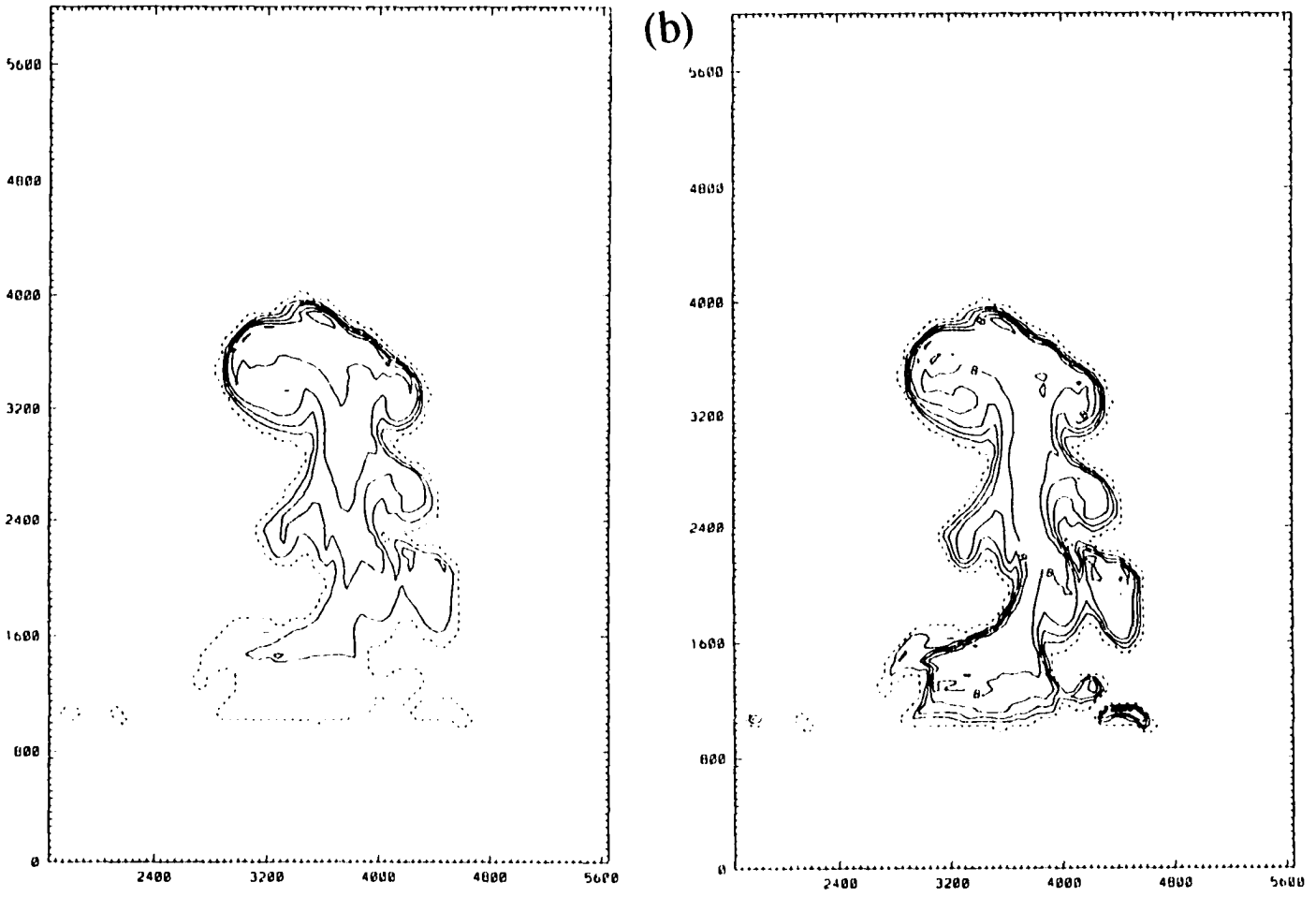


Figure 3.5 (continued)

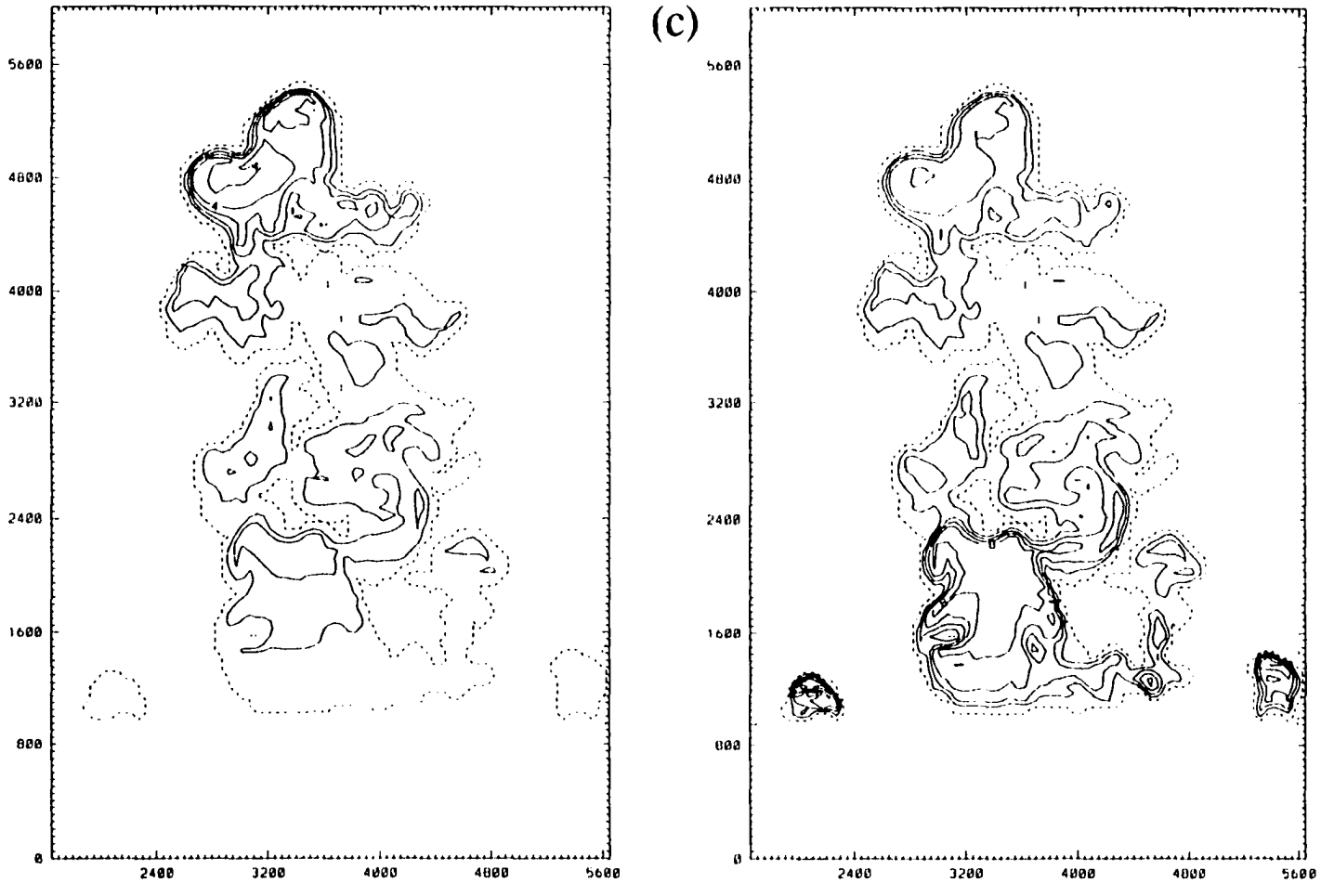


Figure 3.5 (continued)

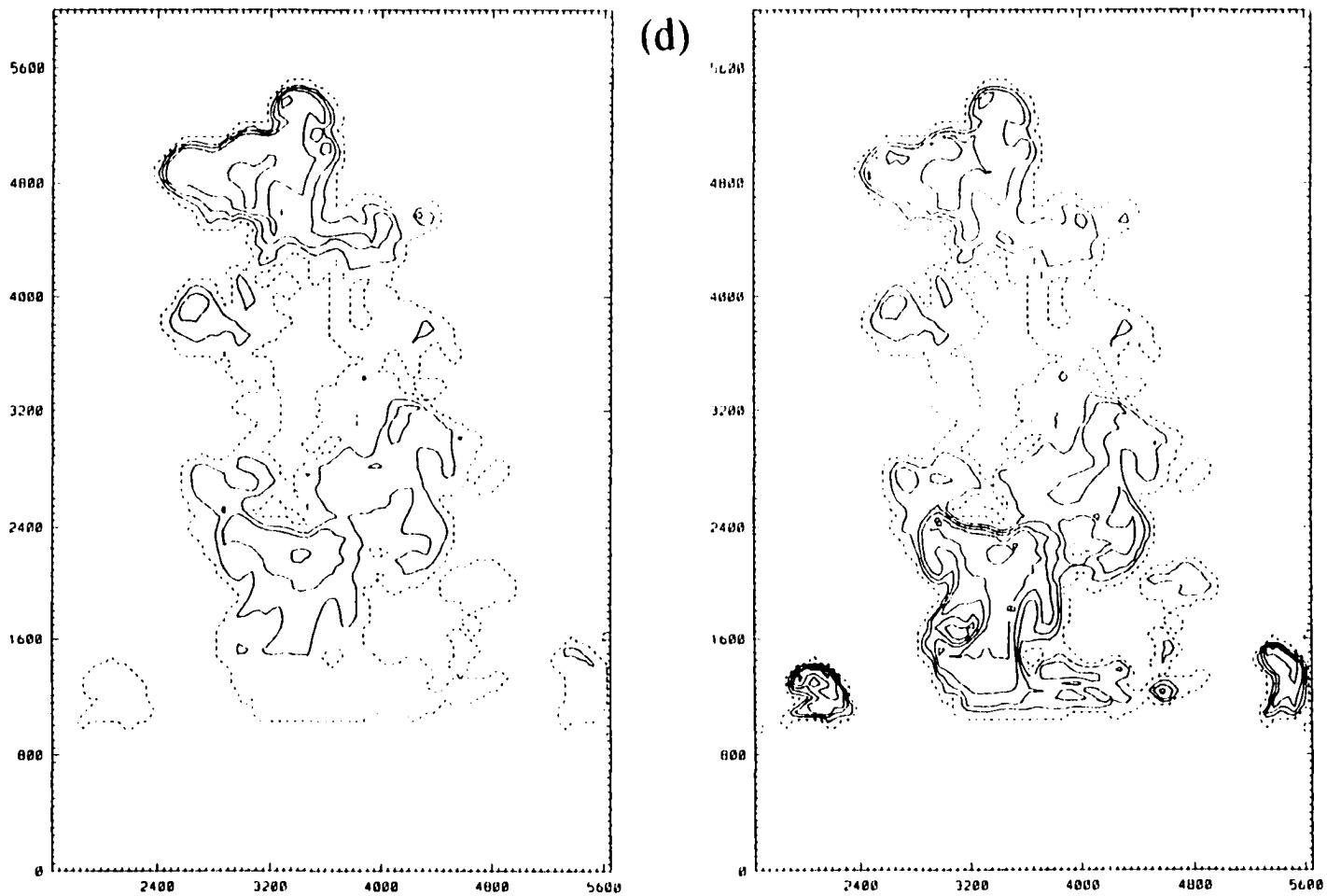


Figure 3.5 (continued)

were from a Johnson-Williams liquid water probe which has been known to underestimate the cloud liquid water content. Comparisons between the simulated and observed cloud water at lower levels, however, agree reasonably well. At the height and corresponding time of the first penetration, the simulated liquid water content falls in the range indicated by the observations (1.5-2.1 g m^{-3}), but at the time of the second penetration is over 1 g m^{-3} higher than the range (1.5-2.1 g m^{-3}) indicated by the observations. While it is possible that the aircraft did not sample the maximum liquid water content present at that level in the cloud, it is also possible that the simulated cloud is underestimating the effects of entrainment at later times. Further experimentation, including changing the magnitude of the fluxes, the coefficients of the turbulence parameterization and the lower levels of the input sounding, did little to decrease the cloud liquid water content without losing the realism of other measured variables within the cloud. Thus, the simulation is used "as is", and the possibility of an exaggerated cloud water content is addressed later in the collection calculations.

4. DESCRIPTION OF COLLECTION-TRAJECTORY MODEL

4.1 Numerical Technique for Solving Trajectory Equation

The technique used to solve the trajectory equations is a predictor-corrector scheme (also used by C94):

$$\begin{aligned} x' &= x_o + dt\ u_o \\ y' &= y_o + dt\ v_o \\ z' &= z_o + dt\ w_o \end{aligned} \tag{7}$$

$$\begin{aligned} x^* &= x_o + dt/2\ (u' + u_o) \\ y^* &= y_o + dt/2\ (v' + v_o) \\ z^* &= z_o + dt/2\ (w' + w_o) \end{aligned} \tag{8}$$

where a "naught" subscript denotes the original position location and velocity, a "prime" denotes the first guess values of position and velocity, and an "asterisk" denotes the new position values. Using the velocity (u_o, v_o, w_o) interpolated to the original location (x_o, y_o, z_o), a "first guess" location (x', y', z') is found , along with the velocity components (u', v', w'). interpolated to that point. (Spatial interpolation is done according to the parabolic scheme of Clark and Farley (1984), while temporal interpolation is linear). These first guess velocity components are averaged with the old velocity components to compute a corrected new position x*, y*, z*. If the new position is different from the first guess position by more than a pre-specified error tolerance (here equal to 10 m in any direction) then the corrected position is used as the first guess for another iteration, which continues until the first guess and final

position is within the error tolerance or until the maximum number of iterations is met (twenty, for the present study). If the first guess and final locations still have not converged at this point, the trajectory is halted. (No convergence problems were encountered for any of the trajectories in this study). The final position is corrected for the falling of the particles at their terminal velocities over the time step using

$$z^*(\text{corrected}) = z^* - dt\ V_t. \tag{9}$$

4.2 Collection Model

4.2.1 Collection Equation

A continuous collection equation of the form

$$\frac{dM}{dt} = \pi(R+r)^2 E_c \Delta V_t q_c \rho_a \tag{10}$$

is used, where M is the mass of the collector drop, R is the radius of the collector drop, r is the radius of the cloud droplets, Ec is the collection efficiency, ΔVt is the difference in the terminal velocities of the collector and collected drops, and q_c is the model-simulated cloud water mixing ratio multiplied by the local air density ρ_a. A "packet" of UGA initialized at cloud base grows according to this equation; all the UGA within the packet grow at the same rate. Because collections among drops originating on UGA are not permitted, the number concentration within a packet is constant.

4.2.2 New Packet Initialization

When the collection model is started, 2304 (48 x 48) packets of UGA are initiated at the height of cloud base, where they are drawn into the cloud by the updraft. To represent most of the UGA that are present in the cloud as time proceeds, it is necessary to continue to initialize new packets at cloud base. A simple scheme accomplishes this task. At the end of every time step, the volume of air entering cloud base at each grid point is accrued according to the formula

$$cbvol = (w - V_t) * area * \Delta t \qquad (11)$$

where w is the updraft speed, Vt is the terminal velocity of the UGA, "area" is the cross-sectional area represented by a grid point and Δt is the time step. Once the accrued volume at a point is greater or equal to a packet volume, a new packet is released at that point and its trajectory is calculated as well.

4.2.3 Spatial and temporal scales

The spatial scale of the packets must be appropriately matched to the time step used in the collection-trajectory model. The packet volume must be large enough so that not more than one packet is initiated at a given point at cloud base per time step. The time step in turn affects the paths of the trajectories and the roundoff error in the coalescence calculations. While very small packet volumes might be desirable for capturing the most detail, the number of packets initiated during a run can grow very large. After some experimentation with different values of packet size and time step length, a packet size of $(50\ m)^3$ and time step of 5 s has been chosen.

4.2.4 Size distribution of UGA

The sizes and concentrations of UGA in the packets (Table 4.1) are roughly half of the maximum values in continental air reported by Noll and Pilat (1971). The midpoint of each bin is used as the radius of the UGA in equation (10).

4.2.5 Collection Efficiencies

Collision efficiencies (Fig. 4.1, Table 4.2) in the model are those summarized by Rogers and Yau (1989)[1], extended to a radius of 2.5 mm using values reported by Beard and Ochs (1984). Coalescence efficiencies are assumed unity for all calculations except when specified otherwise.

4.2.6 Terminal Velocity

The terminal velocities of the cloud droplets and collector drops are calculated according to the size-dependent formulas of Beard (1976) (Fig. 4.2).

4.2.7 Cloud droplet radii

The simulated cloud water is a bulk quantity expressed as a mixing ratio, so it is necessary to assign radii to the cloud droplets which are collected according to (10). The radii influence both the $(R+r)^2$ factor and the collision efficiency, and as the collector drop radius increases their importance decreases. The droplet radii are assigned adiabatic values assuming a droplet concentration of 600 cm^{-3}, the maximum value found in the aircraft penetrations near cloud base. The radius value at a given height is interpolated from among the values in Table 4.3. The cloud drop radius prescription predicts a faster change in radius with height than that implied by the peaks of the aircraft-observed Table droplet spectra. It is possible that the observations do not include adiabatic areas within the cloud, due to limited sampling.

---

[1]A compilation of those values calculated by Klett and Davis (1973), Beard and Ochs (1984) and Mason (1971).

Table 4.1 UGA radii and number concentrations used in the collection-trajectory model. Number concentrations are expressed for bin widths of 10 μm.

radius (μm)	Concentration (m^{-3} 10 μm^{-1})
15	1450
25	260
35	125
45	50
55	10
65	5
75	0.6
85	0.3
95	0.05

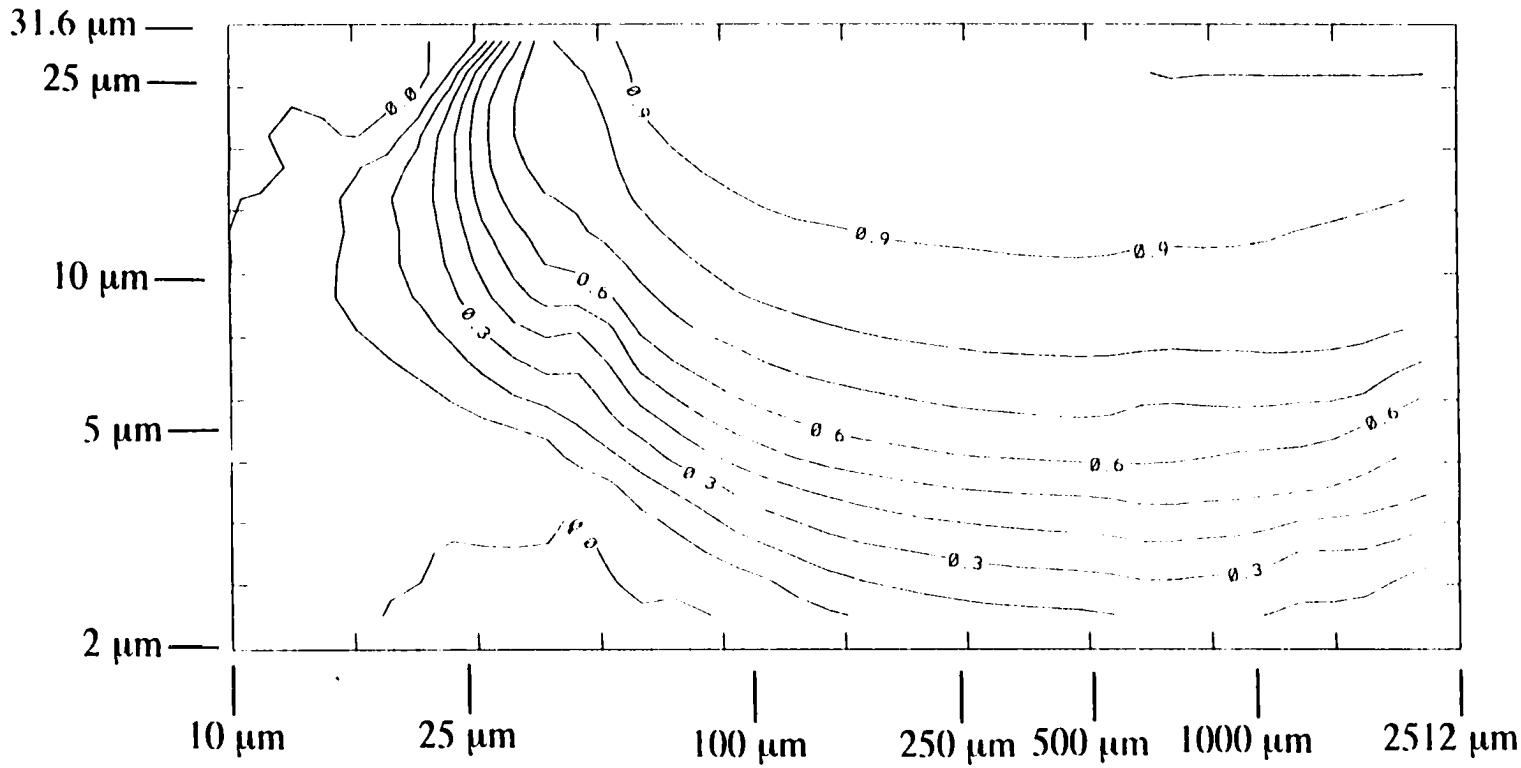


Figure 4.1 Collision efficiency, as a function of drop radii, used in the collection-trajectory model. Contour interval is 0.1.

Table 4.2 Numerical values (in percent) of collision efficiencies plotted in Fig. 4.1. Top row denotes collector drop radius in μm; farthest column to the left denotes smaller drop radius, in μm .

	10.	12.6	16.	20.	25.	32.	40.	50.	63.	79.	100.	126.	158.	200.	251.	316.	398.	501.	631.	794.	1000.	1259.	1585.	1995.	2512.
31.6	0	0	0	0	0	0	70.0	90.7	93.1	96.7	97.0	97.1	97.4	97.5	97.5	97.5	97.6	97.7	100.	100.	100.	100.	100.	100.	100.
25.1	0	0	0	0	0	52.1	75.0	79.5	91.9	95.2	95.9	96.1	96.3	96.4	96.5	96.5	96.6	96.8	100.	100.	100.	100.	100.	100.	100.
20.0	0	0	0	0	25.0	59.0	75.0	75.4	88.7	92.4	94.1	94.7	95.1	95.4	95.5	95.6	95.6	95.7	96.3	97.1	98.0	97.6	97.1	96.4	95.6
15.8	0	0	07.5	17.0	29.3	57.5	70.9	73.7	83.2	88.6	91.2	92.5	93.0	93.6	93.7	94.0	94.0	94.1	94.1	94.1	93.8	93.2	92.5	91.6	90.2
12.6	0	06.5	08.0	17.0	27.9	49.3	63.1	70.0	77.3	83.3	87.2	89.1	89.8	90.7	91.0	91.2	91.6	91.7	90.8	90.8	90.6	89.9	89.1	88.0	86.0
10.0	0	07.0	09.5	17.0	25.1	40.4	55.0	58.3	69.6	76.3	81.4	84.2	85.9	86.8	87.3	87.9	88.0	88.0	88.0	88.0	88.0	88.0	87.1	85.0	82.6
7.94	05.2	07.0	08.0	11.8	18.0	29.7	39.4	39.7	59.6	67.9	72.5	76.1	78.6	80.6	81.7	82.6	82.7	82.9	82.9	82.5	82.0	82.6	81.6	78.4	74.3
6.31	05.2	06.0	05.5	06.8	10.0	16.8	25.3	28.6	45.2	55.4	62.7	66.9	69.4	71.3	72.9	74.0	74.7	74.9	72.2	73.1	74.3	73.0	72.0	63.5	59.0
5.01	04.4	04.8	03.5	04.2	04.8	06.1	07.8	19.5	28.8	40.7	48.9	54.8	59.0	61.3	63.2	64.2	65.0	65.5	64.5	63.3	61.7	61.0	57.0	51.9	47.1
3.98	03.7	03.0	03.0	02.7	02.3	02.0	02.0	03.0	14.8	23.0	32.1	38.5	42.7	46.1	48.8	50.2	51.0	51.7	53.8	53.0	52.0	50.1	47.2	43.1	37.9
3.16	02.5	02.4	01.0	01.8	0	0	0	0	02.8	10.3	17.9	23.7	28.9	31.7	33.7	35.4	36.7	37.5	39.8	38.6	37.0	32.0	32.0	27.8	21.5
2.51	02.0	02.0	01.5	0	0	0	0	0	0	0	03.6	09.8	15.1	18.3	21.0	22.9	23.5	24.5	26.9	25.9	24.7	21.0	21.0	15.8	12.3
2.00	01.7	01.5	01.1	0	0	0	0	0	0	0	0	0	01.3	03.9	06.0	08.0	09.8	10.2	16.7	15.9	15.0	12.4	09.6	06.7	03.6

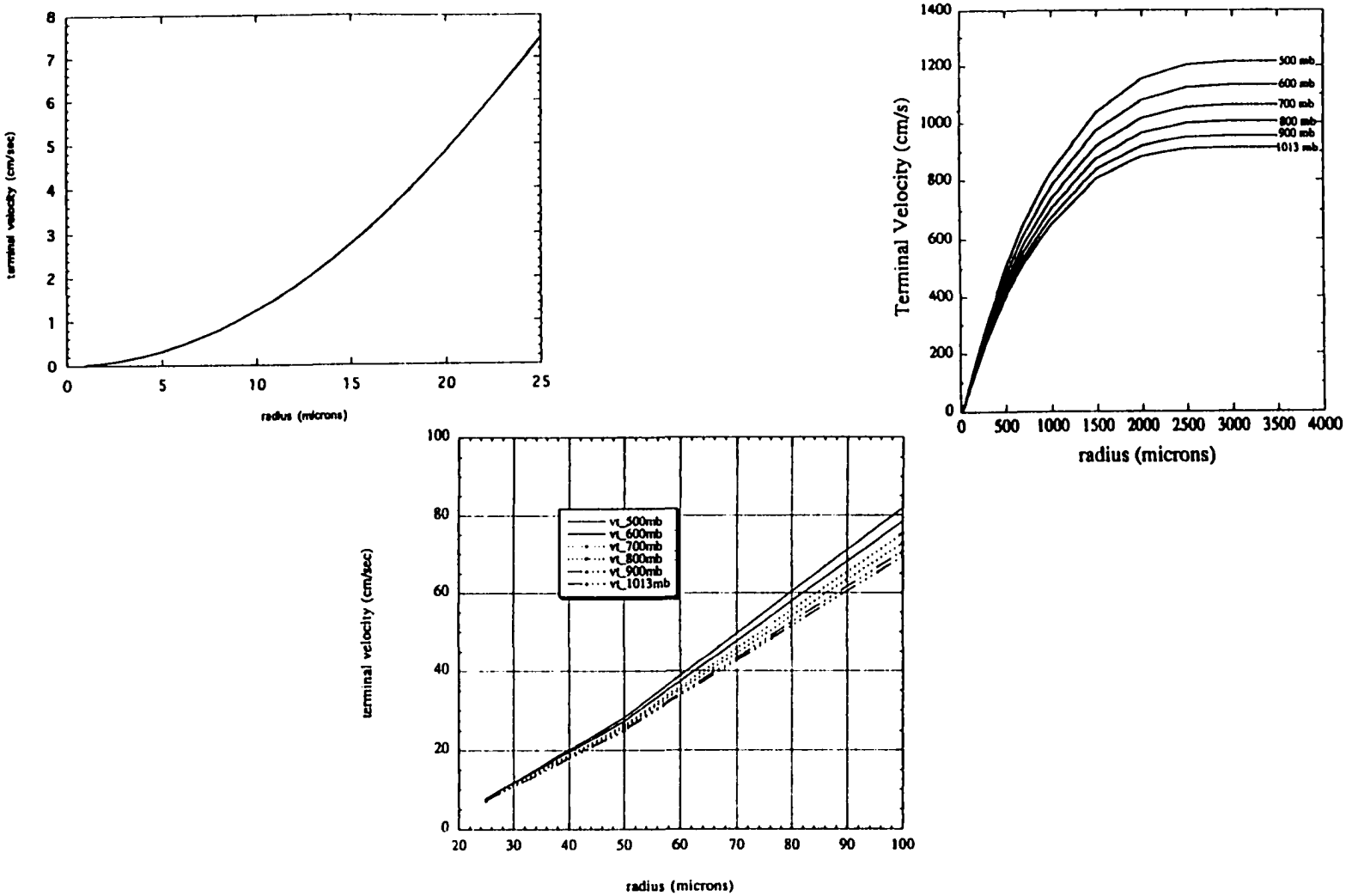


Figure 4.2 Terminal velocity as a function of drop radius and atmospheric pressure, using formulas of Beard (1976).

Table 4.3 Cloud droplet radii assigned in the collection-trajectory model, as a function of altitude. Also listed is radius at peak concentration from observed FSSP spectra.

height (km)	radius (μm)	observed radius (μm)
1.0	3.0	
1.5	9.48	
1.8		8-9
1.9	11.07	
2.39		8-9
2.5	12.87	
3.2	14.49	
4.0	15.66	
5.0+	16.77	

Sensitivities of the coalescence calculations to this prescribed drop distribution with height is tested later.

4.2.8 Reflectivity Calculations

At one minute intervals, the reflectivity attributable to the packets is calculated over the $(200m)^3$ volume within which they occur at that time, using (5). The volumes over which the reflectivity is calculated are larger than the packet volumes, to help account for the spreading and contorting of the packets as they move through the cloud.

The cloud droplets also contribute to the reflectivity factor. Because cloud water is expressed in the model in bulk form without any specification of droplet size, a simple scheme is used to calculate radar reflectivity as a function of cloud liquid water content. The concentration of cloud droplets (600 cm^{-3}) is adjusted by multiplying by the fraction of adiabatic cloud water at that location. The concentration of particles is decreased near the cloud edges and other areas of low liquid water content. The reflectivity is calculated using the adjusted drop concentration and the prescribed cloud droplet radius at that height. This reflectivity is then added to that calculated from the packets containing the drops formed on UGA.

The decrease in cloud droplet concentration without a decrease in the radii is the result of inhomogeneous mixing, a representation of the mixing process in which the time necessary to evaporate cloud droplets is less than that required for a volume to become homogeneous by turbulent mixing of the entrained air. At the cloud edges, some drops are completely evaporated, producing a saturated volume of air that is then mixed into the rest of the cloud. This representation is supported to some extent by the observations from the FSSP[2] for the 22 July cloud. At the scales at which the data

[2] The forward-scattering spectrometer probe, or FSSP, measures the light intensity scattered by a particle passing through a laser bean, and converts it to a particle size. The sizes of water droplets measured by this probe are 3-52 μm diameter.

are collected (here, about 100 m), the mixing does appear to be inhomogeneous; the peak in the droplet distribution maintains itself to the cloud edges as the entire spectrum decreases in number (Fig. 4.3). These observations are consistent with spectra observed elsewhere (Paluch and Knight 1984, 1986). They do not capture the details of the mixing process at smaller scales, however, so a test considering the effects of homogeneous mixing is conducted later.

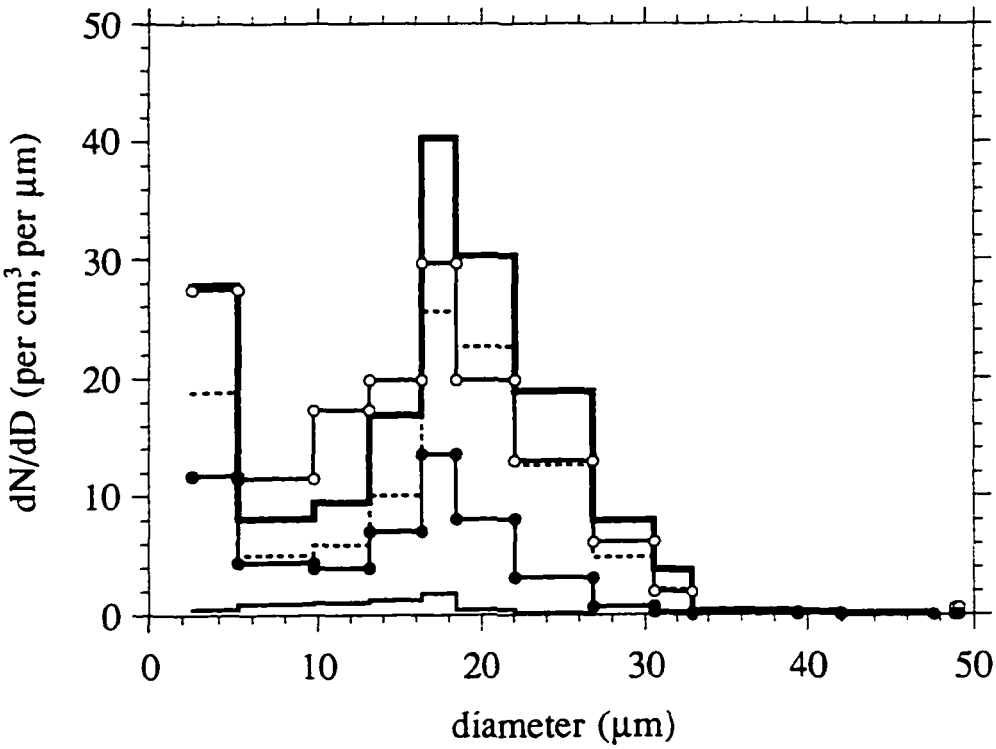


Figure 4.3 One-second drop spectra from the FSSP, sampled during a single penetration of the cloud at 2385 m altitude.

5. RESULTS

5.1 Reflectivity evolution

5.1.1 Cloud water

From the 3-D simulated cloud liquid water content presented in Section 3.3, the reflectivity due to the cloud water alone can be calculated, using the adiabatic drop radii and the concentrations adjusted for sub-adiabatic liquid water content. This reflectivity represents that from condensation processes alone, since collections among cloud droplets cannot occur. The reflectivity patterns (Fig. 5.1) appear much like those on X-band radar, increasing in value towards the upper center of the cloud, having a sharp gradient near cloud top during the times of strong ascent and decreasing in value toward all other cloud edges. At no time does the reflectivity due to the cloud droplets alone reach 0 dBZ in any part of the cloud (Fig 5.2), as predicted by the calculations using adiabatic drop sizes presented in Section 2.3. The reflectivity is initially less than -25 dBZ and peaks at -4 dBZ after 9 min. It will be shown that the reflectivity from the cloud droplets dominates that from the drops formed on UGA during the first 6 min, because of their much larger number, despite the fact that particles as large as 95 μm radius are being ingested into the cloud.

5.1.2 Primary run

When the collection-trajectory model is initialized with UGA and run, the evolution of the reflectivity field (Fig. 5.3) is initially the same as that from cloud water alone, but then becomes quite different. For the first 6 min, the reflectivity attributable to the drops formed on UGA is negligible throughout the entire cloud (compare with Fig. 5.1). After 7 min, however, the UGA drops start to dominate the

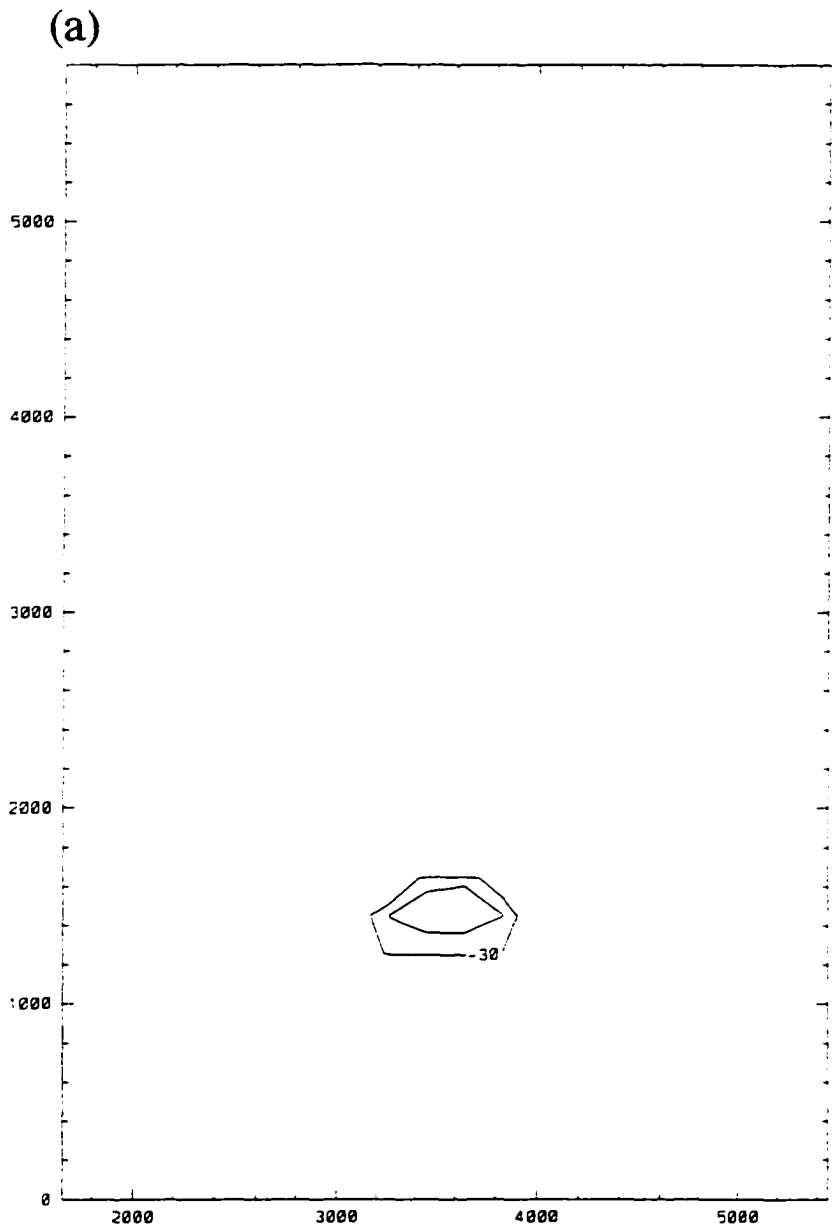


Figure 5.1 Vertical cross-sections of reflectivity factor calculated from simulated cloud water, after: (a) two minutes, (b) four minutes, (c) six minutes, (d) eight minutes, (e) ten minutes and (f) twelve minutes.

(b)

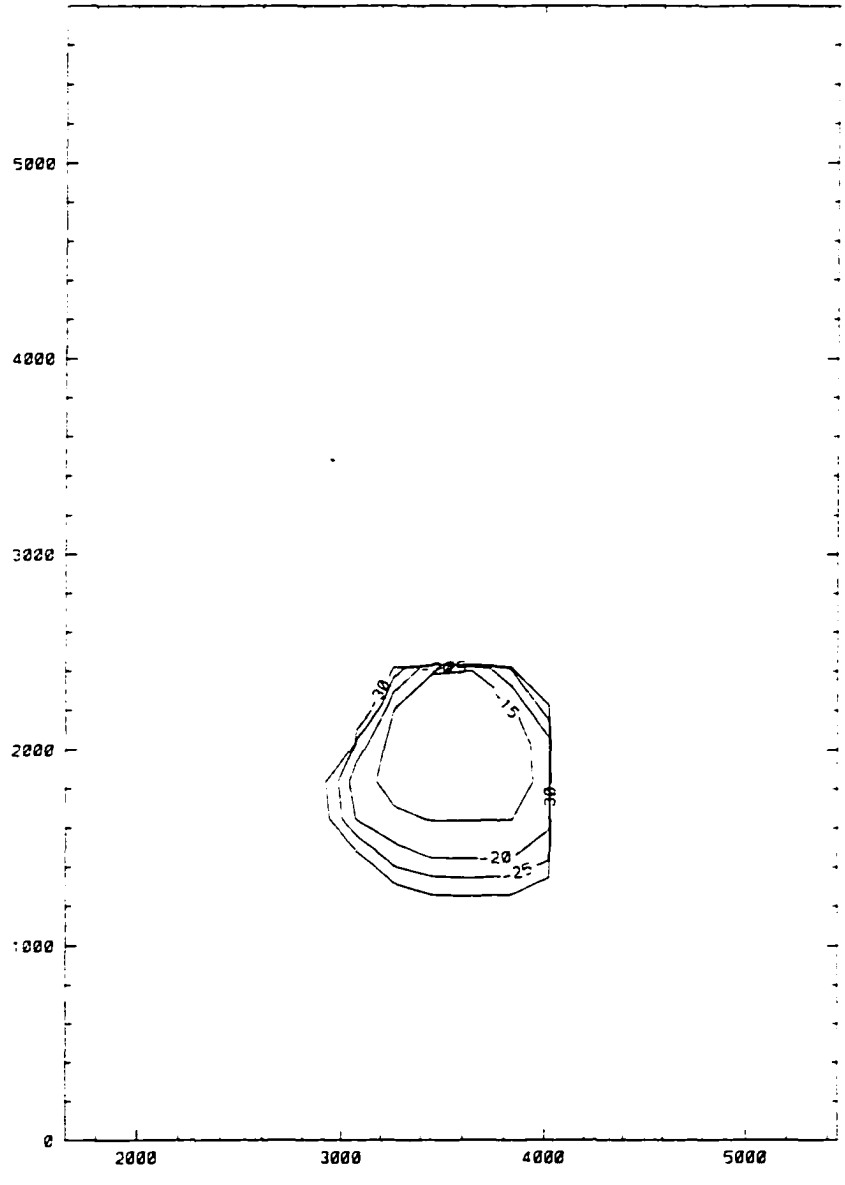


Figure 5.1 (continued)

(c)

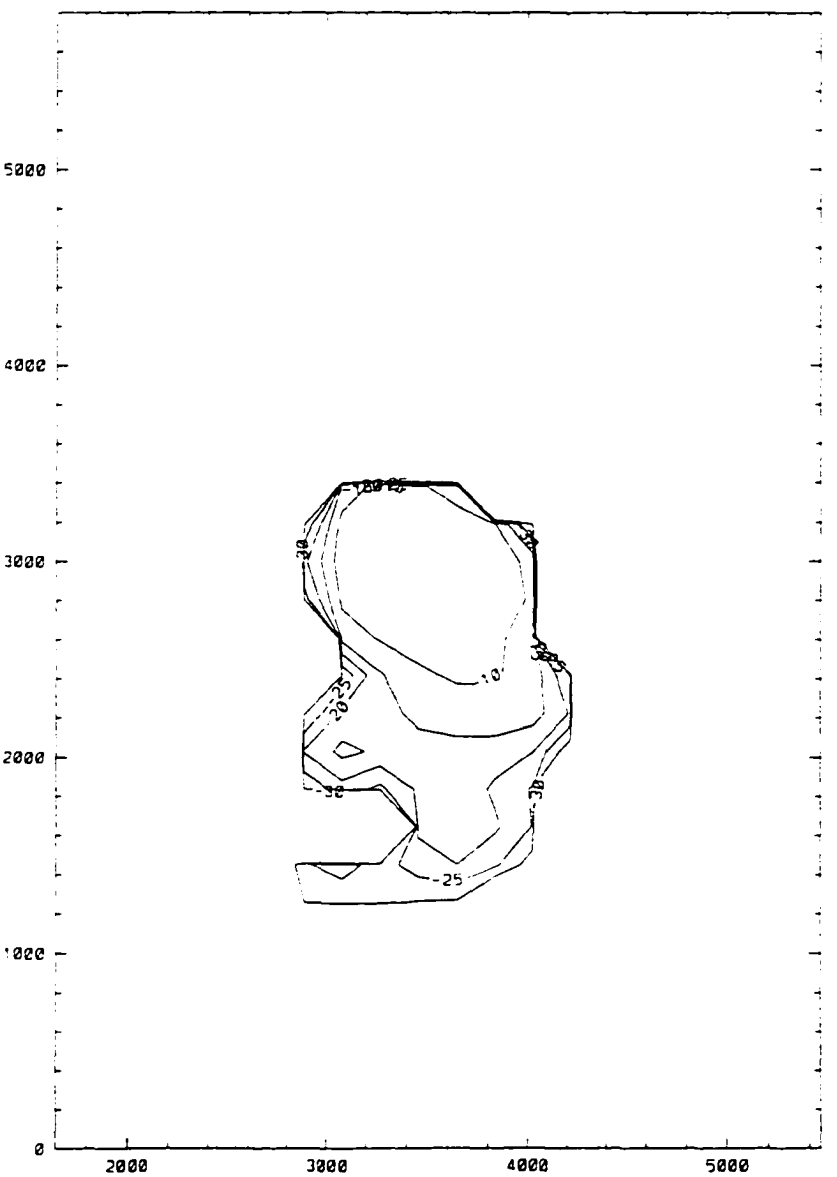


Figure 5.1 (continued)

(d)

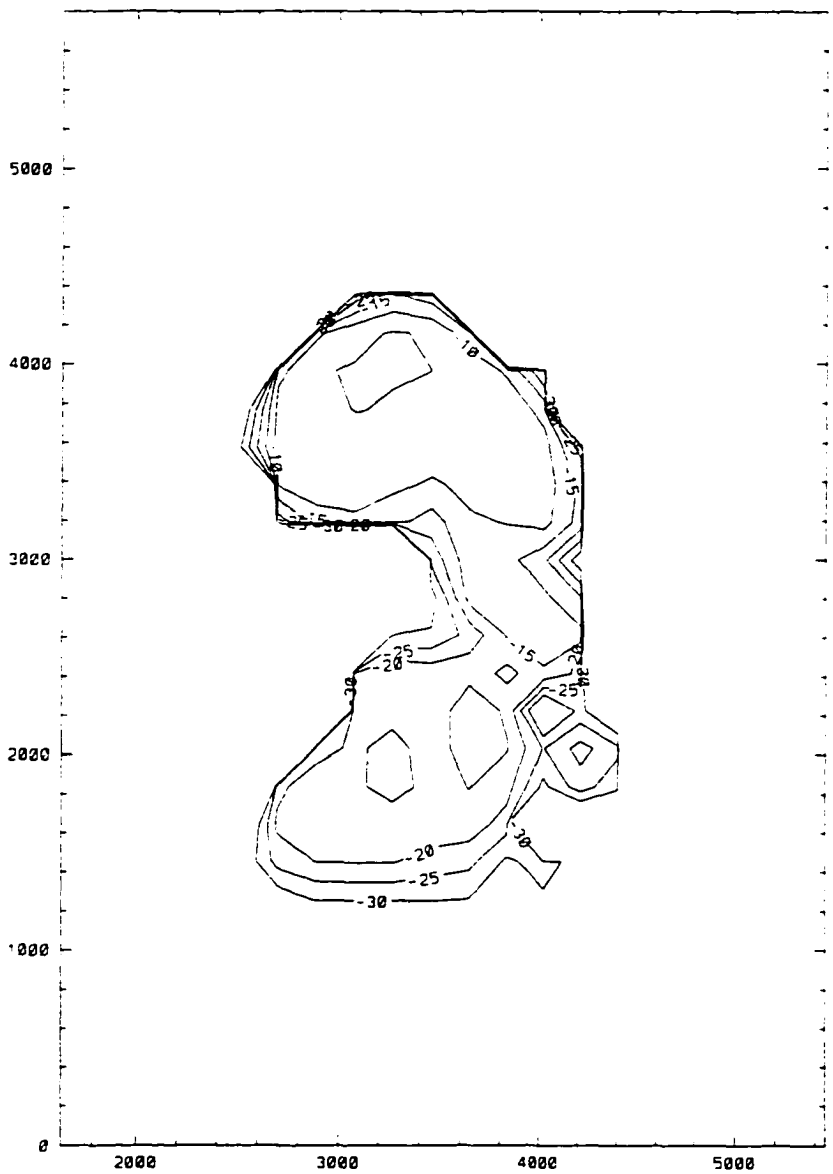


Figure 5.1 (continued)

(e)

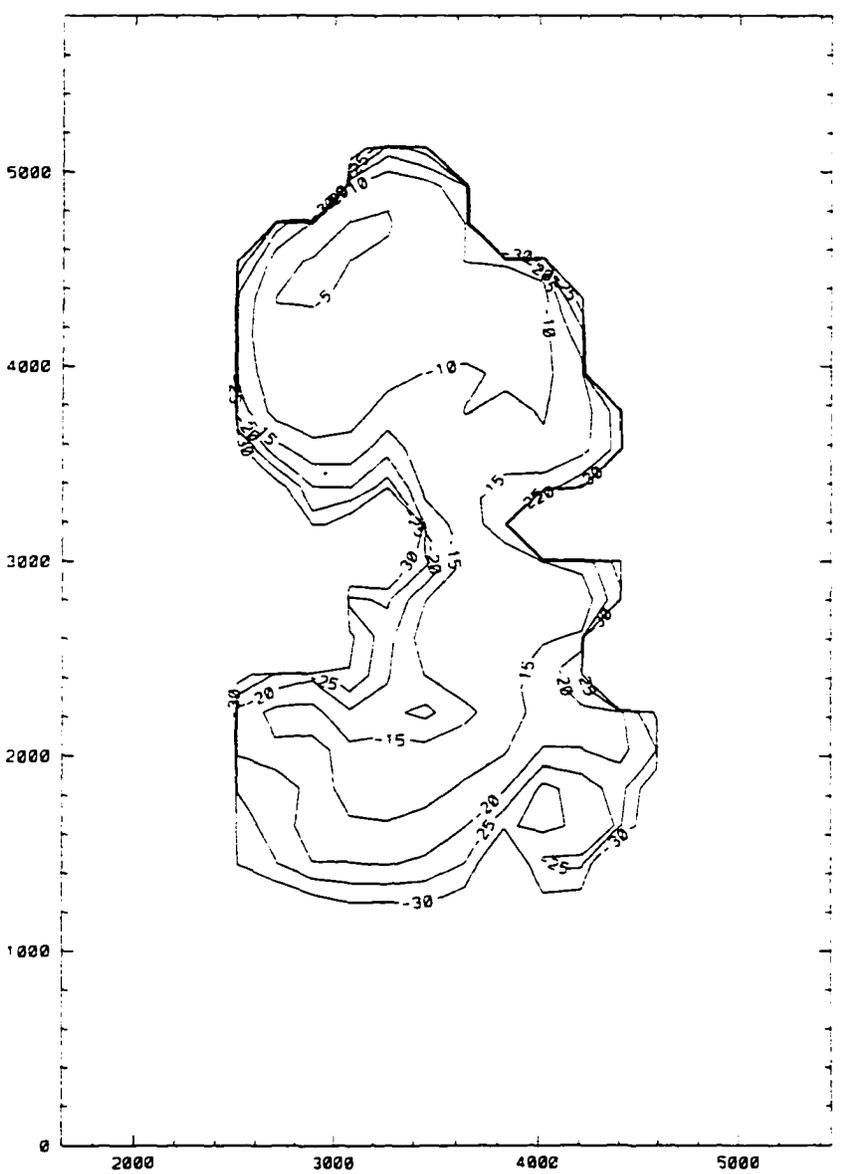


Figure 5.1 (continued)

(f)

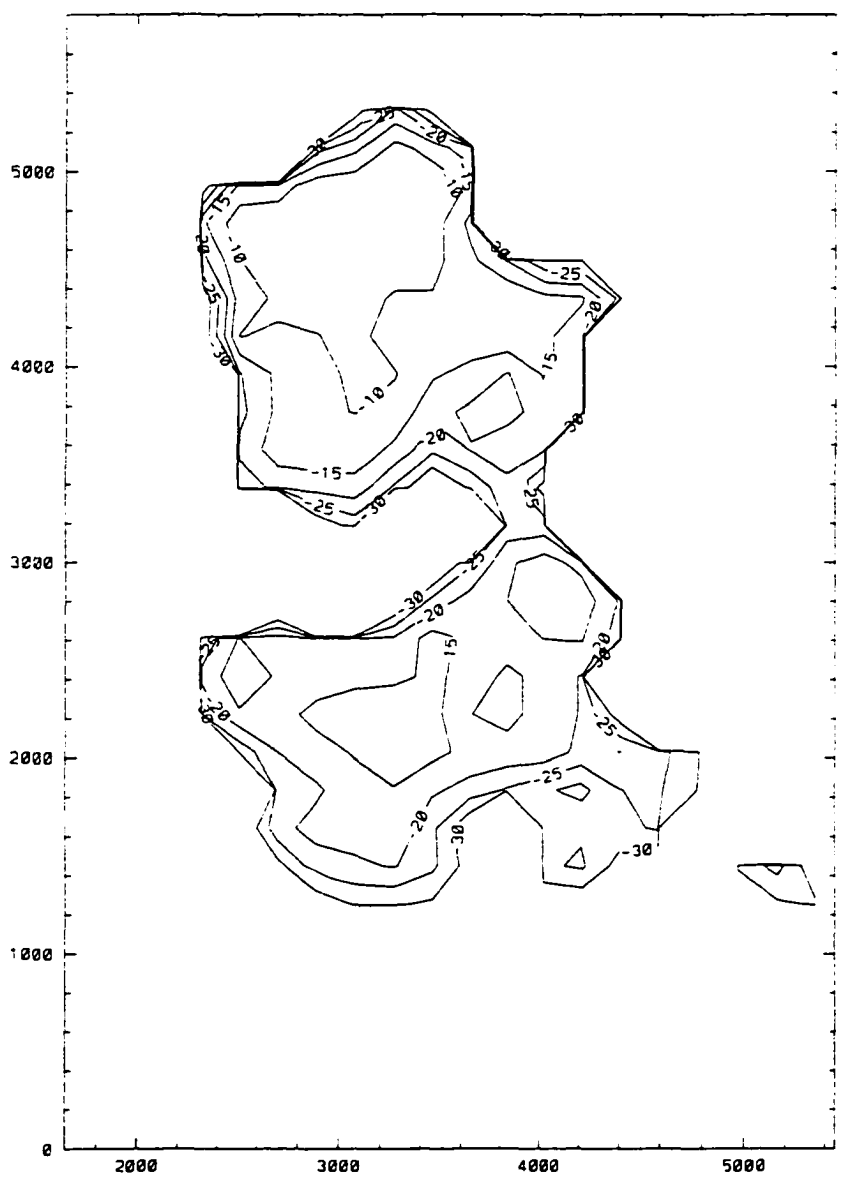


Figure 5.1 (continued)

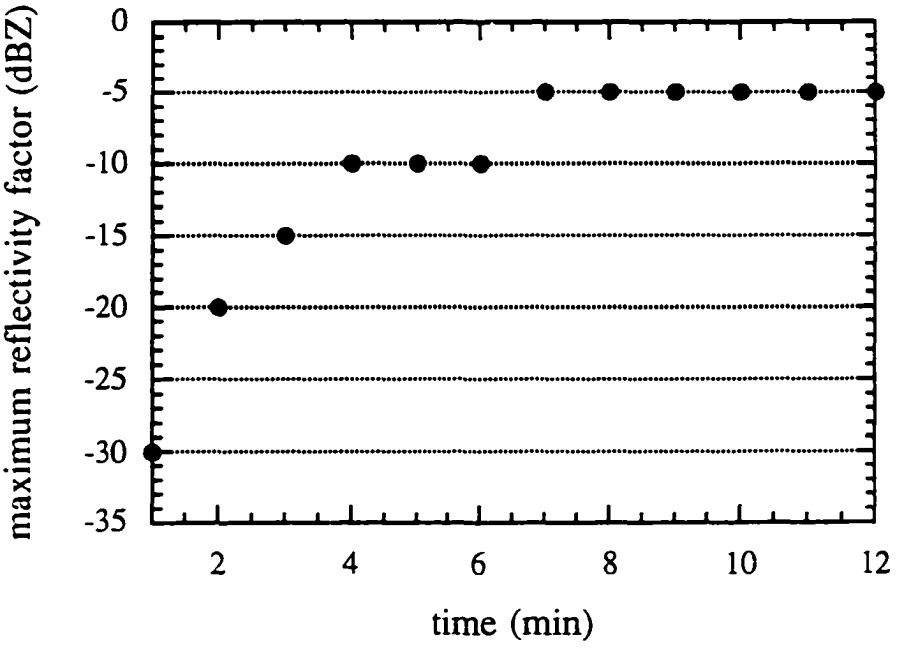


Figure 5.2 Maximum echo calculated from modeled cloud drops.

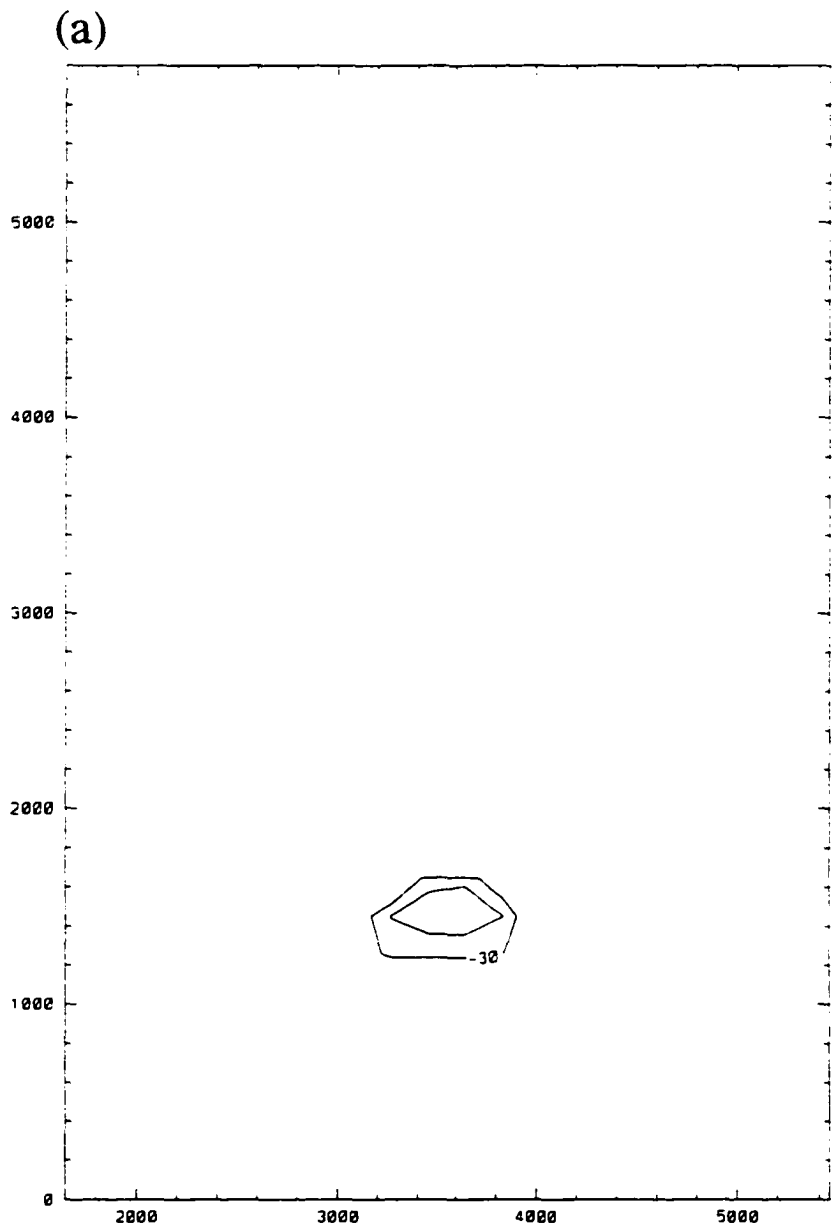


Figure 5.3 Vertical cross-sections of reflectivity factor calculated from cloud water and drops grown on UGA for the primary run, after: (a) two minutes, (b) four minutes, (c) six minutes, (d) eight minutes, (e) ten minutes and (f) twelve minutes.

(b)

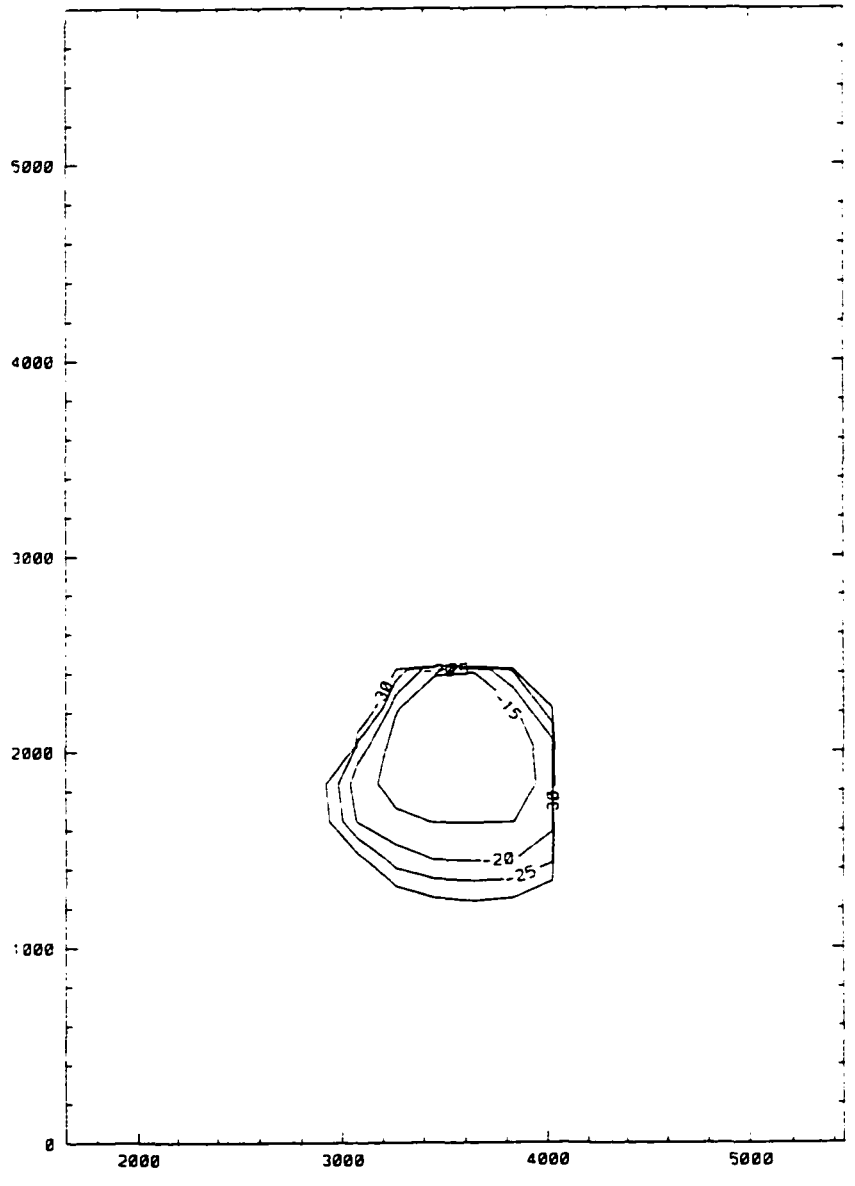


Figure 5.3 (continued)

(c)

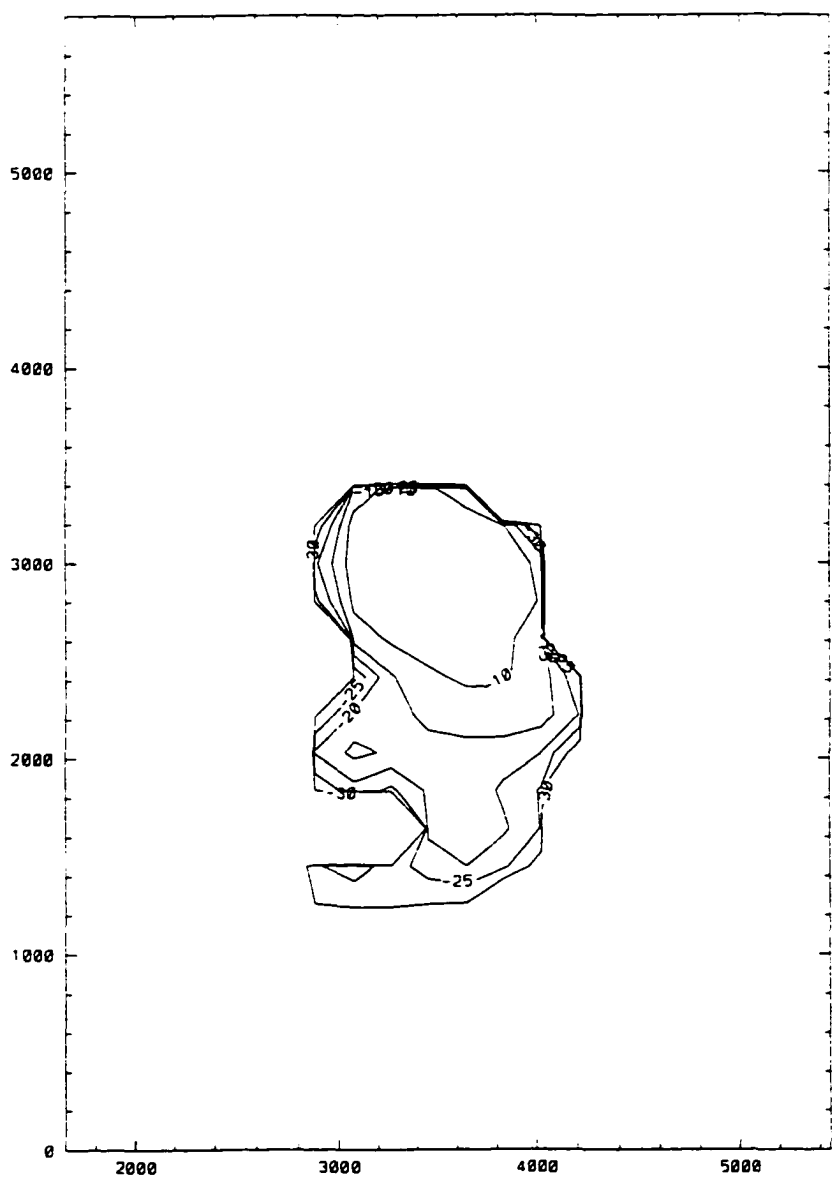


Figure 5.3 (continued)

(d)

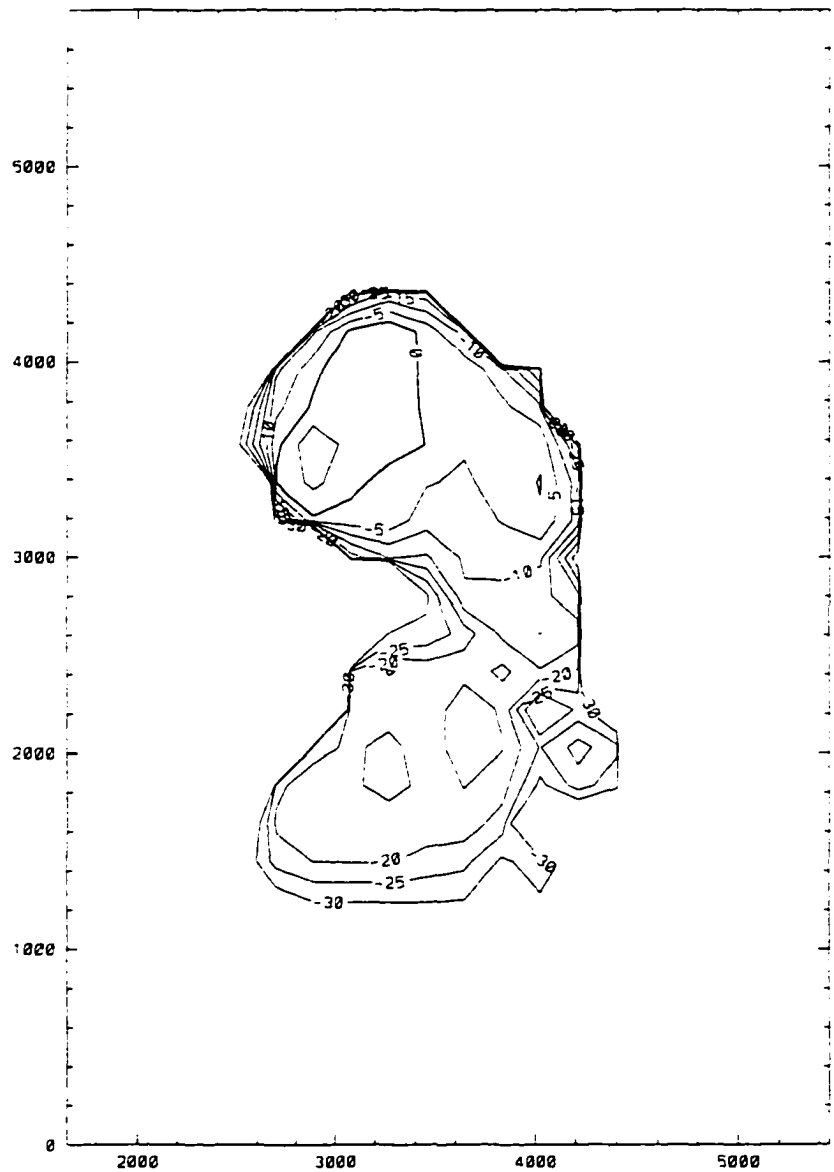


Figure 5.3 (continued)

(e)

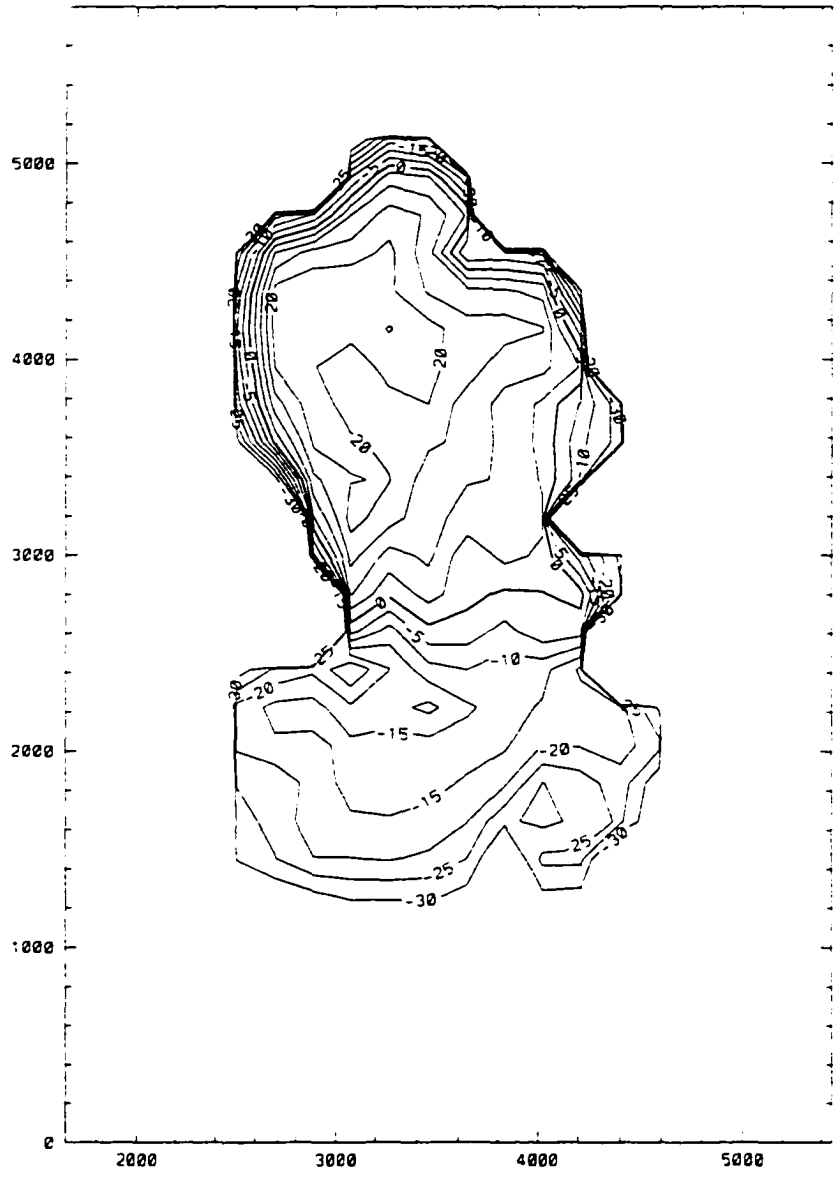


Figure 5.3 (continued)

(f)

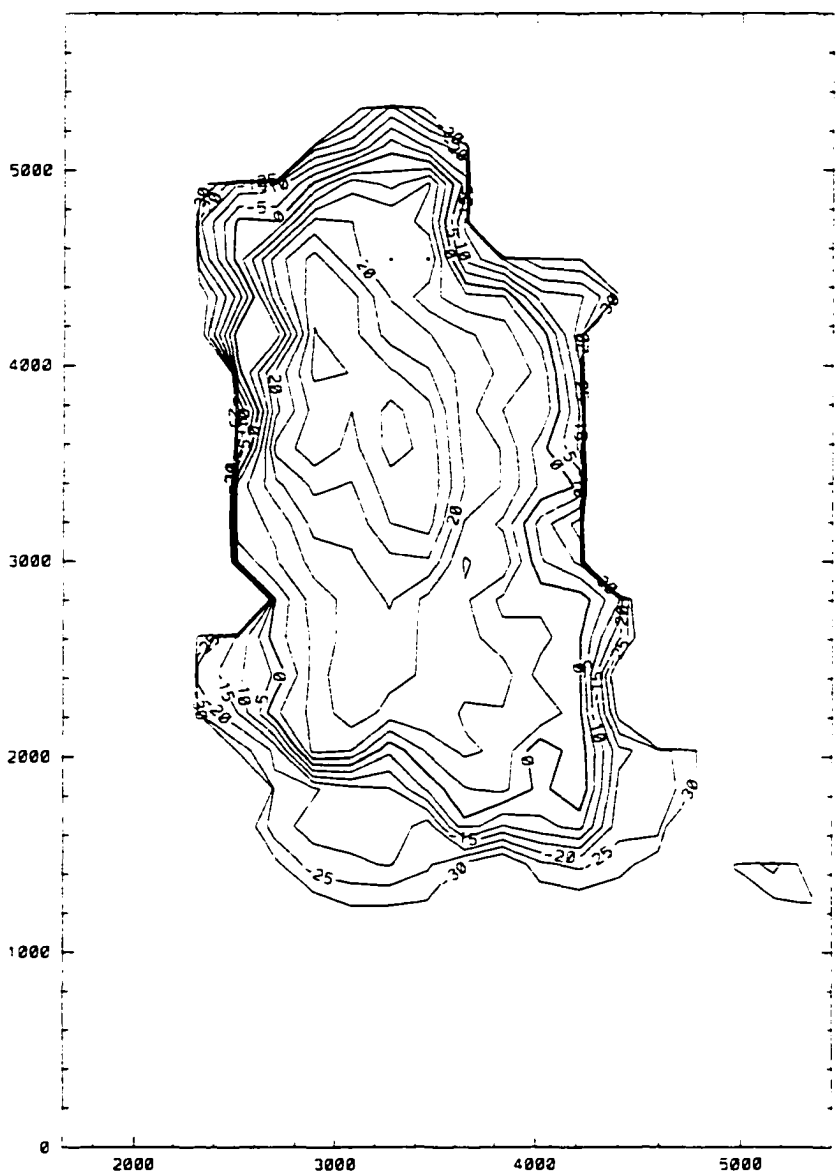


Figure 5.3 (continued)

echo pattern. The growth of the UGA by collection produces a 0 dBZ echo (Fig. 5.4a) at approximately 3.8 km height (Fig. 5.4b) between 7 and 8 min. By 9 min, the maximum reflectivity has jumped to over 20 dBZ, and quickly grows to 40 dBZ by 12 min. The maximum echo never ascends above 4.5 km throughout the run.

5.1.3 Noise tests

Before testing the sensitivity of the reflectivity to various formulations of physical quantities, an estimate of the noise in the reflectivity due to the technical aspects of the model is made.

5.1.3a Time step and packet initiation

A 5 s time step is used for the primary run, but tests presented earlier in Section 2.2 suggest that truncation error can lead to an underestimation of growth by collection. In addition, if the packets take different paths because a shorter time step is used to solve the trajectory equation, the underestimation of growth could be either offset or amplified. A test in which the time step is decreased to 2.5 s shows little effect. The maximum reflectivity and the height at which it occurs (labeled "dt" in Fig. 5.5) is very similar to the primary run, except that the magnitudes of the maximum reflectivity are increased between 1 and 3 dB. The 0 dBZ echo again forms at 7 min, and the quick increase in the maximum reflectivity evident in the primary run is only amplified in this test.

The time at which the packets are first introduced into the cloud is the time at which 0.001 g m^{-3} of cloud water first appears in the cloud water field. A test in which the packets are initiated two minutes earlier shows little change. The development of the reflectivity (labeled "ext" in Fig. 5.5) is nearly identical to the primary run, because

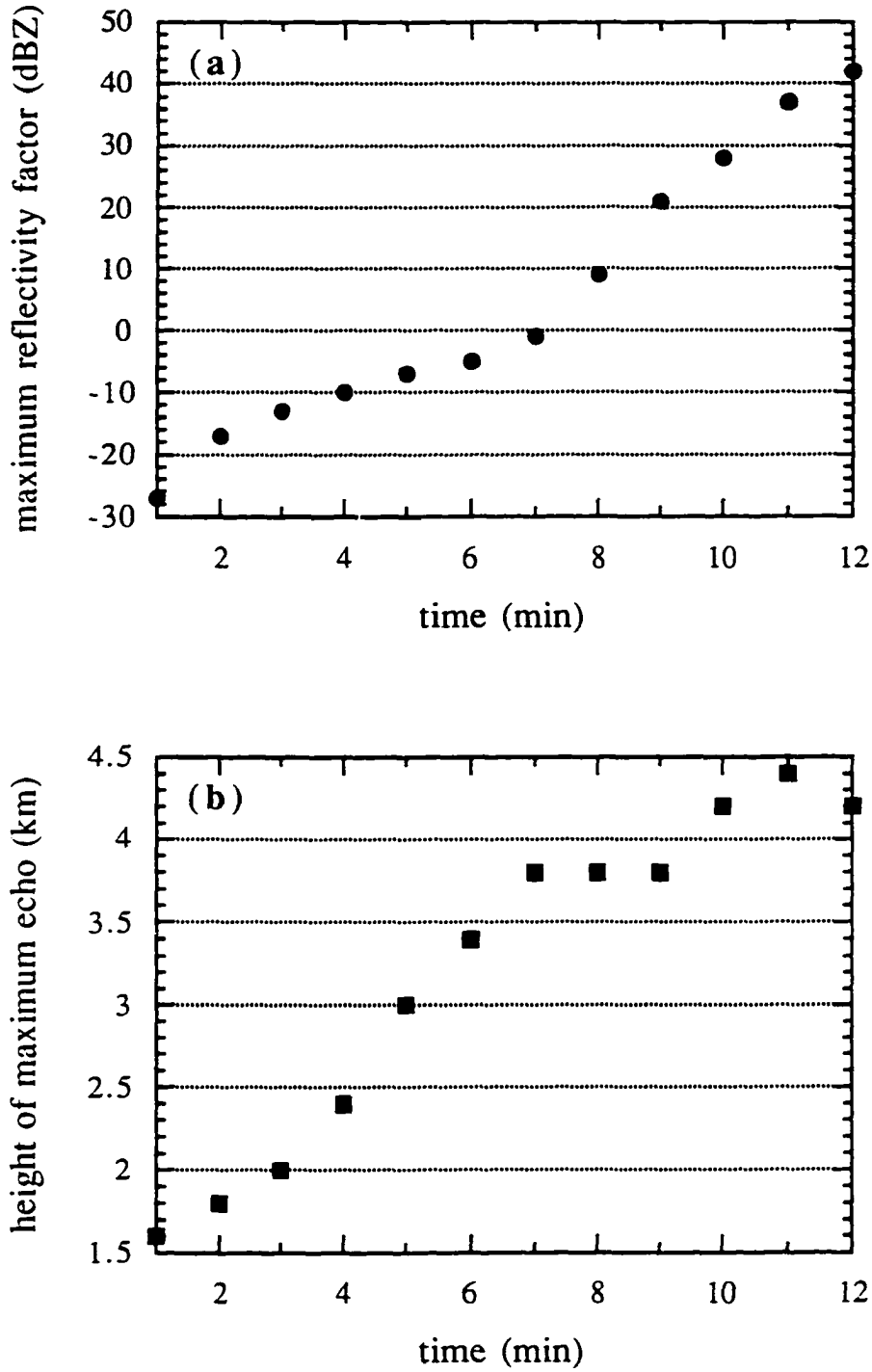


Figure 5.4 (a) Maximum echo calculated from cloud droplets and drops grown on UGA (primary run), as a function of time. (b) Height of maximum echo plotted in (a).

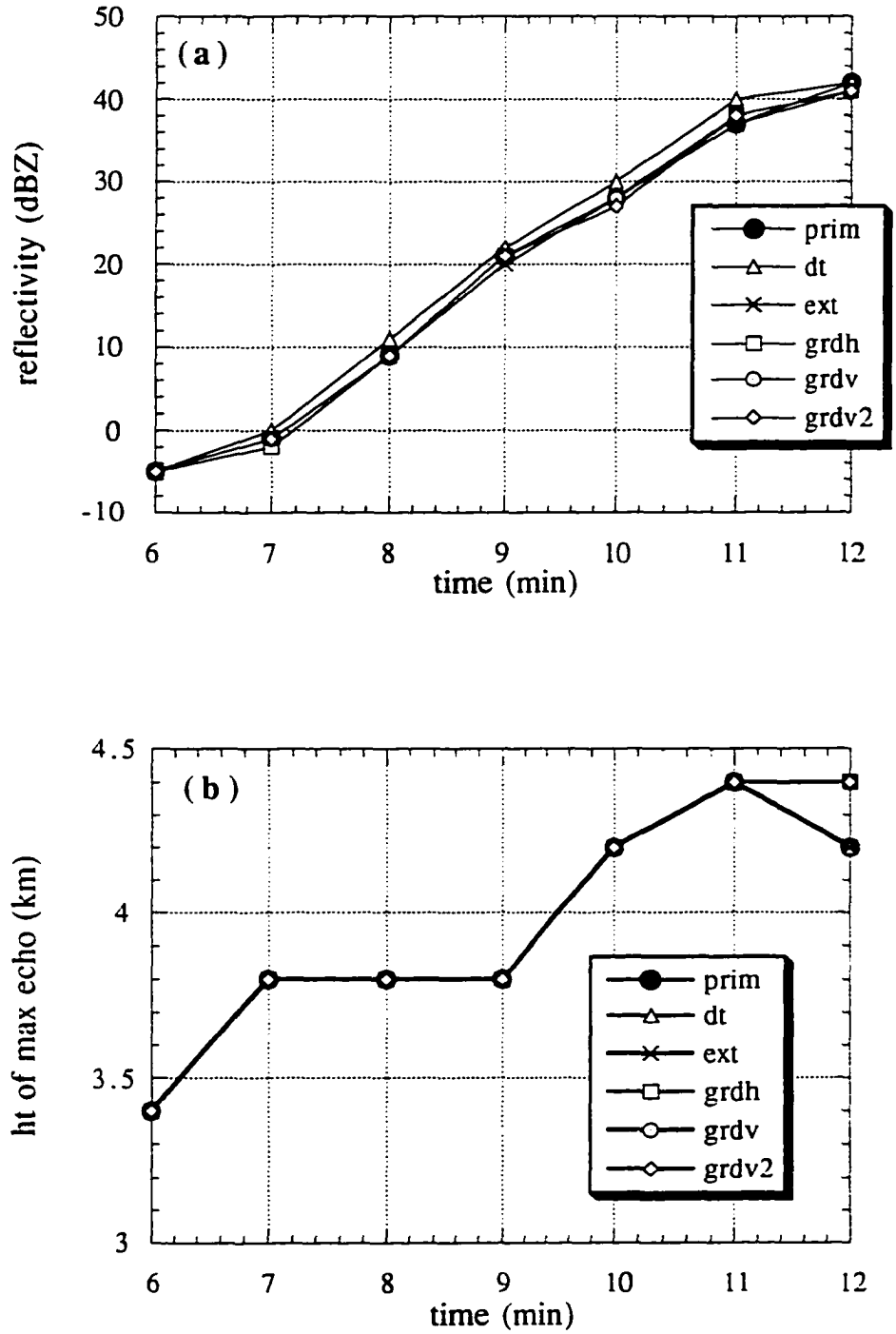


Figure 5.5 (a) Maximum echo calculated from cloud water and drops grown on UGA for all noise tests. (b) Height of maximum echo plotted in (a).

at these early times the cloud inflow is weak and little cloud water exists to be collected.

5.1.3b Simulated fields frequency

A simplification of the design of this study is that the full 3-D cloud model needs to be run only once to get the cloud fields, and then the coalescence-trajectory model can be run many times to explore sensitivities. A result of this framework is that the cloud model fields must be ingested into the collection-trajectory model at regular intervals, but the frequency is limited by the disk space occupied by the cloud model output files, and the additional I/O time when running the collection model. The primary run ingests the simulated fields every 30 s. Results of a comparison test among ingest intervals of 15, 30 and 60 s (Fig. 5.6) do show a dependence on the ingest interval. There is less than 1 dB difference in the 15 and 30 s ingest frequencies throughout the time period, but the 60 s ingest lags the 30 s by as much as 3 dB. The decrease in the reflectivity with the less frequent ingest intervals is due to the underestimation of updraft speed (Fig. 5.7a) and cloud liquid water (Fig. 5.7b) as they increase. Although evidence has been sought for packets having different trajectories through the cloud as the cloud fields are better resolved, no convincing tendencies have been found for those packets contributing the most to the reflectivity. This topic may be better explored in a cloud model where spatial as well as temporal resolution is varied.

5.1.3c Packet size and initiation sites

Each packet volume is $(50m)^3$, which undoubtedly misses a lot of the variation among the actual particle trajectories within the volume. As an illustration, a packet of 45 μm UGA that produced drops 1673 μm radius is divided into 125 "sub-packets",

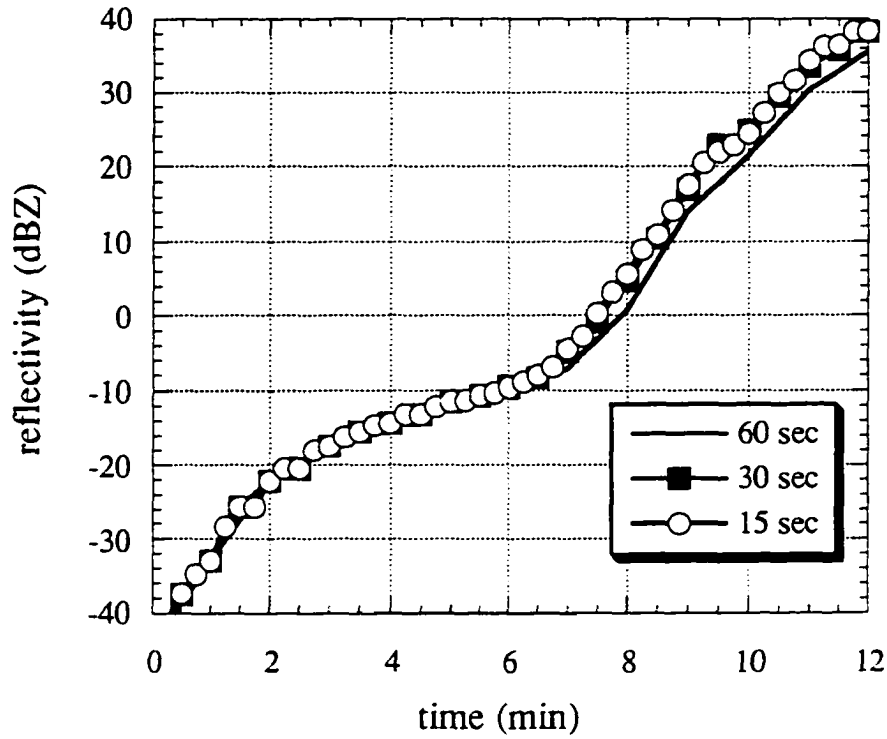


Figure 5.6 Maximum echo as a function of ingest interval of simulated cloud fields.

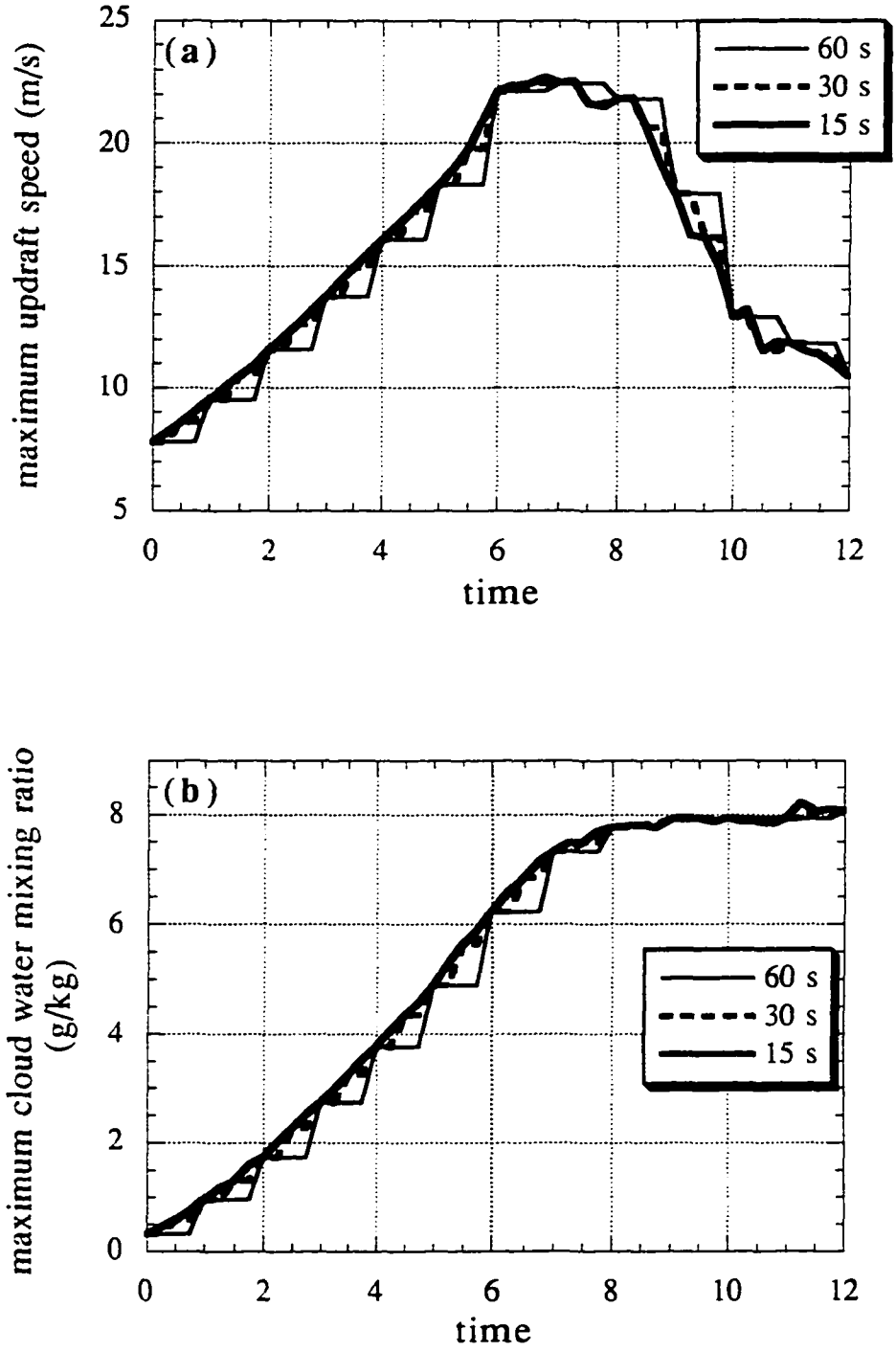


Figure 5.7 (a) Maximum updraft resolved as a function of ingest interval of simulated cloud fields. (b) Maximum cloud water mixing ratio resolved as a function of ingest interval of simulated cloud fields.

each having a volume of $(10m)^3$, and these are released into the modeled cloud. The spread in the final sizes (Fig. 5.8) is nearly a factor of three, and the 1673 μm drops from the $(50m)^3$ packet happen to be nearly in the upper tenth of the distribution for this particular case. (There are presumably cases where the drops grown within the larger packet would be much smaller than the average of the sub-packets, since this noise is probably of a random nature). Obviously each packet becomes highly convoluted by the end of a run in reality, and different drops within one packet may experience far different trajectories and environments. The summation of the drops over larger volumes to calculate the reflectivity field is an attempt to compensate for the distortion of the packets, and the model is intended only to capture the gross features of the reflectivity field evolution rather than the details of every trajectory anyway. A further decrease in packet size begins to erode the advantages of the coalescence-trajectory model, which can be run cheaply and quickly.

To estimate the noise from the limited number of trajectories represented, the locations of the initiation sites at cloud base are displaced horizontally and vertically. If the gross features of the reflectivity field are largely dependent on the initiation sites, then the number of trajectories represented is probably inadequate. In the first experiment, the packet initiation sites are displaced by 25 m in both horizontal directions. The maximum reflectivity (labeled "grdh" in Fig. 5.5) differs from the primary run by only ~1 dB at times, and the height of the maximum reflectivity (Fig. 5.5b) is identical to the primary run, except at the very end where it differs by 200 m. (The volumes over which the reflectivity is calculated are 200 m on each side, so this is only a difference of one volume lower). Lowering the initiation sites by 25 and 50 m similarly makes little difference (~ 1 dB) in the results (labeled "grdv" and "grdv2", respectively). The reflectivity patterns (not shown) for all the displacement experiments are nearly identical to those of the primary run. Thus it appears that the

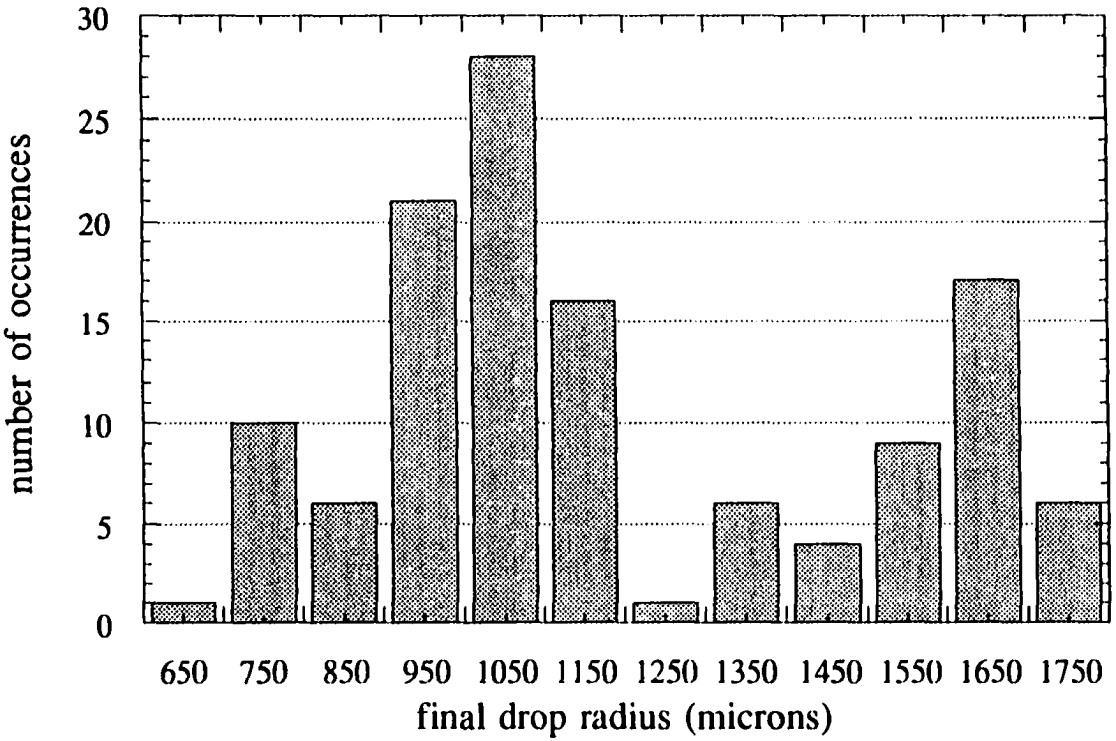


Figure 5.8 Final drop radii for 125 sub-packets.

gross features of the reflectivity field are captured by the limited number of trajectories used here.

5.1.4 UGA concentration sensitivity

The development of the modeled maximum reflectivity is obviously affected by the number concentration of UGA used in the model. The results of the primary run were produced by using nearly the highest UGA concentrations observed near the ground, but observations have shown that the concentration of UGA decreases with height, which should also be the case at the height of cloud base. Decreasing all UGA concentrations by the same factor decreases the reflectivity by a constant, and does not change the *rate* at which the reflectivity increases. For example, halving all UGA concentrations decreases the reflectivity only 3 dB when the UGA dominate the reflectivity, verified by the experiment labeled "uga/2" (Fig. 5.9). Similarly, decreasing the concentrations of all sizes of UGA by two orders of magnitude (labeled "uga/100") decreases the reflectivity by 20 dBZ. Decreasing the concentrations of the UGA does nothing toward changing the height of the maximum modeled echo.

The sizes of UGA dominating the modeled echo are those in the middle of the spectrum, 45-65 μm. Within the ten highest reflectivity volumes, the packets comprising the top 10 dBZ within each volume are sorted by their original UGA sizes (Fig. 5.10), for minutes 6 through 12, when the UGA dominate the reflectivity field. At the earliest times, the 65 μm UGA dominate, but the dominance shifts to the 55 μm and 45 μm sizes by the end of the time period. The rate of increase in maximum reflectivity by separate categories of UGA (Fig. 5.11a) shows this transition as well, between minutes ten and twelve. The largest UGA, 75-95 μm, contribute less to the reflectivity, because of their small concentrations. The reflectivity they do produce forms low in the cloud (Fig. 5.11b). The smallest UGA, 15-35 μm, while more

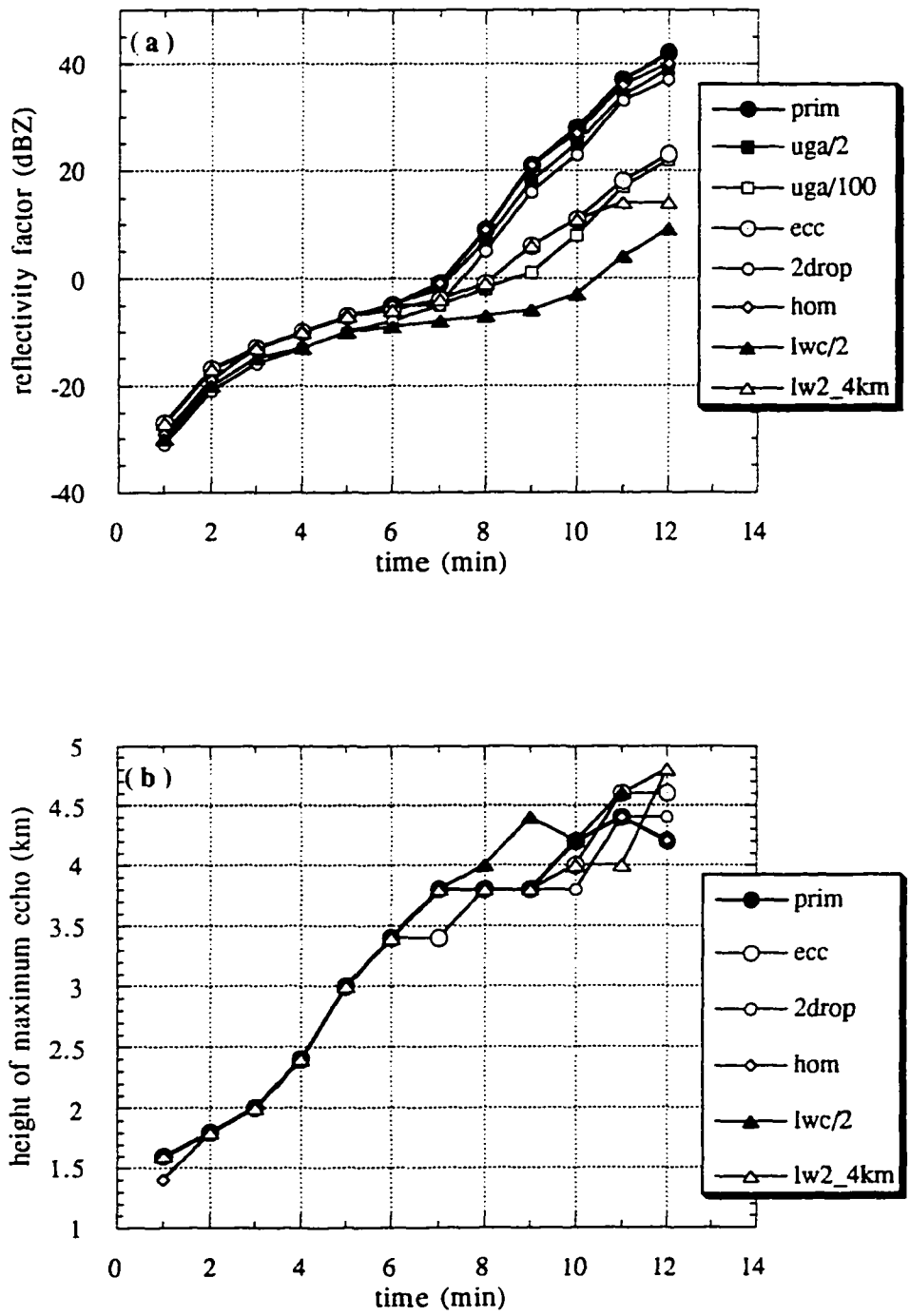


Figure 5.9 (a) Maximum echo calculated from cloud water and drops grown on UGA as a function of time, for all sensitivity tests. (b) Height of maximum echo plotted in (a).

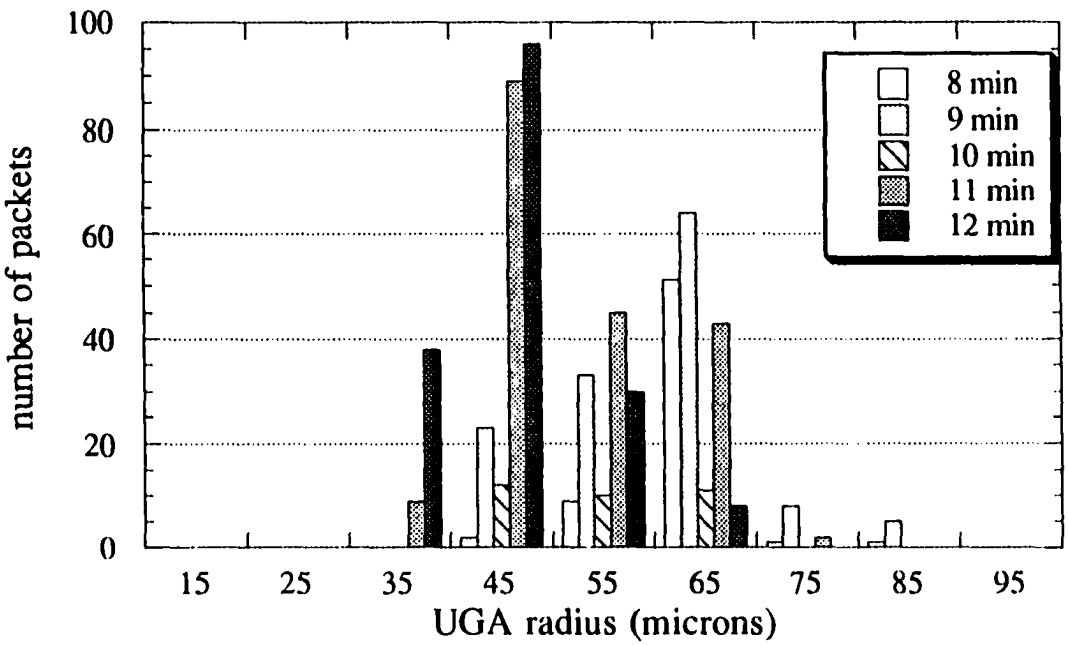


Figure 5.10 UGA contributing to highest 10 dBZ within the ten greatest reflectivity volumes, as a function of time. Bars signify number of packets within a given size category of UGA, at one minute intervals, from 8 to 12 min.

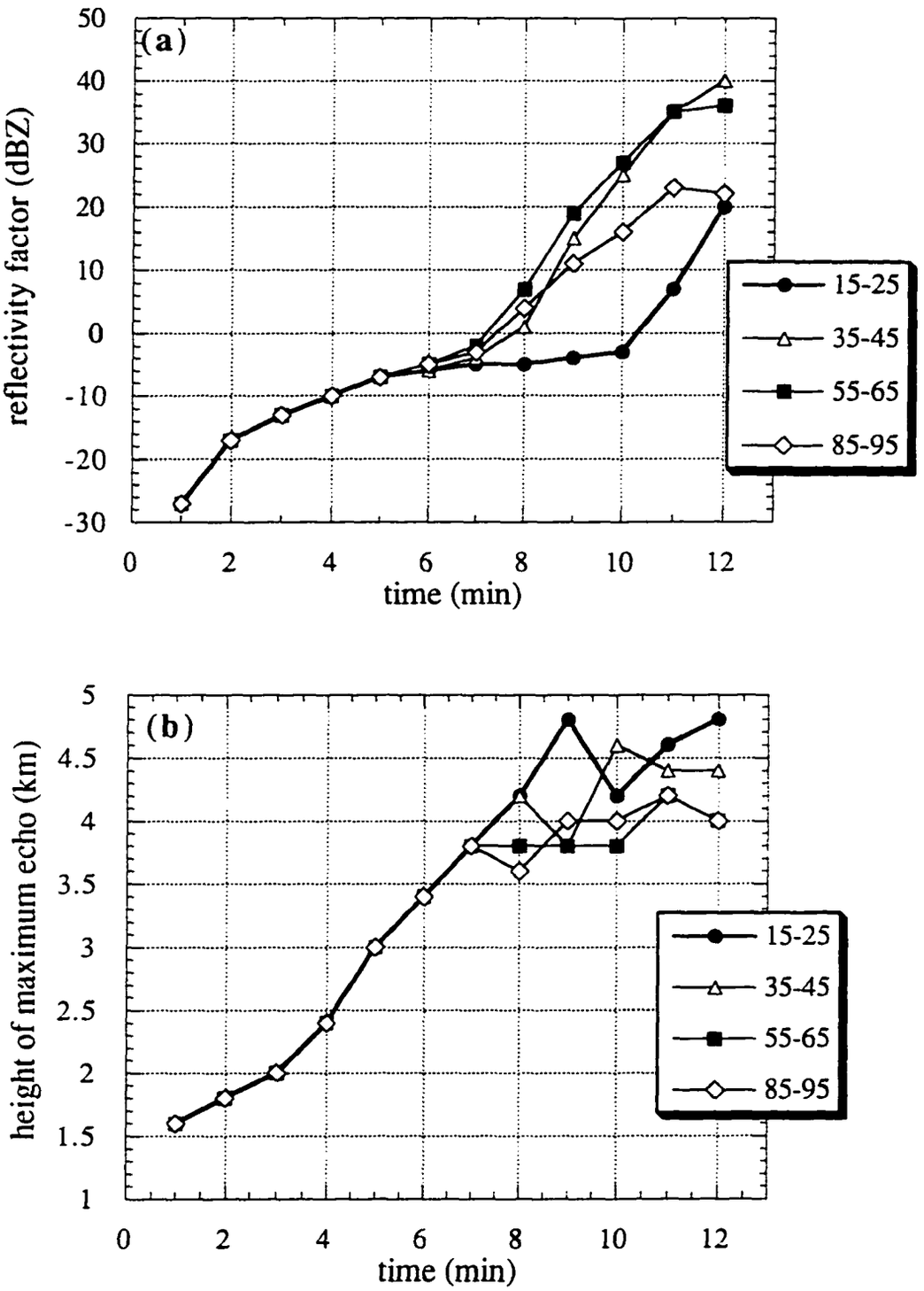


Figure 5.11 Maximum reflectivity factor calculated from cloud water and drops formed on specific size ranges (in μm) of UGA. (b) Height of maximum echo plotted in (a).

numerous than the larger particles, grow so slowly due to their low collision efficiencies that they contribute very little to the reflectivity until near the end of the run; the reflectivity they produce is located highest in the cloud.

5.1.5 Cloud droplet radius sensitivity (homogeneous mixing)

Although the aircraft observations indicate that inhomogeneous mixing is occurring at the edges of the cloud, there is probably some homogeneous mixing going on as well. The spatial scale of the microphysical data is approximately 100 m, while that used in the model is 50 m. At some smaller scale the mixing probably becomes homogeneous, and thus the sensitivity of the model to the mixing prescription is of interest. As opposed to inhomogeneous mixing, where the cloud droplet concentrations are reduced for sub-adiabatic cloud liquid water content, this sensitivity test uses homogeneous mixing, where the radii of the cloud droplets are shrunk according to the deficit from adiabatic liquid water content (while holding the concentration constant). Because the cloud droplet radii are reduced, the collision efficiencies are reduced as well, which slows the growth of the UGA and hence the reflectivity. Results (labeled as "hom" in Fig. 5.9) show only a slight decrease in the maximum reflectivity at the latest times, and the heights at which it occurs is the same as the primary run. Although the cloud droplets are shrunk at the cloud edges, those in the strongest part of the updraft are minimally affected because the liquid water content is so near the adiabatic value. It will be shown later in the trajectory analysis that the highest reflectivity packets, which dominate the reflectivity field of the cloud, ascend through the high liquid water content core of the cloud, which is barely affected by the mixing prescription used in the model.

5.1.6 Cloud droplet concentration sensitivity

High-rate droplet concentration data from the same day as the case cloud shows droplet concentrations as high as 1200 cm^{-3} in some instances (Alan Blyth, personal communication). Given that this value is twice that used in the primary run, the sensitivity to the overall cloud droplet concentration is tested. Although there is no explicit dependence on droplet concentration in the form of the continuous collection equation used here (8), there is a dependence on collision efficiency, which decreases due to the decrease in the adiabatic cloud drop radius as a function of height (Table 5.1). Results (labeled "2drop" in Fig. 5.9) show a decrease in the maximum reflectivity from the primary run as much as 4-5 dBZ, a larger sensitivity than in the homogeneous mixing experiment just discussed, because packets traveling through the core of the cloud are now affected as well.

5.1.7 Sensitivity to coalescence efficiencies

In the primary run and all tests discussed thus far, collision efficiencies rather than collection efficiencies have been used; all coalescence efficiencies have been assigned unity. Beard and Ochs (1984) present data for collector drops with radii from 50 to 501 μm that indicate coalescence efficiencies are often not unity. A table of collection efficiencies was created using their data, extended to larger radii by extrapolation[1]. These new collection efficiencies (Fig. 5.12, Table 5.2) decrease the maximum collection efficiencies to barely above 70%; the collision efficiencies used before were 100% (refer back to Fig. 4.1). The resulting reflectivity fields show that including the coalescence efficiencies has a large effect on the development of the radar echo (labeled "ecc" in Fig. 5.9), delaying the appearance of the 0 dBZ echo by one minute, reducing the maximum reflectivity at minute 12 by nearly 20 dB and raising the height of the maximum reflectivity at minute 12 by 200 m.

[1]Extrapolation of collection efficiency values to 2512 μm, although of debatable verity, seemed more logical than to leave the 100% collection efficiencies for drops larger than 501 μm.

Table 5.1 Cloud droplet radii assigned in the collection-trajectory model, as a function of altitude, for an adiabatic droplet concentration of 1200 cm^{-3}. Also listed are the radii used for an adiabatic droplet concentration of 600 cm^{-3}.

height (km)	radius (μm), 1200 cm^{-3}	radius (μm), 600 cm^{-3}
1.0	2.5	3.0
1.5	7.25	9.48
1.9	8.79	11.07
2.5	10.22	12.87
3.2	11.45	14.49
4.0	12.43	15.66
5.0+	13.32	16.77

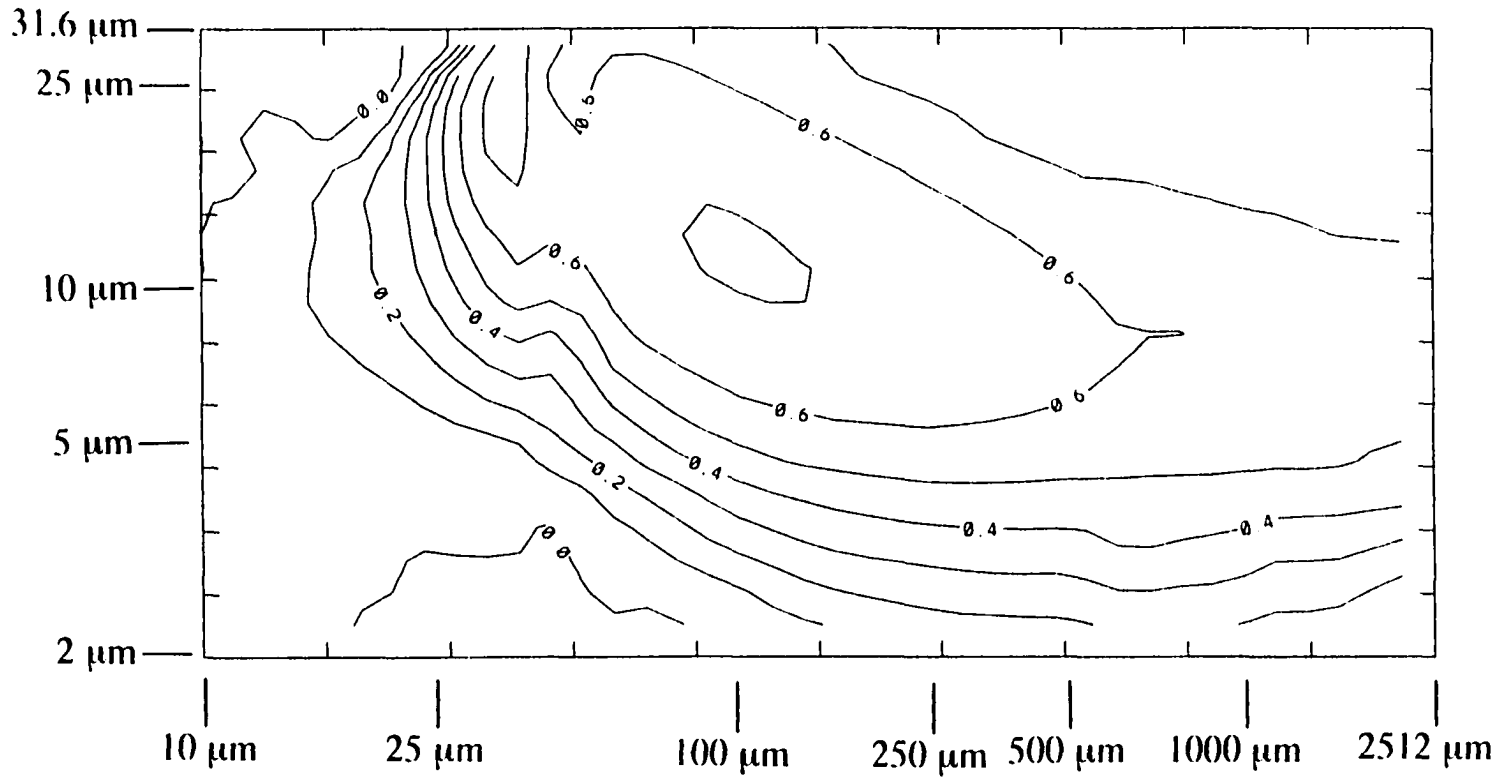


Figure 5.12 Collection efficiences used in the collection-trajectory model, including coalescence efficiencies of Beard and Ochs (1984).

Table 5.2 Numerical values (in percent) of collection efficiencies plotted in Fig. 5.12. Top row denotes collector drop radius in μm; farthest column to the left denotes smaller drop radius, in μm .

	10.	12.6	16.	20.	25.	32.	40.	50.	63.	79.	100.	126.	158.	200.	251.	316.	398.	501.	631.	794.	1000.	1259.	1585.	1995.	2512.
31.6	0	0	0	0	0	0	70.0	58.7	57.2	56.1	52.7	49.1	48.7	48.7	48.8	48.8	48.8	48.9	49.0	49.0	49.1	49.1	49.2	49.2	49.2
25.1	0	0	0	0	0	52.1	75.0	56.9	63.1	62.5	59.8	56.7	53.3	49.7	48.2	48.3	48.3	48.4	48.5	48.5	48.4	48.4	48.5	48.4	48.5
20.0	0	0	0	0	25.0	59.0	75.0	58.4	66.5	66.8	65.4	62.9	60.2	57.1	53.8	50.3	47.8	47.8	48.0	48.1	48.0	48.0	48.1	48.1	48.1
15.8	0	0	07.5	17.0	29.3	57.5	70.9	60.9	66.9	69.2	69.0	67.6	65.4	63.0	60.2	57.2	53.9	50.5	50.0	49.5	49.2	48.8	48.5	48.0	47.2
12.6	0	06.5	08.0	17.0	27.9	49.3	63.1	61.0	65.9	69.3	70.7	70.1	68.6	66.9	64.6	62.2	59.6	56.6	54.8	52.8	51.6	50.9	50.0	49.5	49.0
10.0	0	07.0	09.5	17.0	25.1	40.4	55.0	53.2	62.3	66.9	69.8	70.5	70.1	68.9	67.2	65.5	63.2	60.8	58.0	58.0	58.0	55.0	54.1	53.8	52.6
7.94	05.2	07.0	08.0	11.8	18.0	29.7	39.4	37.7	55.7	62.3	65.3	67.2	67.9	68.0	67.1	66.1	64.3	62.3	60.4	60.0	59.0	58.6	57.6	55.0	54.3
6.31	05.2	06.0	05.5	06.8	10.0	16.8	25.3	28.1	43.8	52.9	58.9	61.7	62.8	63.2	63.3	62.8	61.8	60.4	58.2	55.5	55.5	53.0	52.0	51.5	51.0
5.01	04.4	04.8	03.5	04.2	04.8	06.1	07.8	19.5	28.8	40.2	47.6	52.6	55.7	56.8	57.5	57.3	56.8	55.9	55.5	55.2	55.0	53.0	53.0	50.5	50.1
3.98	03.7	03.0	03.0	02.7	02.3	02.0	02.0	03.0	14.8	23.0	32.1	38.2	41.8	44.4	46.2	46.8	46.7	46.3	46.1	45.5	45.0	44.6	44.2	43.1	42.9
3.16	02.5	02.4	01.0	01.8	0	0	0	0	02.8	10.3	17.9	23.7	28.9	31.6	33.1	34.3	35.0	35.1	39.8	38.6	37.0	32.0	32.0	27.8	21.5
2.51	02.0	02.0	01.5	0	0	0	0	0	0	0	03.6	09.8	15.1	18.3	21.0	22.9	23.2	23.8	26.9	25.9	24.7	21.0	21.0	15.8	12.3
2.00	01.7	01.5	01.1	0	0	0	0	0	0	0	0	0	01.3	03.9	06.0	08.0	09.8	10.2	16.7	15.9	15.0	12.4	09.6	06.7	03.6

5.1.8 Sensitivity to cloud liquid water content

The sensitivity of the results to the cloud liquid water content is high. Because there are major uncertainties not only in the aircraft observations of cloud water, but also in the entrainment and mixing represented in the cloud simulation, it is necessary to test the sensitivity of the results to extreme variations in cloud water content. In the first experiment, the simulated cloud liquid water content is halved throughout the entire cloud. The resulting reflectivity field from the growth of the UGA in these conditions (including the use of coalescence efficiencies) is greatly reduced (labeled "lwc/2" in Fig. 5.9), by as much as 30 dB at later times. The development of the radar echo is delayed throughout the run: over 10 min pass before the appearance of the 0 dBZ echo which was observed at 7 min in the other tests. The height of the maximum reflectivity (Fig. 5.9b) is higher than in any of the previous experiments, because of the smaller drops. If there is a large bias in the simulated cloud water field, the growth of the UGA is greatly overestimated.

It is possible that the simulated cloud water is reasonable earlier in the cloud's lifetime, when entrainment has had less time to act. As the effects of entrainment become more important as the cloud ages, however, the simulated cloud water may be overestimated. To test the sensitivity of the calculations to the liquid water content in the upper part of the cloud, the simulated cloud water is halved only above 4 km. (A height of 4 km has been chosen because it is the observed height of the 0 dBZ echo, which is replicated well in most of the other runs). Results (labeled "lw2_4km" in Fig. 5.9) show the growth is retarded late in the run, and the height of the maximum reflectivity is still low in the cloud. As in the other experiments, once the UGA drops produce a reflectivity of 0 dBZ, they continue to grow very quickly afterward.

5.2 Raindrop Concentration

In addition to the radar echo produced by the drops grown on UGA, the amount of precipitation is also of interest. For the cloud studied here, the UGA are indeed capable of producing raindrops[2] in the upper regions of the cloud, in concentrations of hundreds per cubic meter within 8 min in the primary run (Fig. 5.13). By the end of the twelve-minute period, raindrop concentration is nearly 300 m^{-3}. This amount of precipitation is smaller than expected, because concentrations of UGA are ingested into the cloud in excess of 1900 m^{-3}. The difference lies in the fact that the 15 μm UGA never grow to be raindrops. As a result, the 25 μm UGA dominate the raindrop concentration because of their higher concentration (260 m^{-3}) than the larger sizes of UGA.

When non-unity coalescence efficiencies are included (labeled "ecc" in Fig. 5.14), raindrop concentration is slowed initially, but rebounds later in the run. The lower collection efficiencies delay the formation of raindrops initially, but later help to maintain greater concentrations of raindrops higher in the cloud. (The drops are growing at a slower rate than in the primary run, and because of their smaller size do not fall out as quickly. The difference in the sizes of drops produced by the primary run and the run with non-unity coalescence efficiencies is discussed in Section 5.3).

When the liquid water content of the cloud is halved (labeled "lwc" in Fig. 5.14), raindrop concentration is dramatically decreased. The 25 μm UGA which dominated the raindrops in the primary run no longer grow to raindrop size because of the reduced cloud water available for collection, and so the raindrop concentration is less than 100 m^{-3} until the very end of the run.

---

[2]Raindrops are designated as those drops with radii greater than 100 μm.

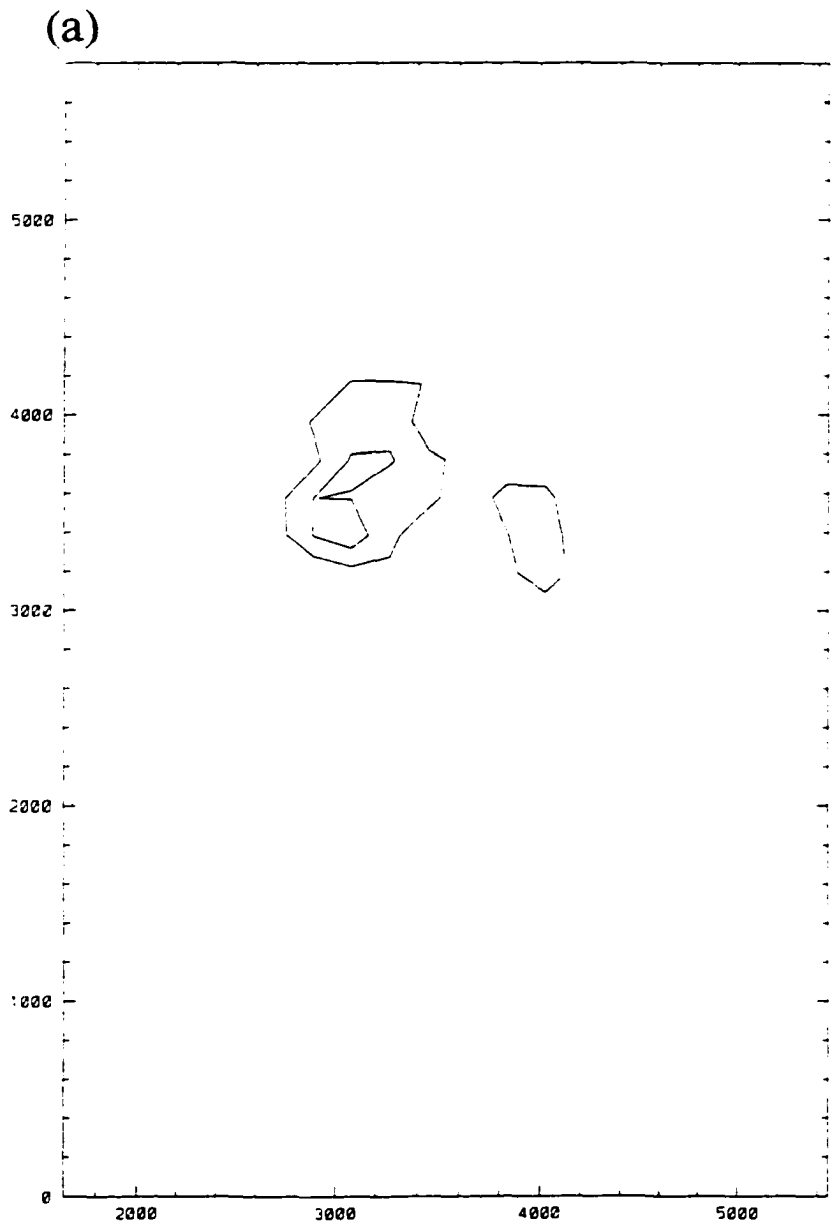


Figure 5.13 Vertical cross-sections of drizzle concentration for the primary run, after (a) 8 minutes, (b) 10 minutes and (c) 12 minutes. Contour interval is 50 m^{-3}.

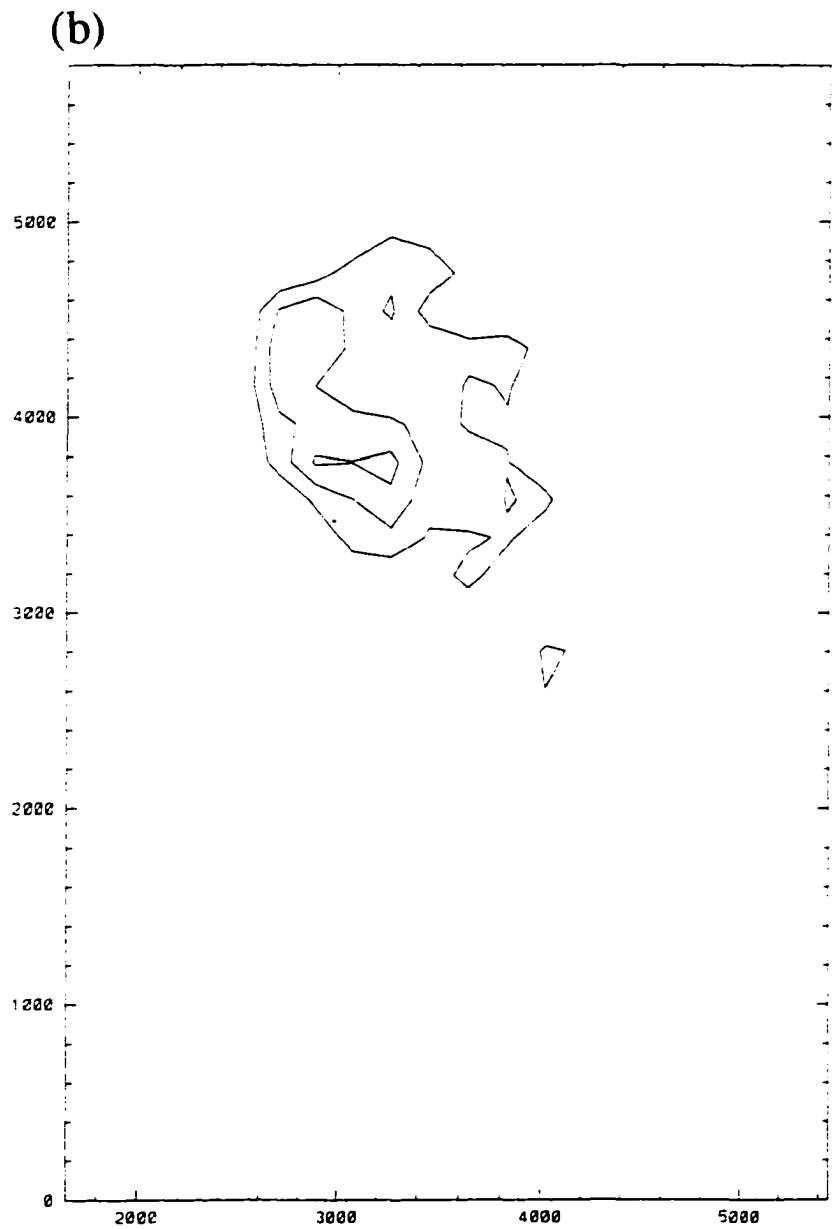


Figure 5.13 (continued).

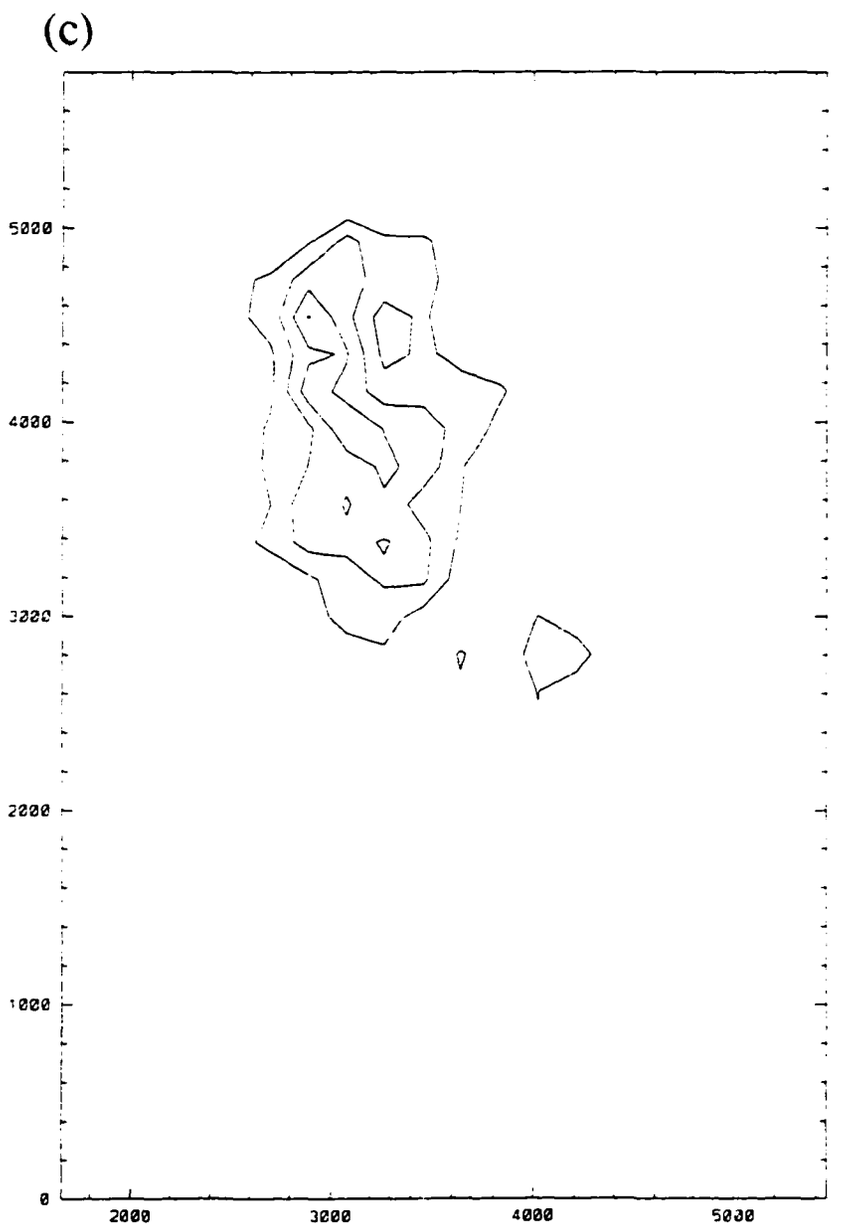


Figure 5.13 (continued).

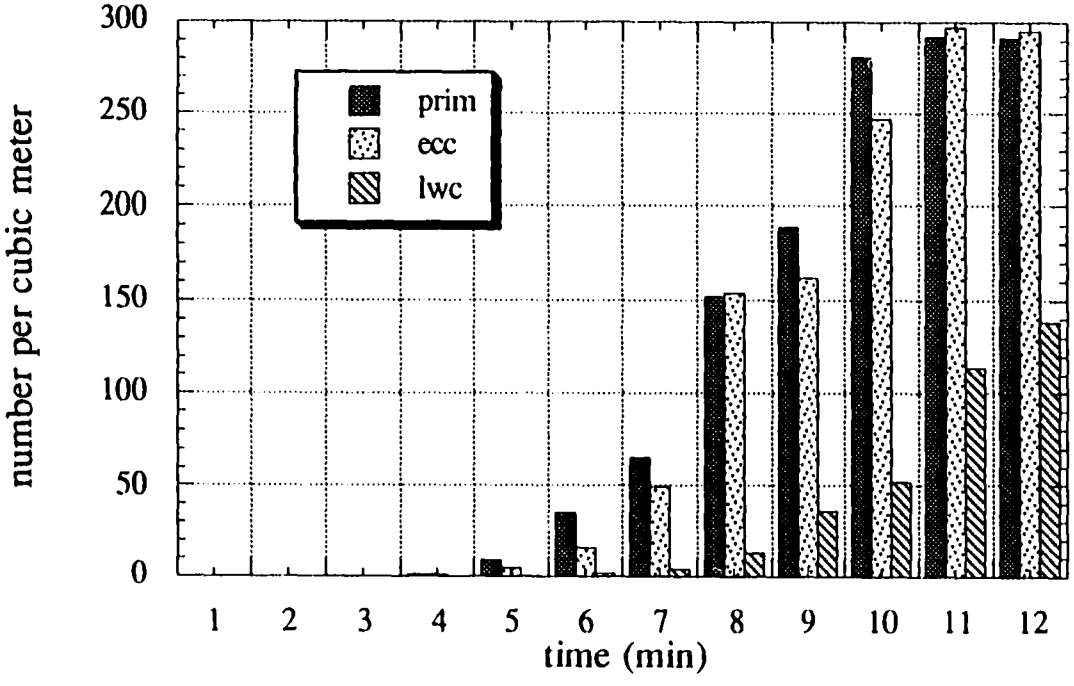


Figure 5.14 Maximum concentration of drizzle and raindrops, as a function of time for three different experiments.

5.3 Drop Spectra

Drop size distributions (here, those drops originating from UGA only) evolve much during the twelve-minute period the model is run. Plotting those distributions within the ten highest reflectivity volumes for the primary run (Fig. 5.15) shows an negative-exponential distribution early on (as expected, because the original UGA distribution is an negative-exponential one), which gradually becomes bimodal, and eventually flattens. Between 8 and 9 min, the distributions really start to break from their exponential form, and it is at this time that the reflectivity makes a significant jump, from -1 dBZ one minute earlier to > 9 dBZ in the primary run. Also at 9 min, the drop distributions develop a bimodal character, the secondary maximum being around 250 μm radius. At 11 min, three small peaks are evident in the distribution, as 50, 200 and 650 μm, but the entire distribution starts to flatten. By minute 12 the distribution is relatively flat between concentrations of 1 and 10 m^{-3} (per 50 μm bin width), corresponding to the concentrations of UGA initiated between 35 and 45 μm (which dominate the reflectivity at this time), although larger UGA could be contributing as well. Those drops in concentrations less than 1 m^{-3} $(50\ \mu m)^{-1}$ on the plots must be from UGA sizes greater than 45 μm. By the end of the run, drops are present in the cloud that have radii greater than 2 mm.[3] When the liquid water content from the drops over each of the ten volumes is computed, the maximum values range from 0.5 to 0.9 g m^{-3}. (The maximum simulated cloud water is greater than 5 g m^{-3}; this large difference in the amount of cloud water in the collector drops versus that collected justifies the neglect of cloud water depletion by the growth of the UGA in the model).

[3]Note that spontaneous breakup of the drops must be considered once the radii are greater than 4.5 mm, so the termination of the calculations at this time prevents the necessity of modeling drop breakup.

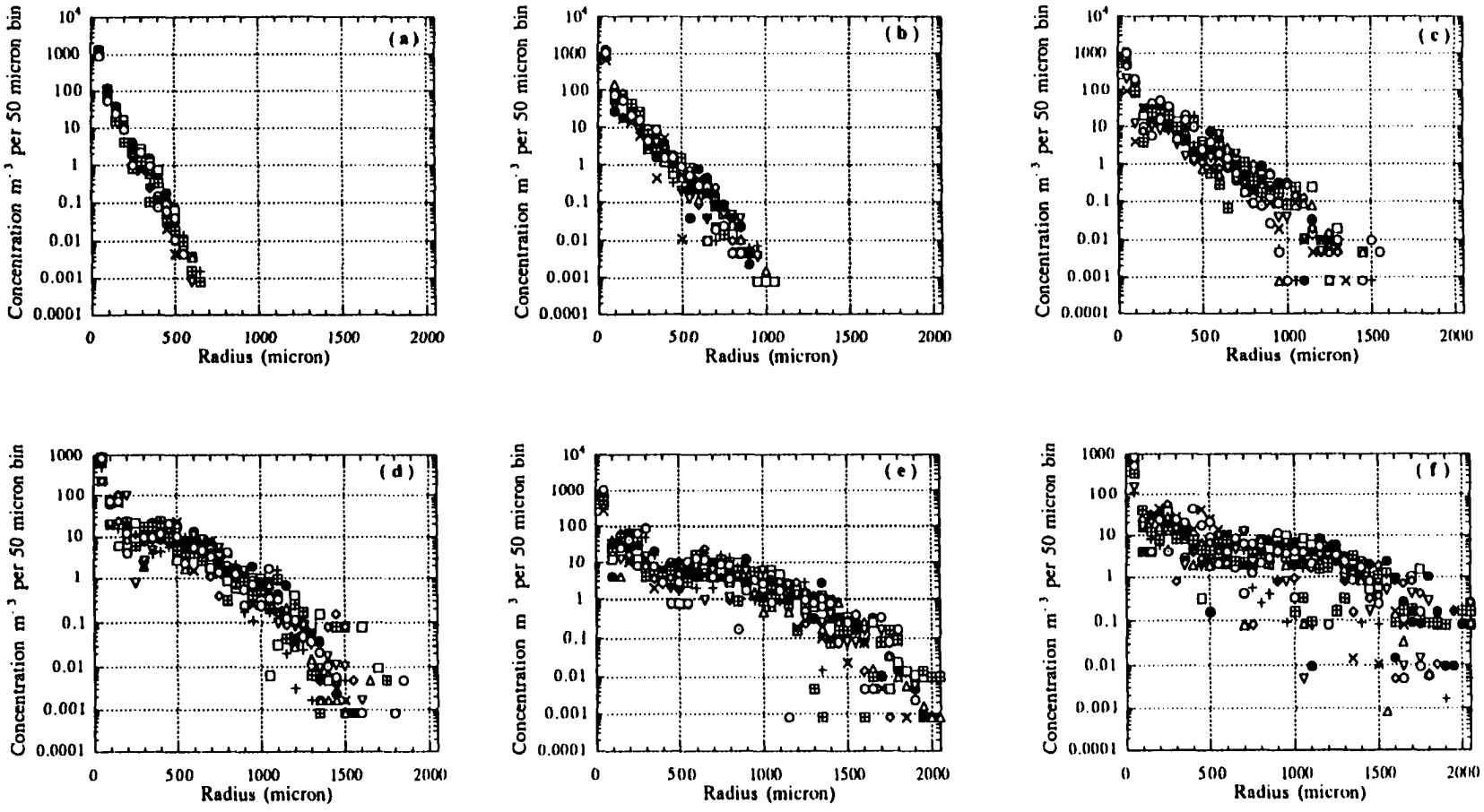


Figure 5.15 Size distributions of drops grown on UGA within the ten highest reflectivity volumes for the primary run, for minutes (a) 7, (b) 8, (c) 9, (d) 10, (e) 11 and (f) 12.

Sensitivity of the drop distributions to coalescence efficiencies and cloud water is high. When coalescence efficiencies are included, the evolution of the drop size distribution is similar but slower (Fig. 5.16). The decrease in the collection efficiencies at larger drop sizes narrows the spread in the distributions from the individual volumes, presumably because the fastest growth of the most fortunate drops is moderated. The bimodality does still develop in this case, although later in the run. When the cloud water is halved, the distributions barely depart from their original negative-exponential shape (Fig 5.17). The drops grow very slowly in this case, so that the stage at which the distribution flattens is not reached. Some bimodality is evident at 11 and 12 min.

Some interesting characteristics of drop size distributions from the UGA are the bimodality that develops and the non-exponential character of the distributions at later times. A secondary peak in the distributions is always initiated near 150 μm radius, where the collection efficiencies have a subtle jump in value. At later times, but before drop breakup is important, the flattening of the distributions occurs at a concentration of the most important UGA. The non-exponential character of the drop distributions at the later times is perhaps realistic, and might evolve toward an negative-exponential distribution if the calculations were carried out further, when drop breakup processes become important.

5.4 Growth Trajectories

Packet trajectories provide additional insight into the growth of the UGA in the model. The packets are all released from cloud base, and ascend via the updraft. Little difference is found in the locations of the different sizes of UGA early in the run (Fig. 5.18), because although there is a range of terminal velocities of the UGA (~0.03

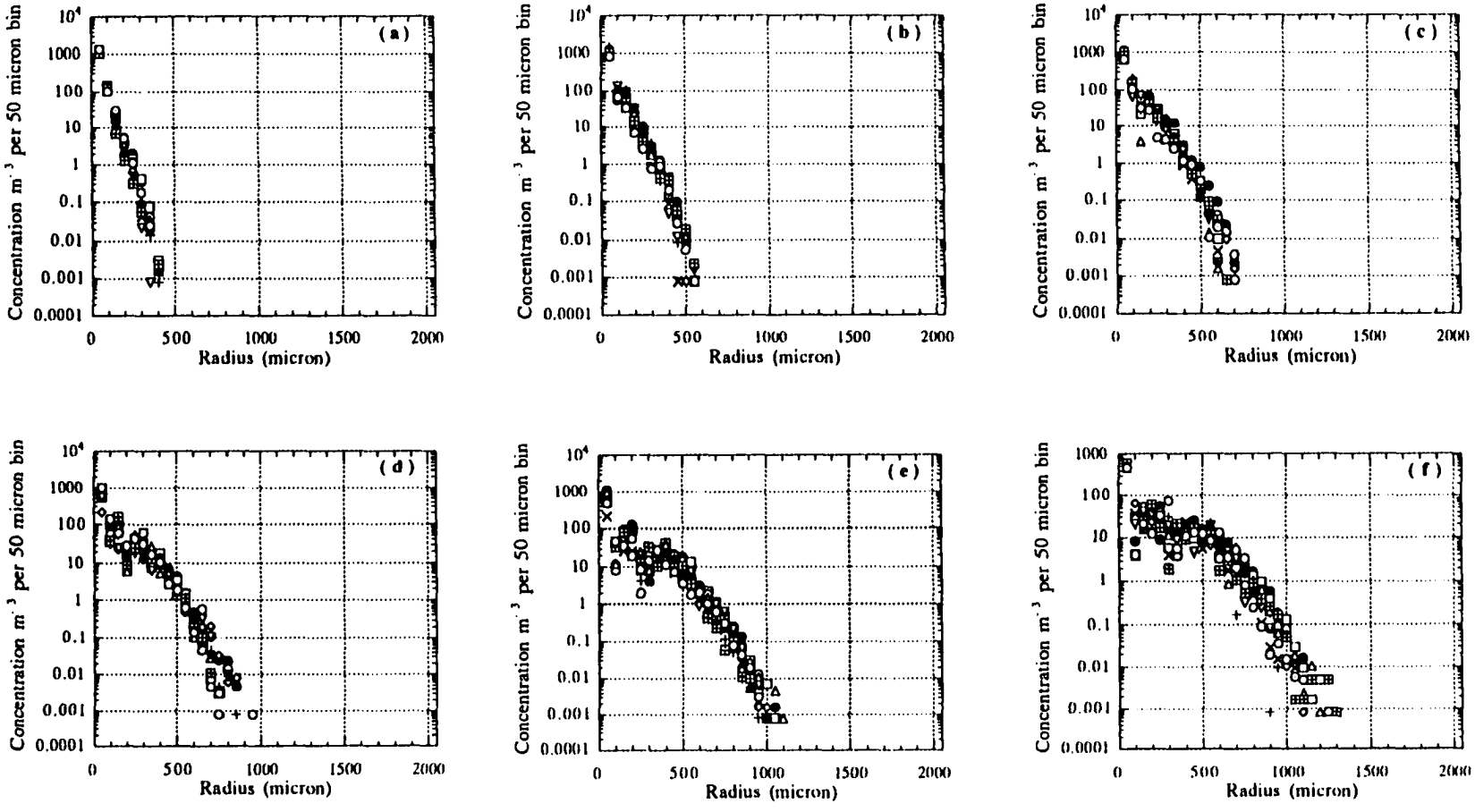


Figure 5.16 As in Fig. 5.15, except for the experiment in which non-unity coalescence efficiencies are included.

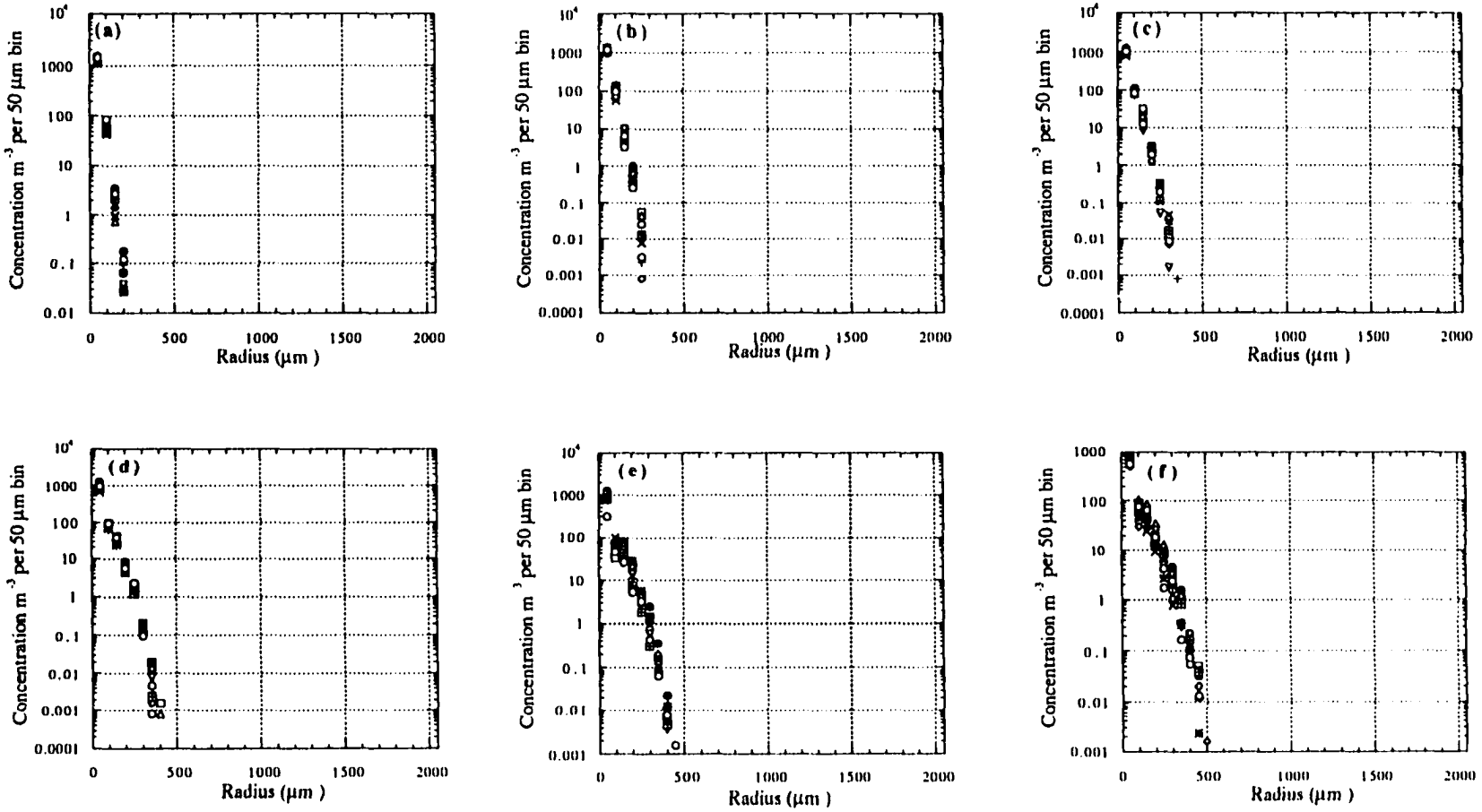


Figure 5.17 As in Fig. 5.15, except for the experiment in which the simulated cloud water content is halved.

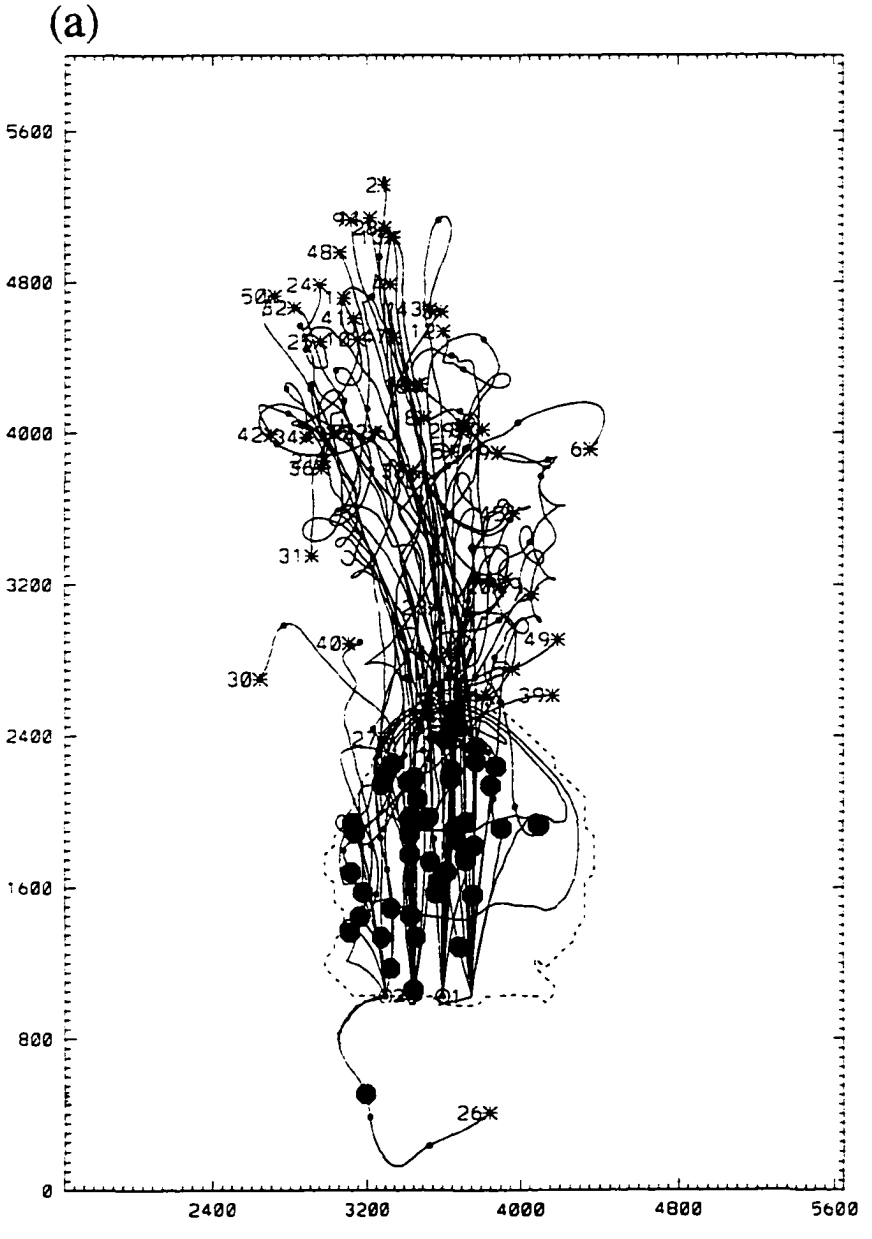


Figure 5.18 Randomly-chosen packet trajectories at 4 minutes for UGA of (a) 15 μm radius, (b) 45 μm radius and (c) 95 μm radius, overlayed on vertical cross-section of simulated cloud water content (contour interval 1 g m^{-3}). Entire trajectories are plotted, with current locations marked by black circles.

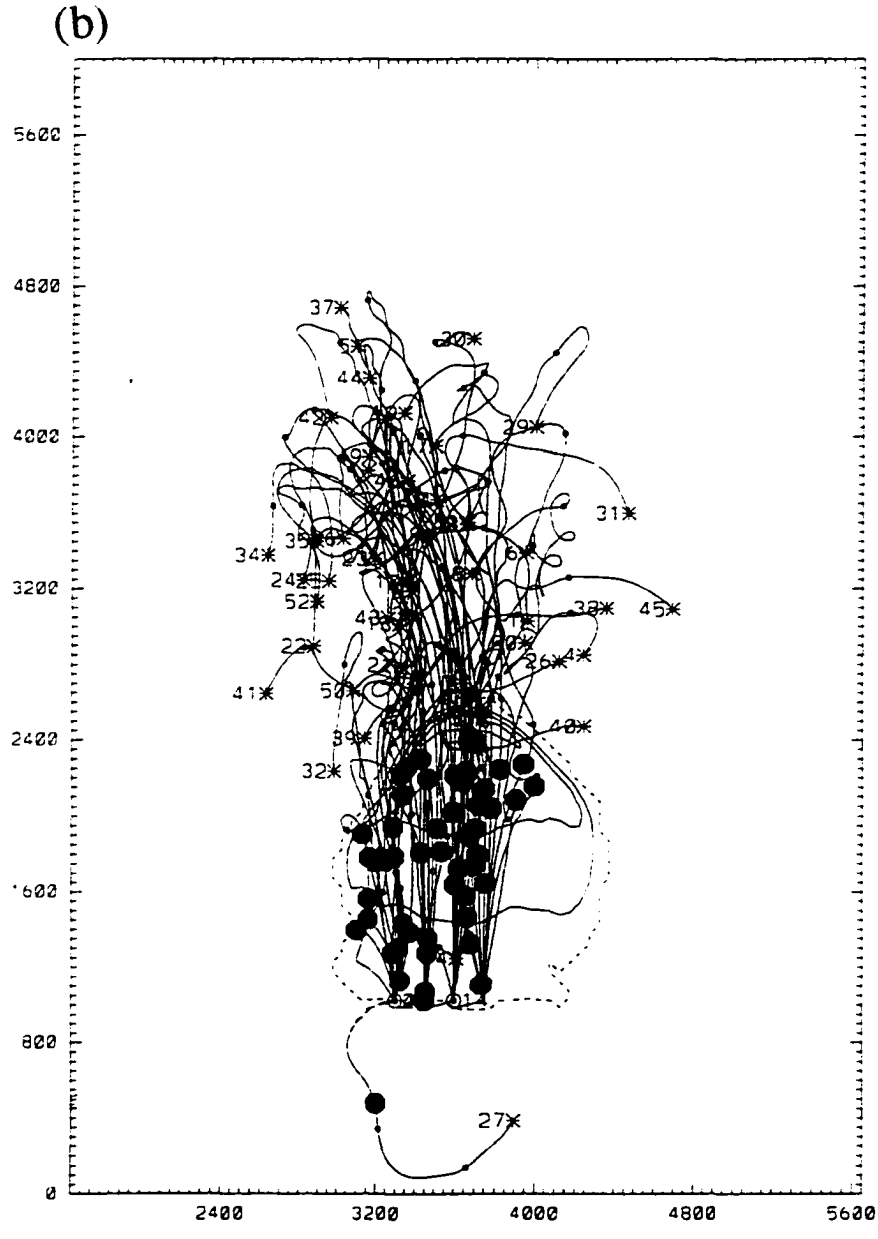


Figure 5.18 (continued).

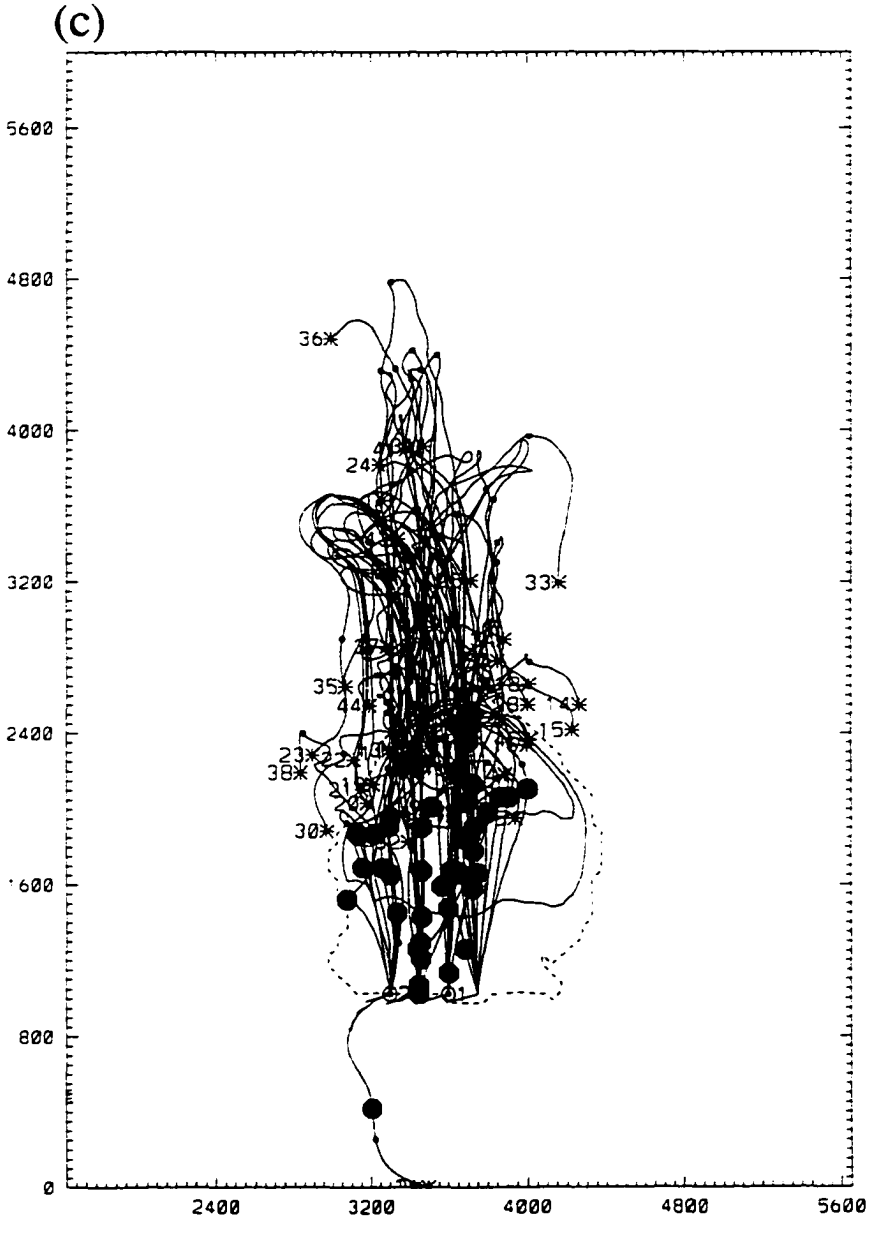


Figure 5.18 (continued).

m s^{-1} at 15 μm radius to ~0.7 m s^{-1} at 95 μm radius), they are much less than the cloud updraft at this time (up to 15 m s^{-1} maximum). The spatial distribution of the number of packets within the cloud is nearly the same, regardless of the size of the UGA within them (Fig. 5.19). Although the larger UGA are more efficient collectors, their growth is limited by the little cloud water present at this time. As time goes on, however, the liquid water content of the cloud increases, and the larger UGA grow more quickly. As the larger UGA grow increasingly larger drops, their terminal velocities also increase, causing them to ascend through the cloud more slowly than the smaller UGA (Figs. 5.20 and 5.21). (The separation of the packets of UGA evident in the middle of the cloud in Fig. 5.21 is due to a minimum in the vertical velocity in this area, causing the top of the simulated cloud to ascend faster than the middle). Large eddies near cloud top start to push particles out of the main updraft at this time, into areas of weaker updraft and less cloud water. The largest drops formed on UGA start to fall, but do not grow nearly as quickly because of the decreased cloud water available for collection. This, as well as their small concentration, prevents the formation of a secondary maximum in reflectivity in the lower part of the cloud. After more time, the cloud updraft weakens and downdrafts as well as updrafts occupy the upper parts of the cloud. More large particles formed on UGA begin descending (Figs. 5.22 and 5.23), and those large drops that were ascending find it difficult to get to the highest liquid water content region. Finally, downdrafts occupy the entire upper region of the cloud, and cloud water has been greatly decreased by evaporation. All the drops grown on UGA start to descend at this time (Figs. 5.24 and 5.25).

Snapshots of randomly-chosen packet trajectories are useful for conceptualizing the overall growth, but the trajectories of those packets contributing the most to the reflectivity are of paramount interest. Trajectories of the packets contributing the most to the maximum echo show that they are carried straight up the

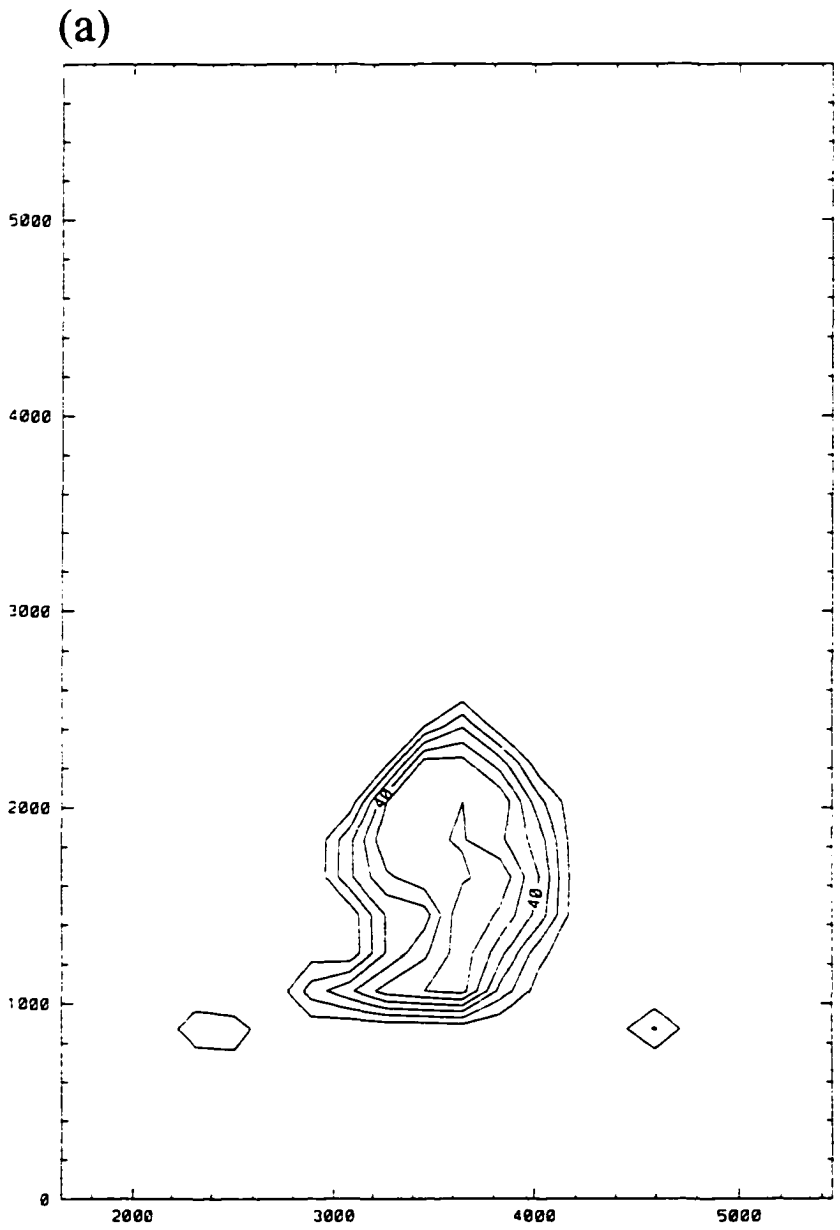


Figure 5.19 Spatial distribution of packets, per (200 m)^3 volume, at 4 minutes for UGA of (a) 15 μm radius, (b) 45 μm radius and (c) 95 μm radius. Contour increment is 10 packets.

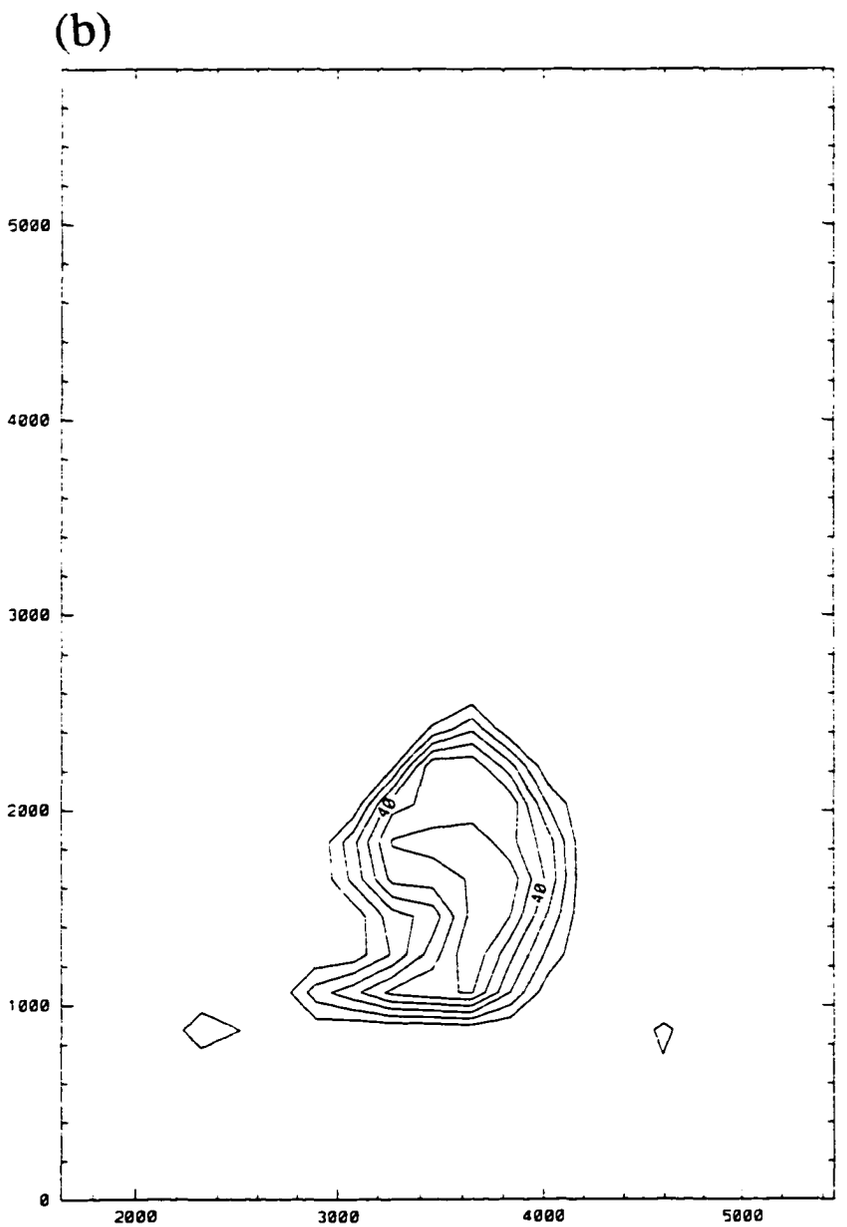


Figure 5.19 (continued).

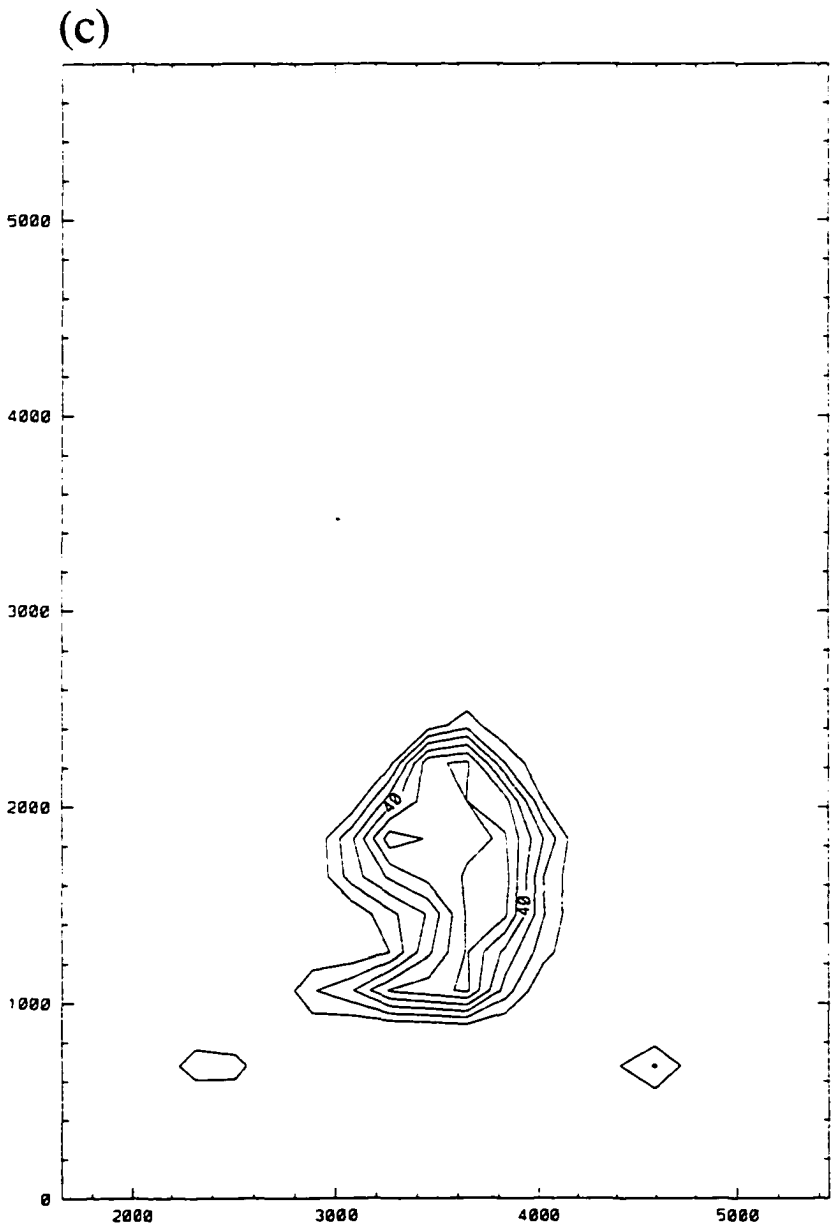


Figure 5.19 (continued).

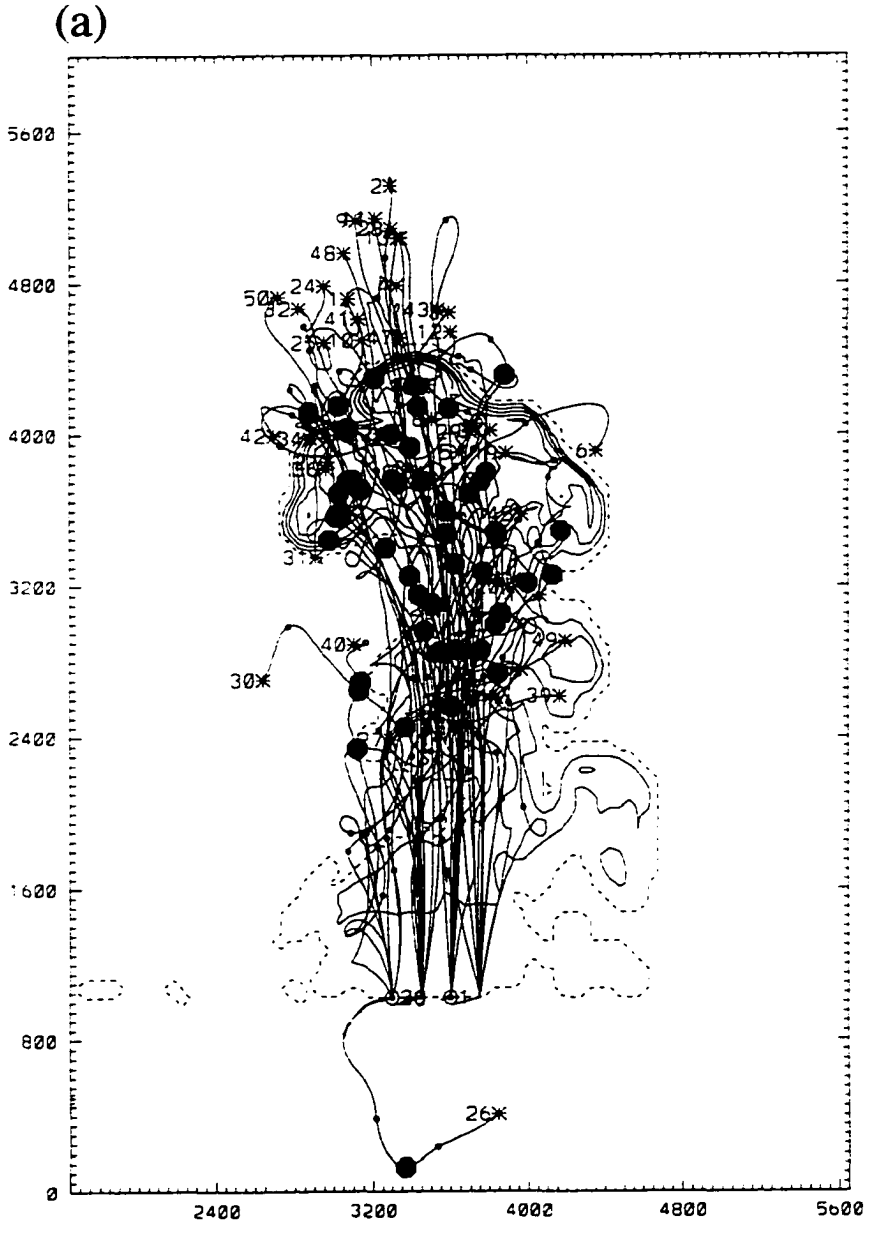


Figure 5.20 As in Fig. 5.18, except at 8 minutes.

(b)

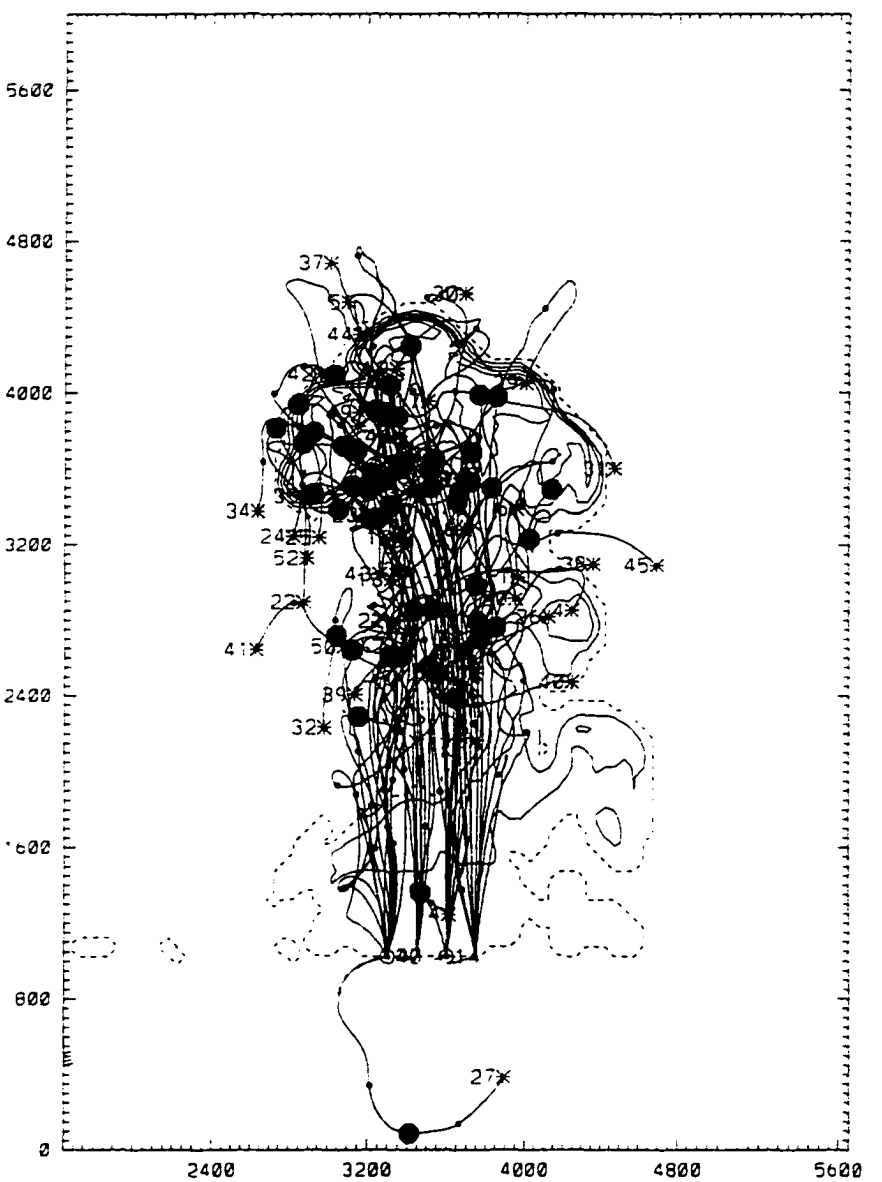


Figure 5.20 (continued).

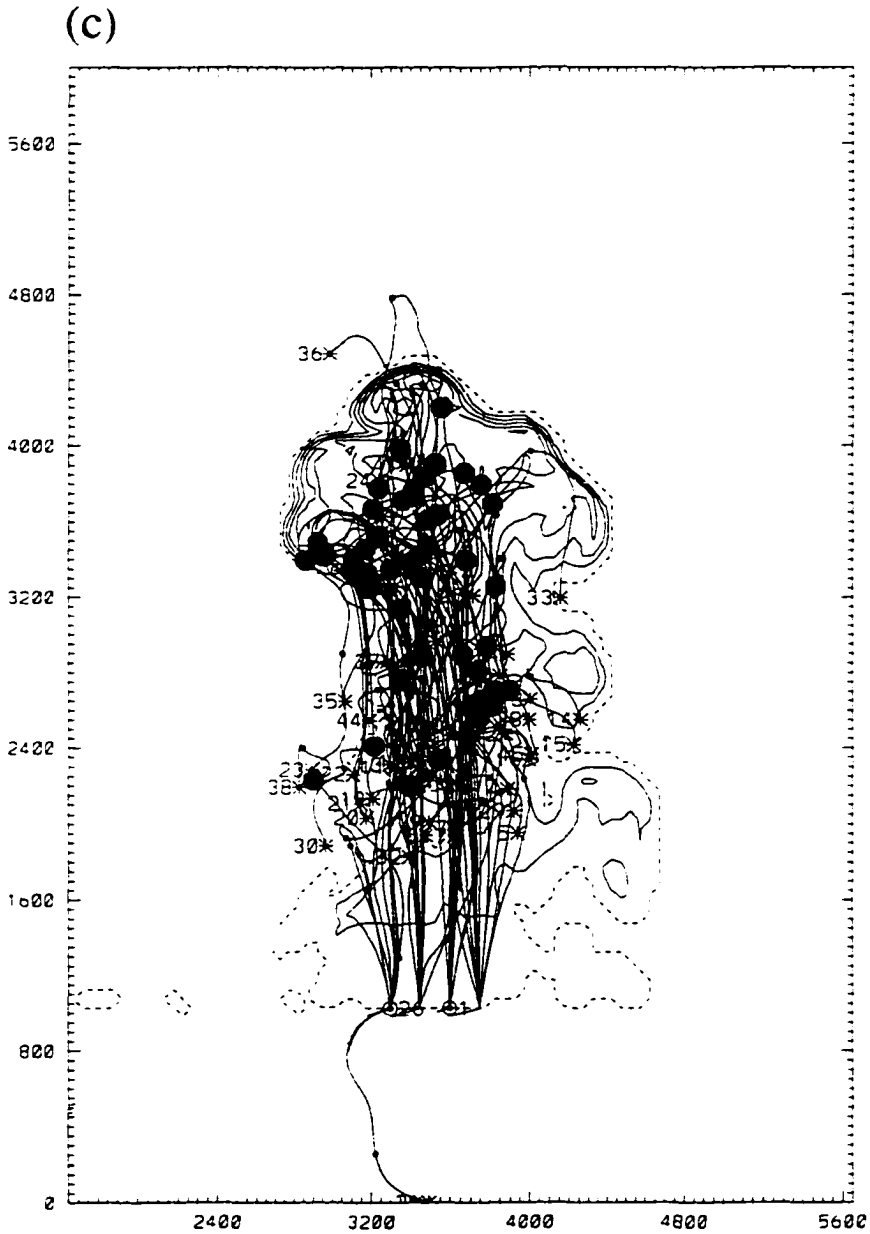


Figure 5.20 (continued).

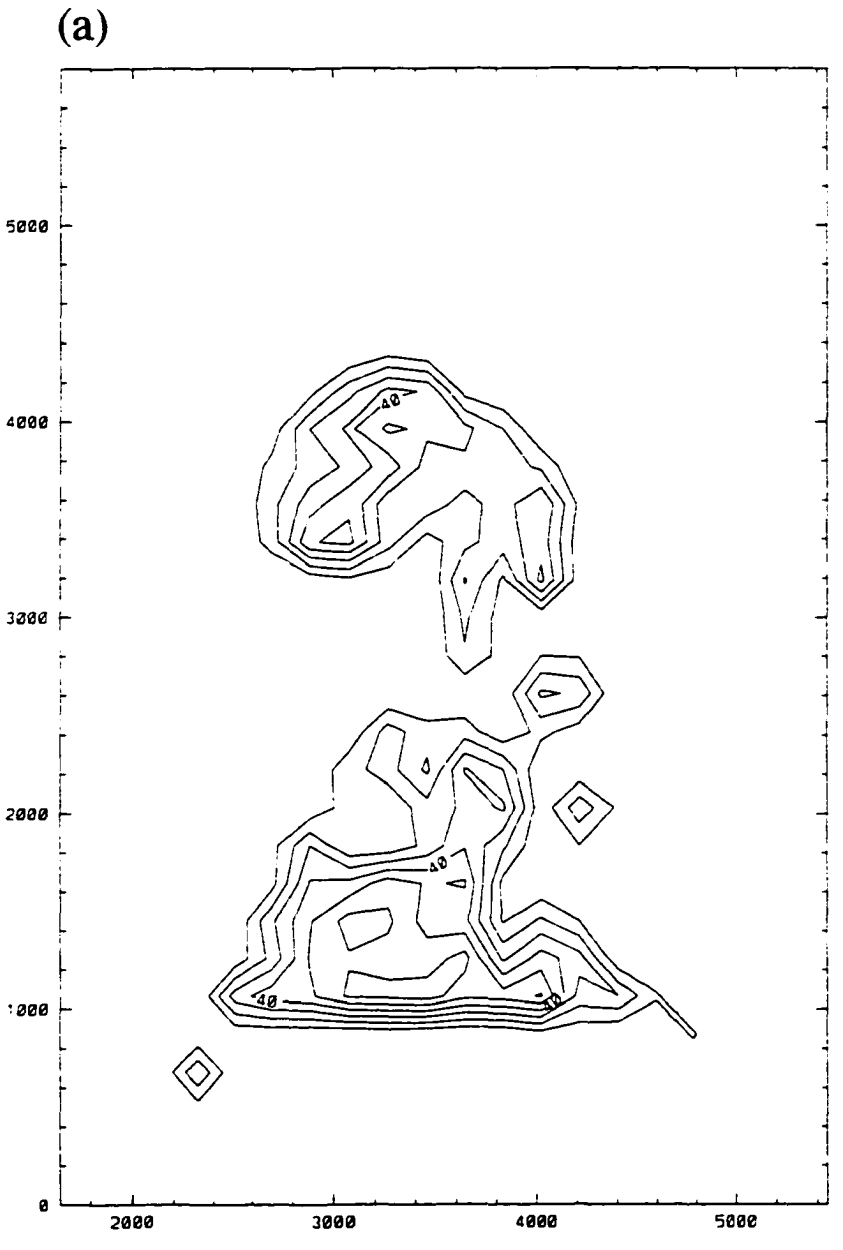


Figure 5.21 As in Fig. 5.19, except at 8 minutes.

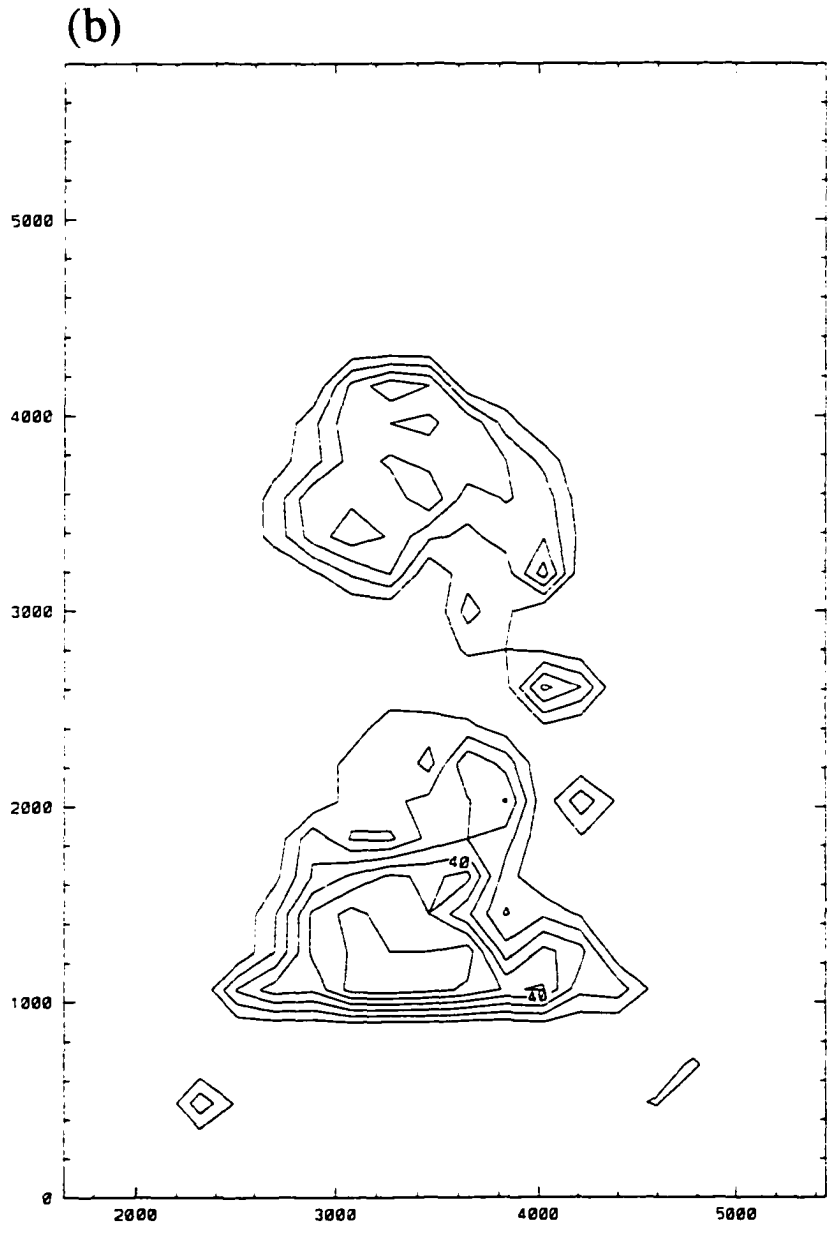


Figure 5.21 (continued).

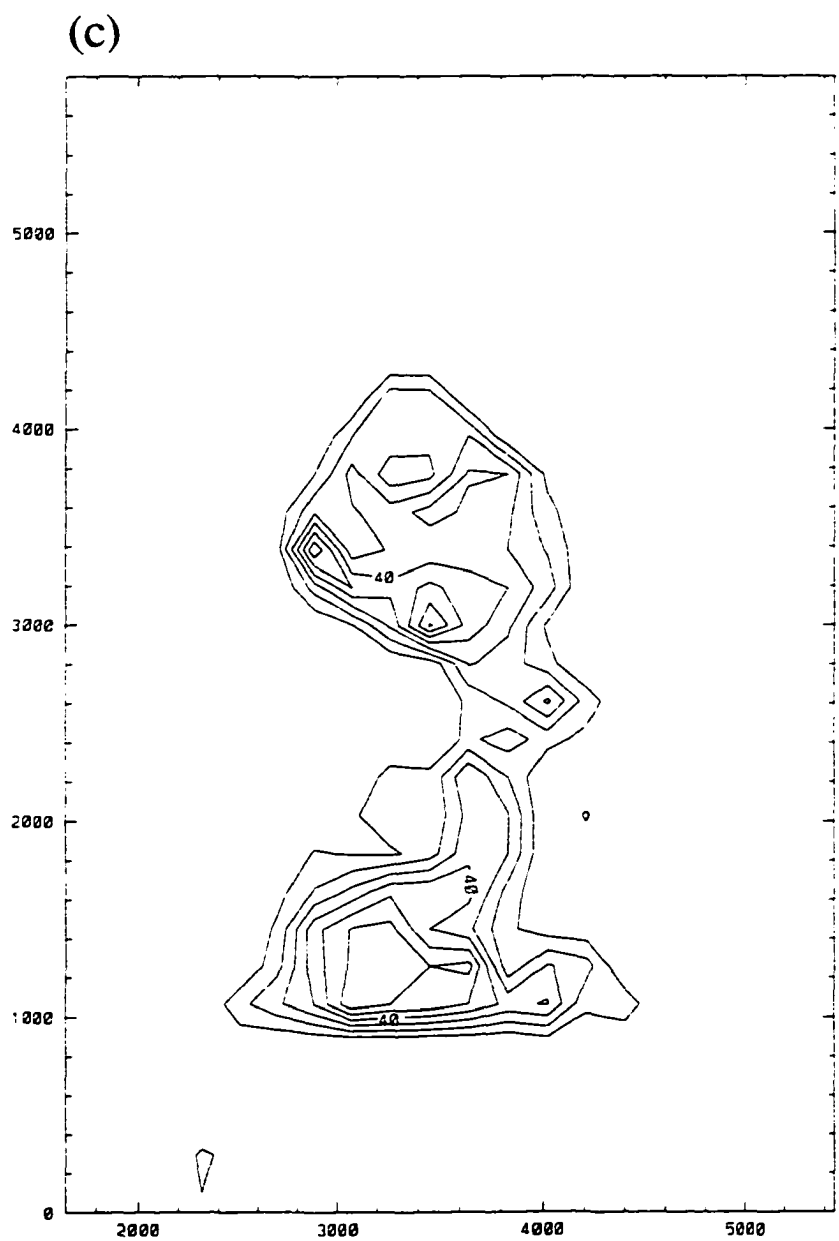


Figure 5.21 (continued).

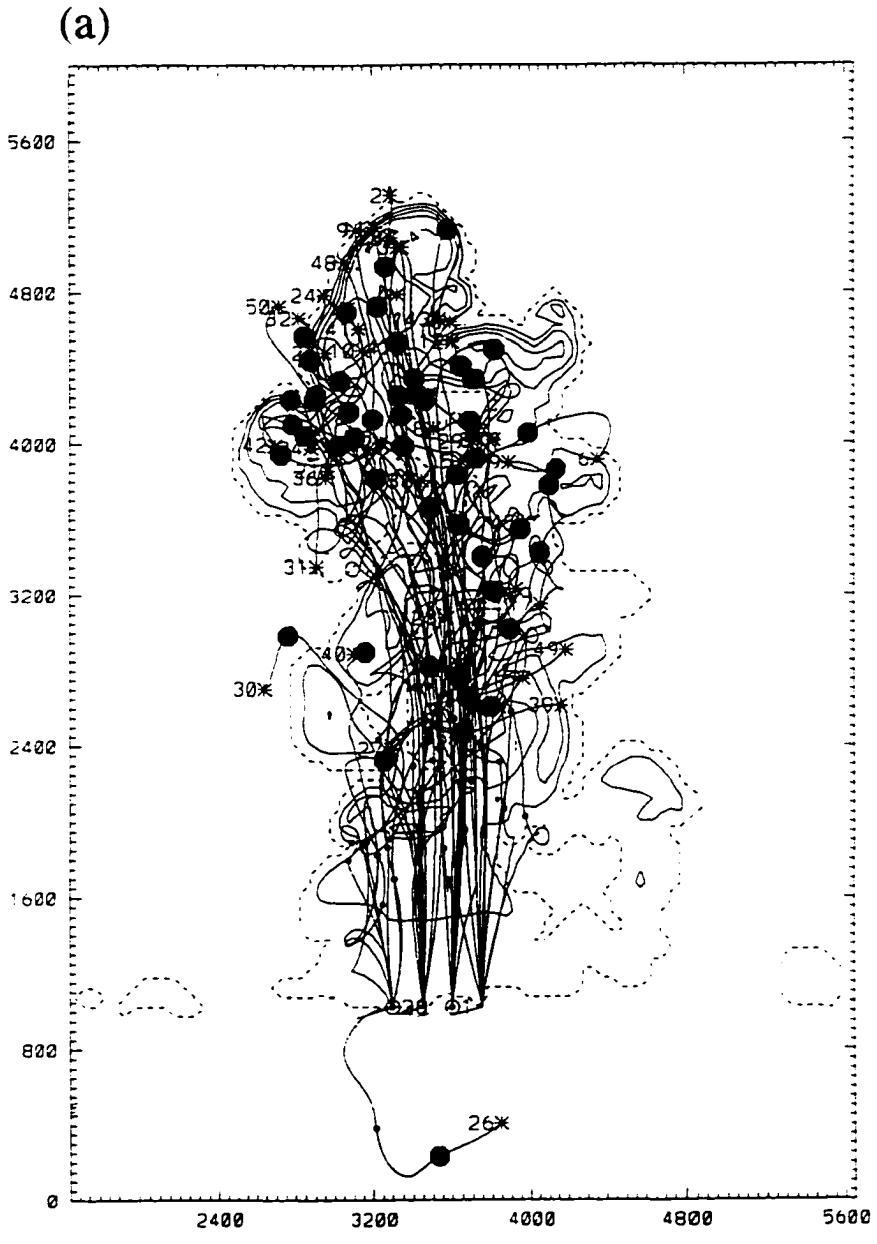


Figure 5.22 As in Fig. 5.18, except at 10 minutes.

(b)

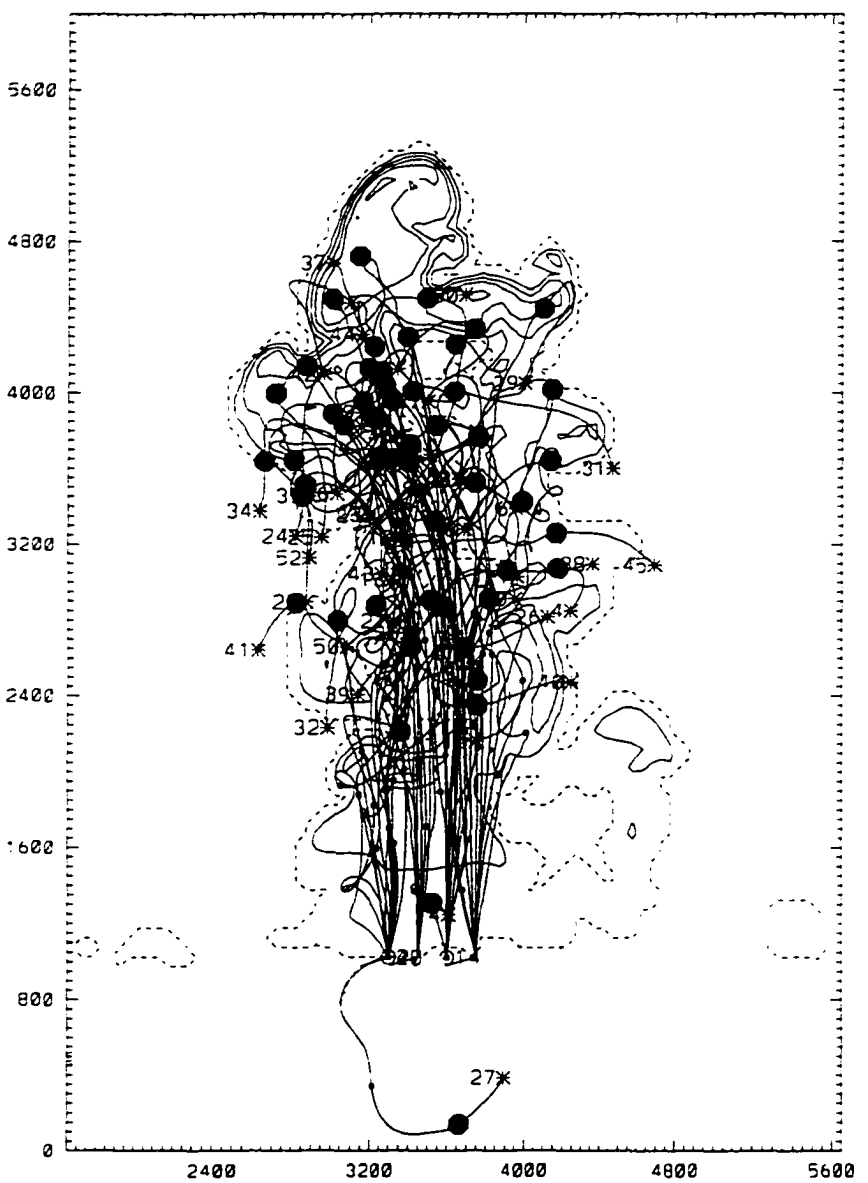


Figure 5.22 (continued).

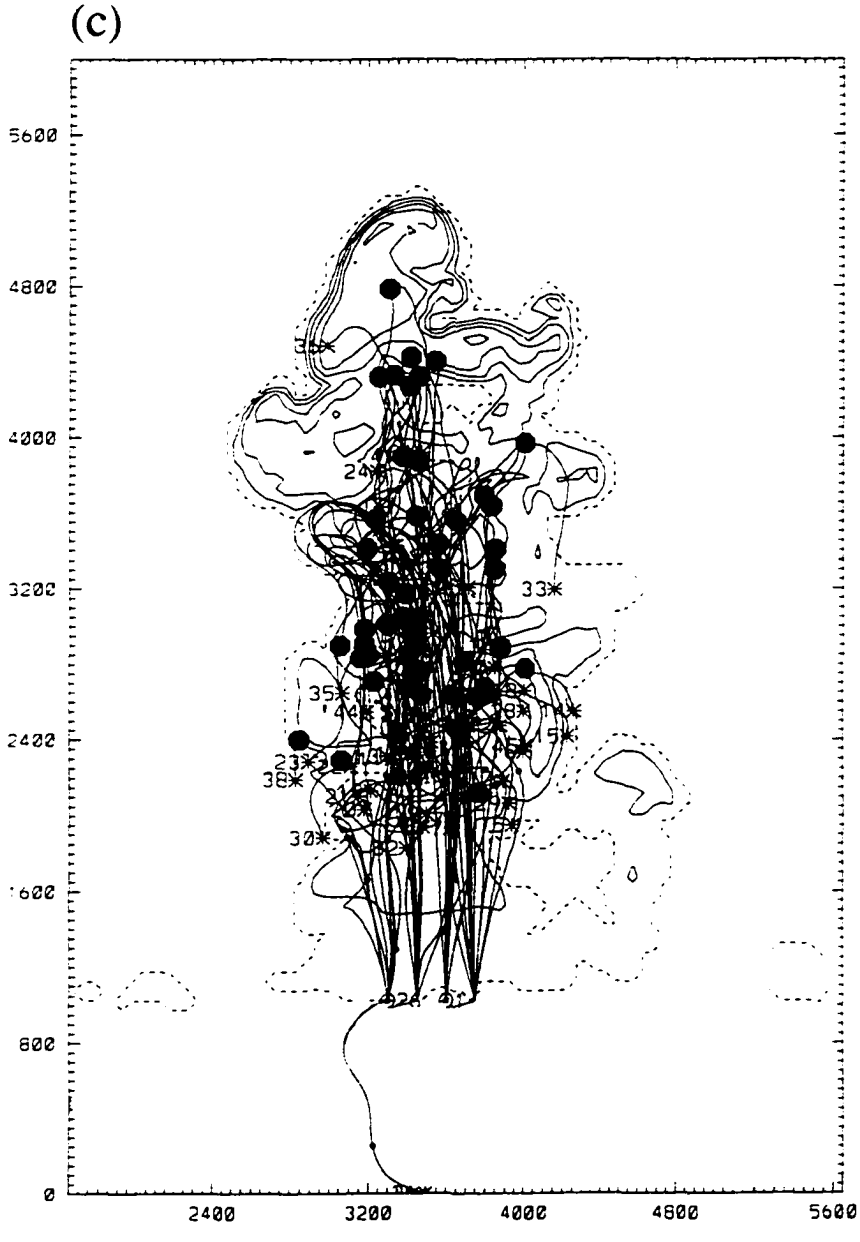


Figure 5.22 (continued).

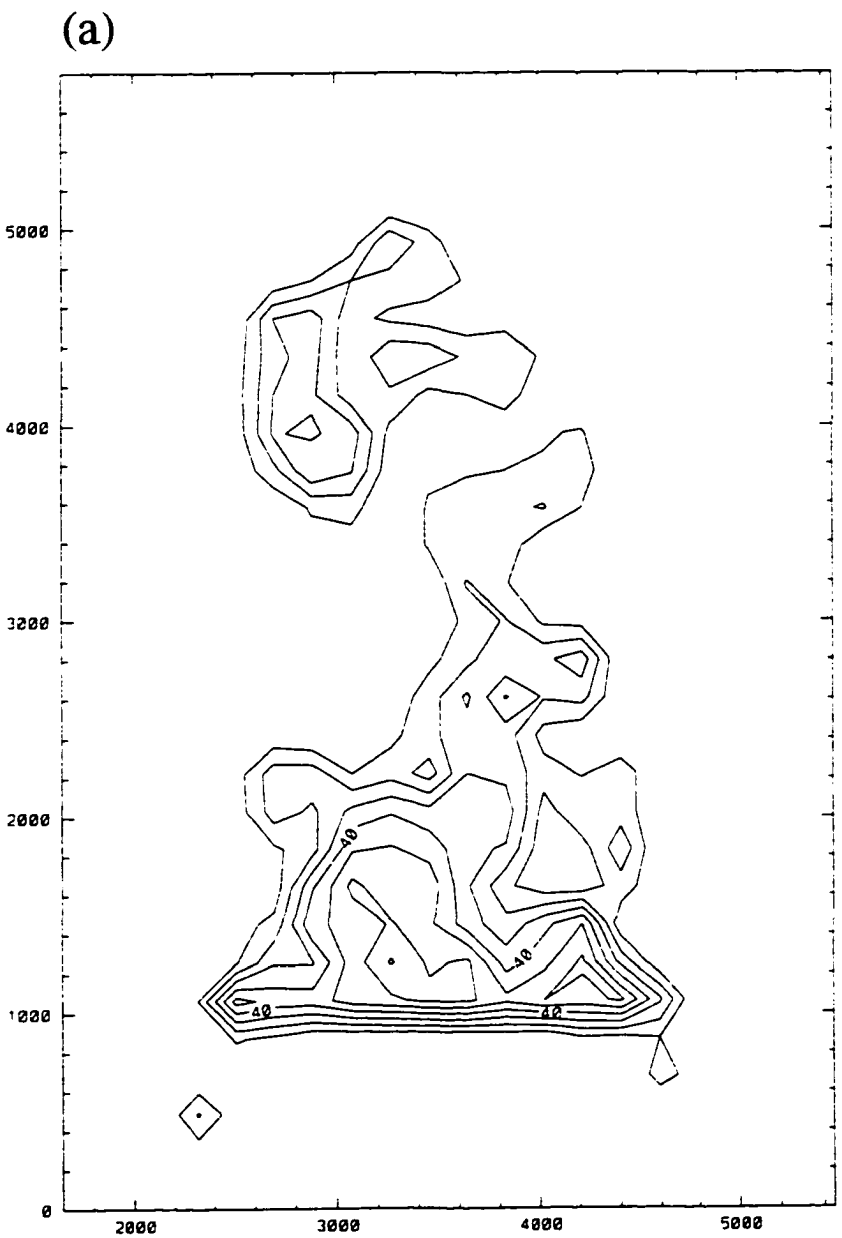


Figure 5.23 As in Fig. 5.19, except at 10 minutes.

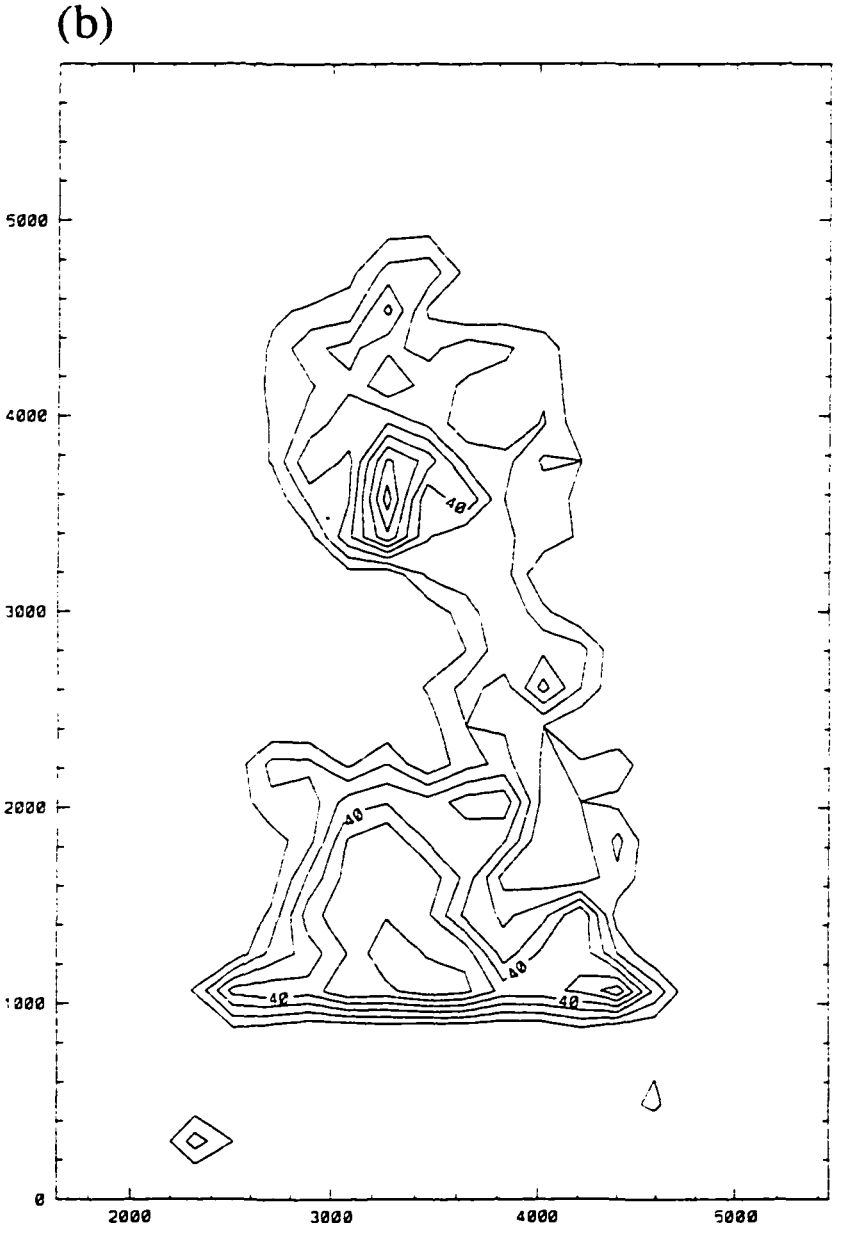


Figure 5.23 (continued).

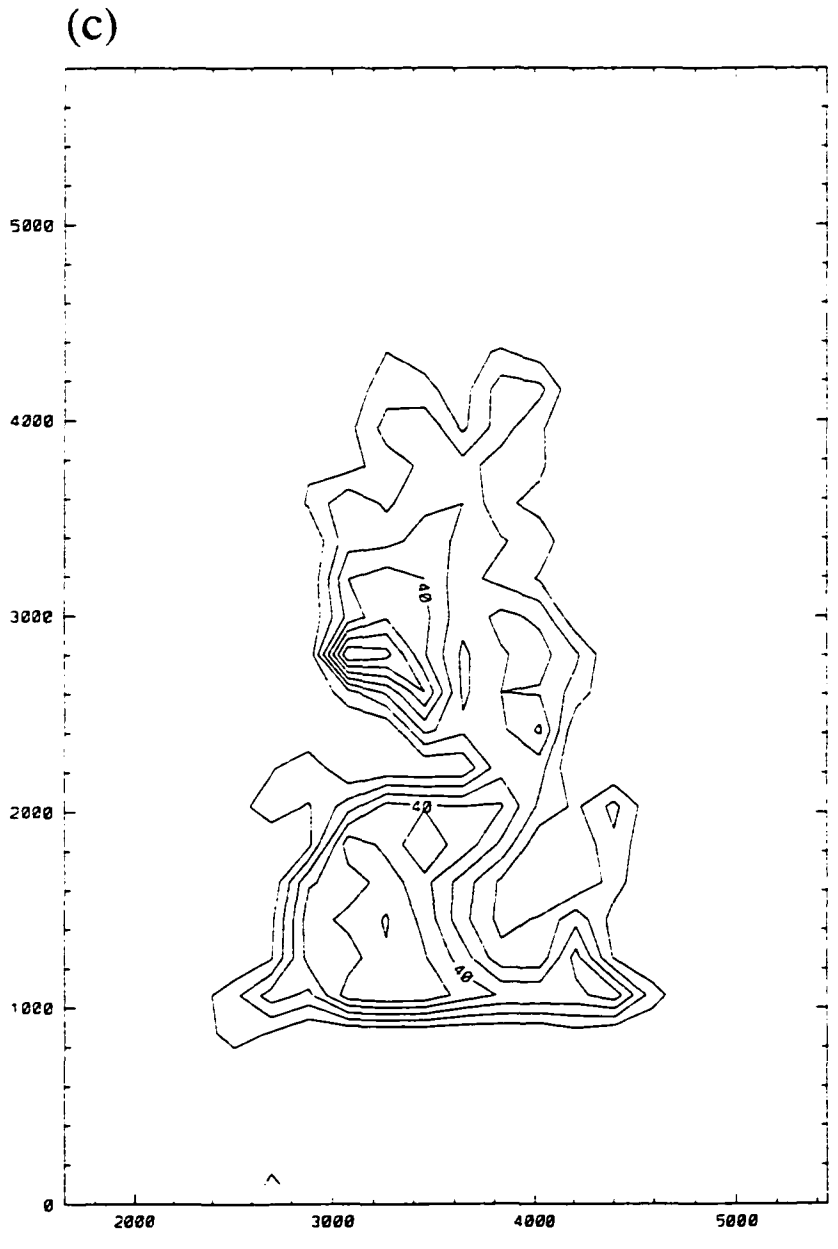


Figure 5.23 (continued).

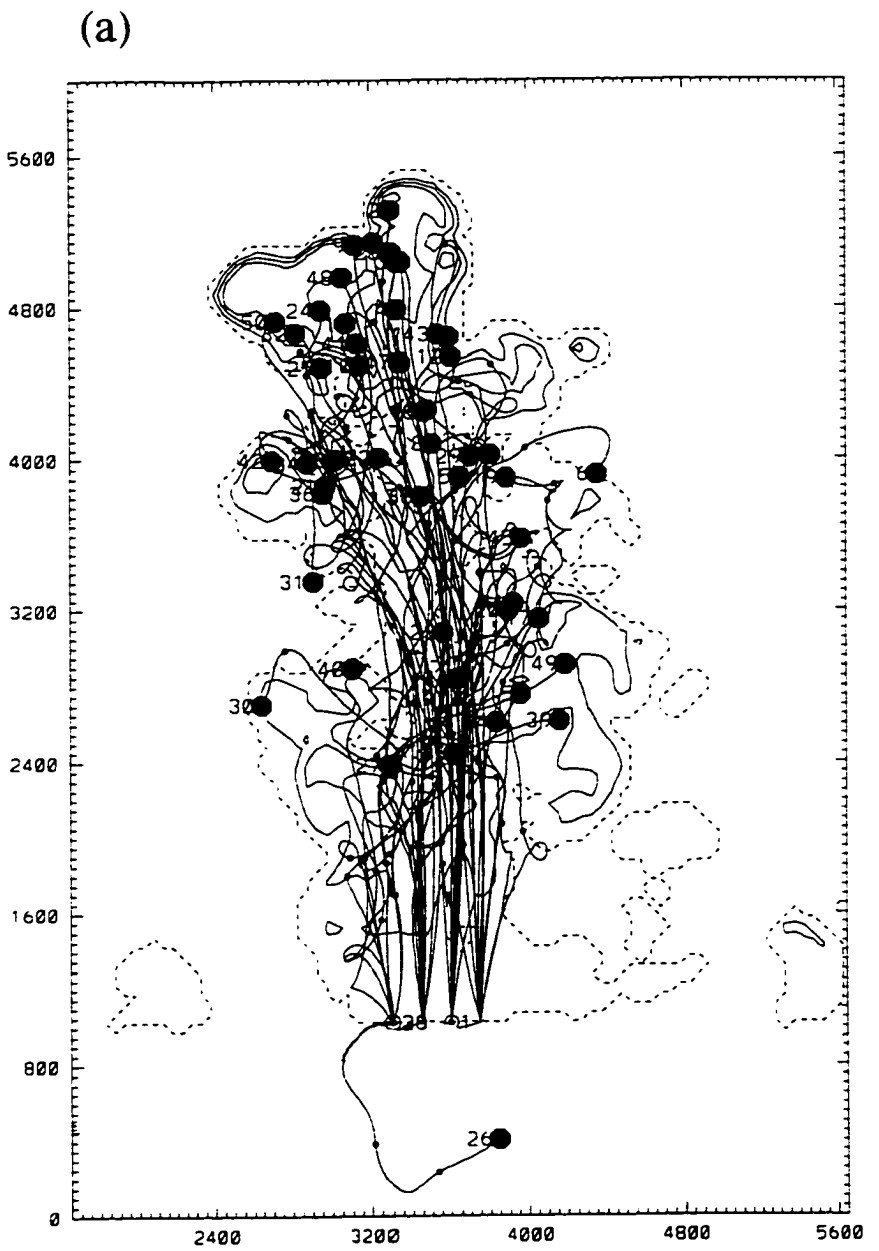


Figure 5.24 As in Fig. 5.18, except at 12 minutes.

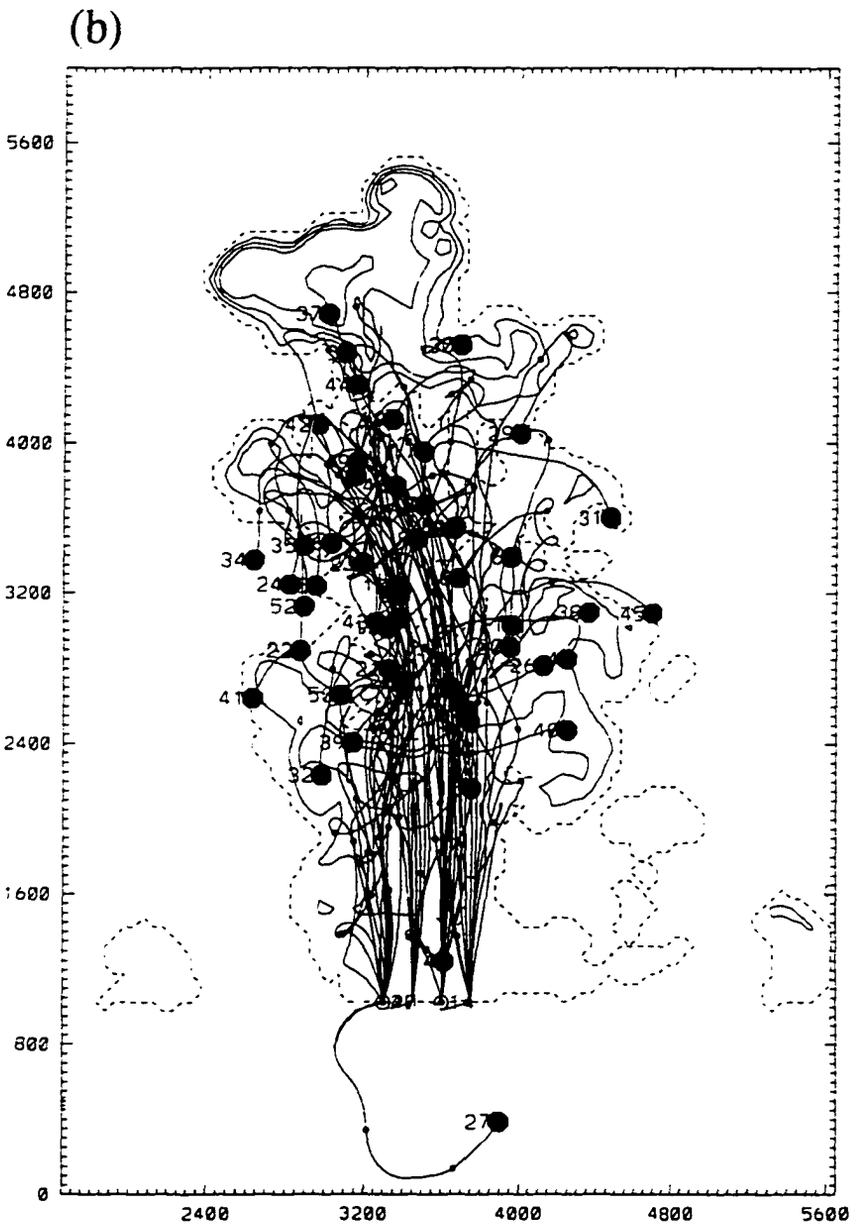


Figure 5.24 (continued).

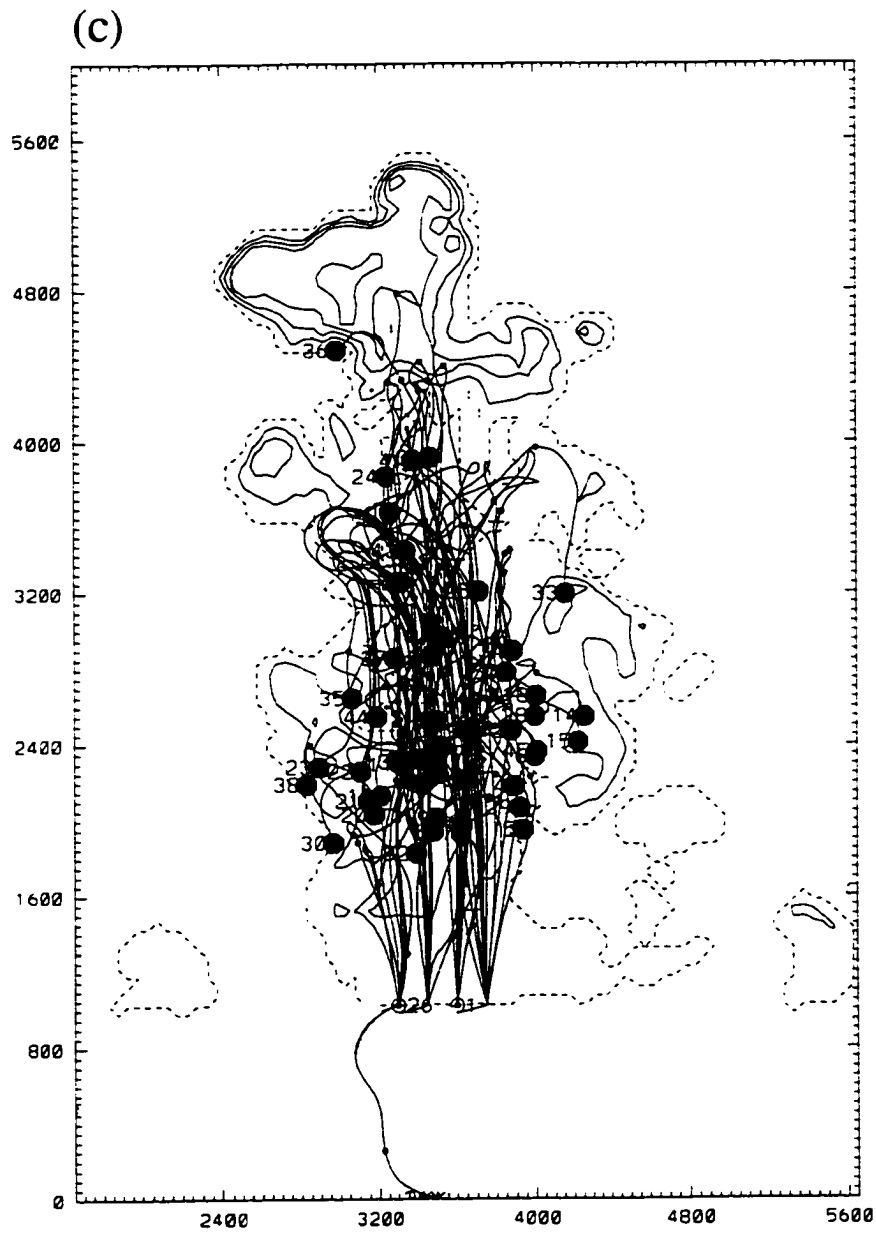


Figure 5.24 (continued).

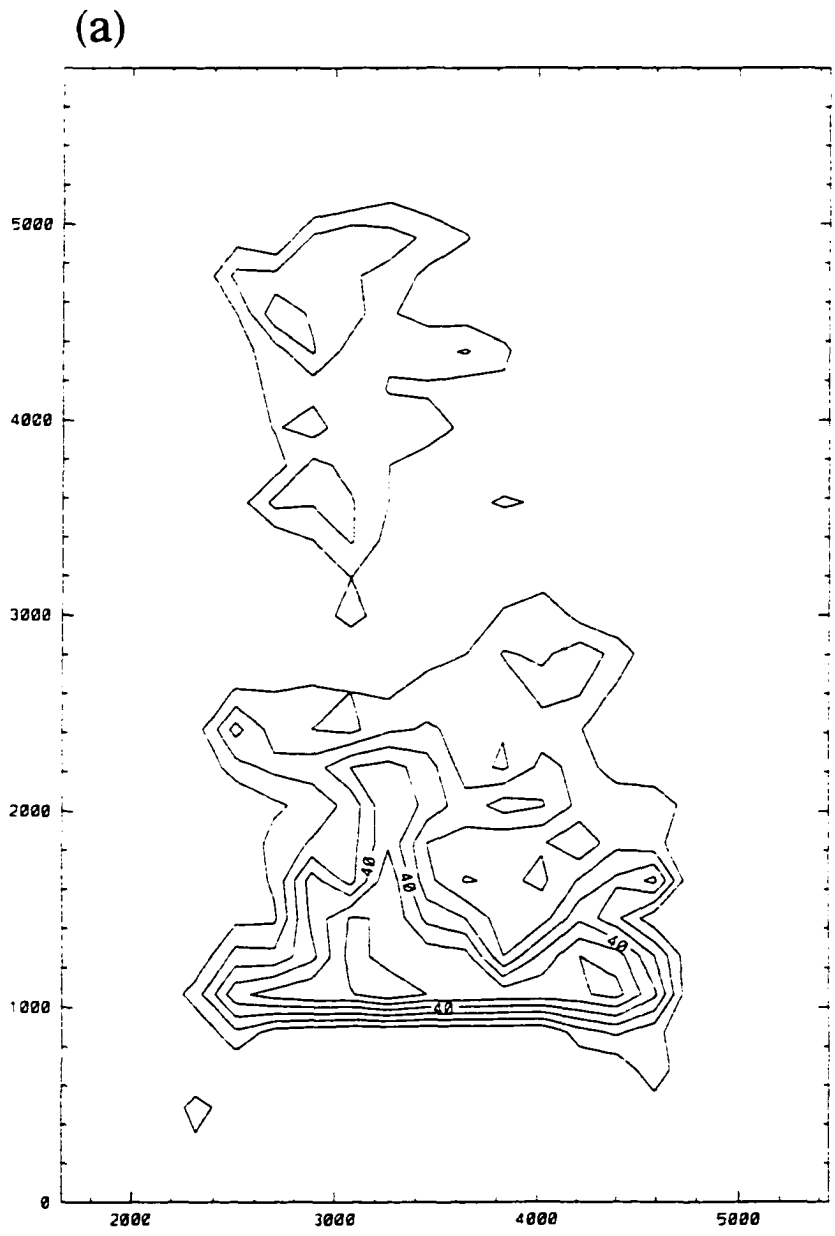


Figure 5.25 As in Fig. 5.19, except at 12 minutes.

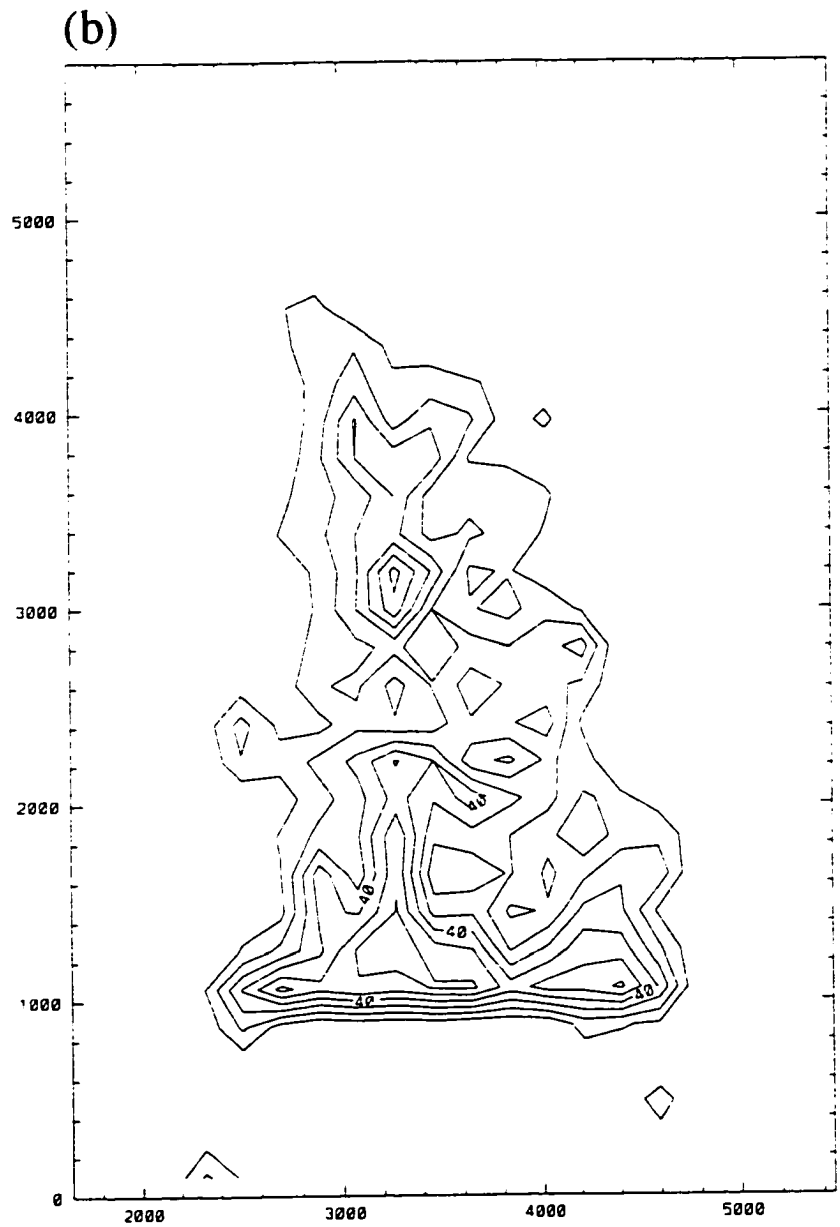


Figure 5.25 (continued).

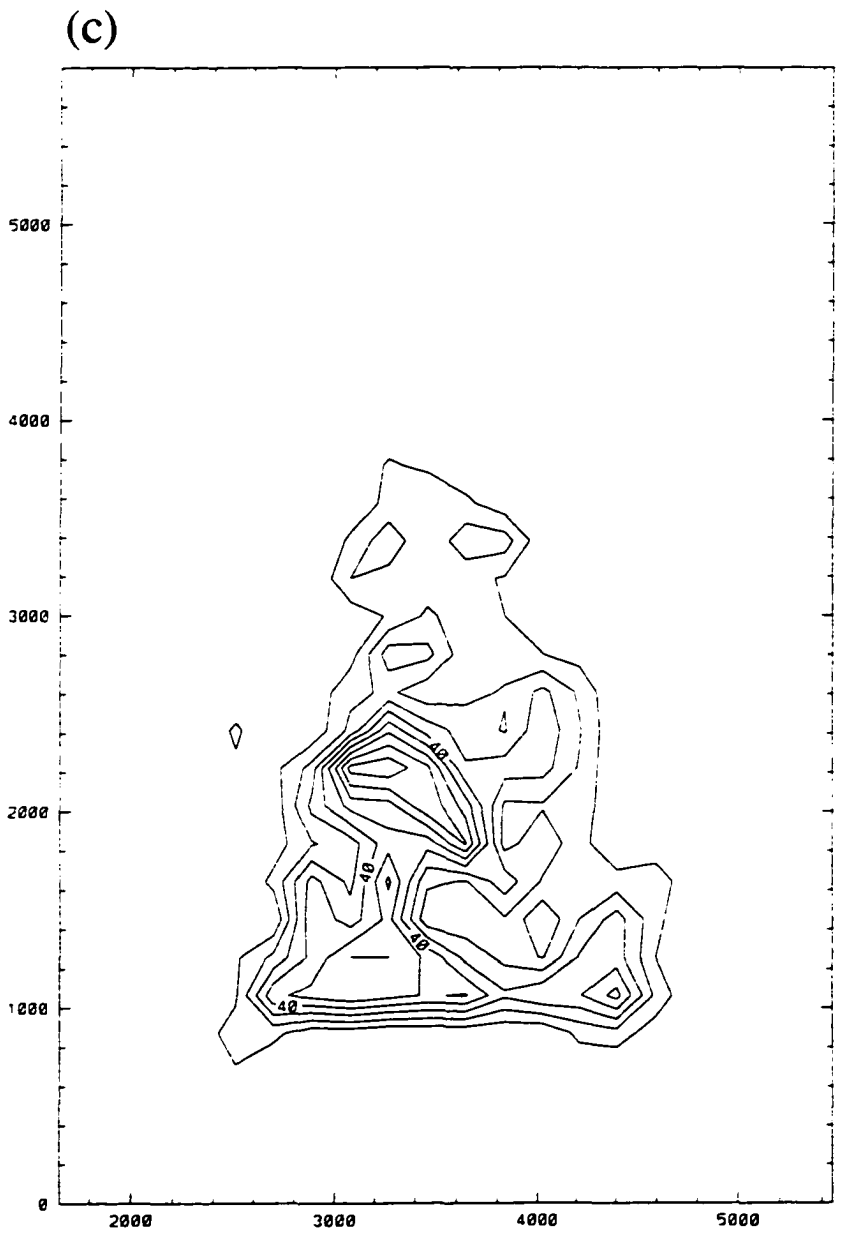


Figure 5.25 (continued).

core of the cloud. The source regions of the highest reflectivity packets (Fig. 5.26) are concentrated at cloud base where the updraft is strongest. The packets contributing the most to the radar echo do change in time, however. Those packets primarily responsible for the 0 dBZ echo at 8 min (Fig. 5.27a) are not the same as those responsible for the 40 dBZ echo at 12 min (Fig. 5.27c), although they were initiated in the same general location (region of maximum updraft) and at nearly the same times. A detailed look at some of the packets contributing to the 0 dBZ echo at 8 min shows that they are advected out of the main updraft core by a large eddy near cloud top at this time; most of the packets caught in this eddy begin their descent into much lower liquid water content regions (Fig. 5.27 a,b) shortly thereafter. The 40 dBZ echo at 12 min is comprised of drops that began as smaller aerosol, were fortunate enough not to have been swept aside by any eddies near cloud top, and are just now beginning their descent.

There is no evidence of drop recycling being important in the modeled cloud. In principle, drops ejected from cloud top can descend with the downdrafts occurring outside the edges of the cloud, and once falling beneath cloud base, be ingested into the cloud again by the combined action of the convergence and updraft beneath cloud base. Kogan (1993) found larger drops were more likely to be recycled in his simulated cloud, through the action of eddies at the cloud sides, well below cloud top. Neither scenario of drop recycling appears important in the present case. Here, the modeled cloud has such a short lifetime that many drops have only begun to reach the cloud top when the simulation is stopped (Fig. 5.27c), preventing their recirculation into the base of the cloud. Those drops pushed outside the main updraft below cloud top by the action of eddies (Figs. 5.27 a,b) are not brought back into the main updraft, nor do they reach the convergence below cloud base by the end of the twelve-minute period. In a separate test where the model was run for 5 min longer than the standard

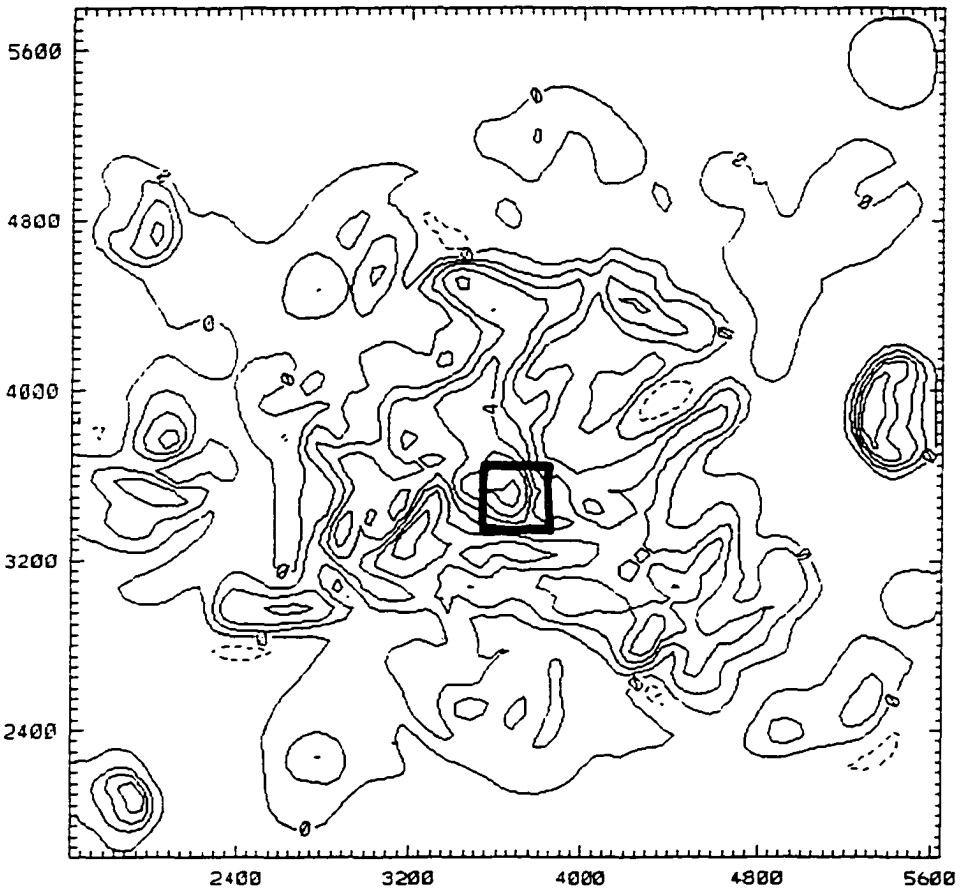


Figure 5.26 Horizontal cross-section of simulated vertical velocity at the height of cloud base, showing source region of packets (within bold square) contributing most to maximum echoes, primary run.

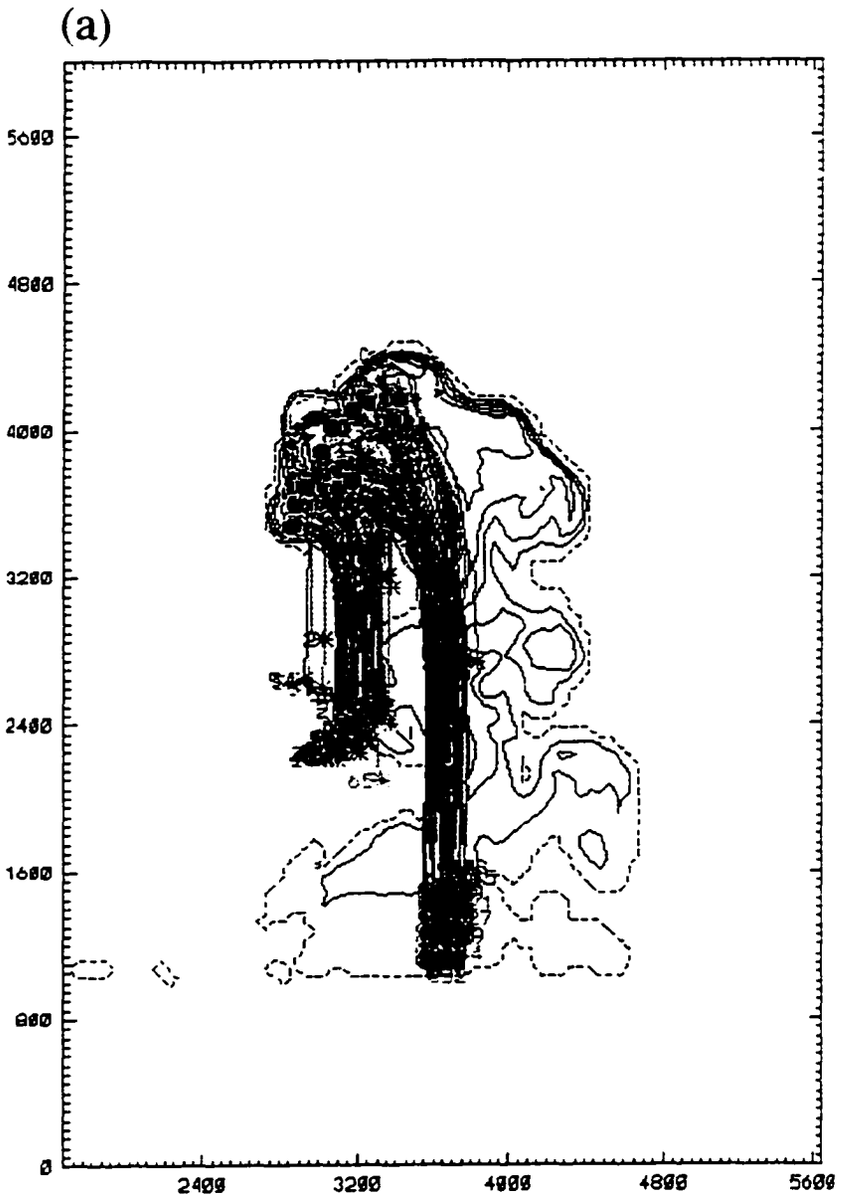


Figure 5.27 Vertical cross-sections of simulated cloud water, with trajectories of packets contributing most to maximim echo overlayed, at (a) 8 minutes, (b) 10 minutes and (c) 12 minutes.

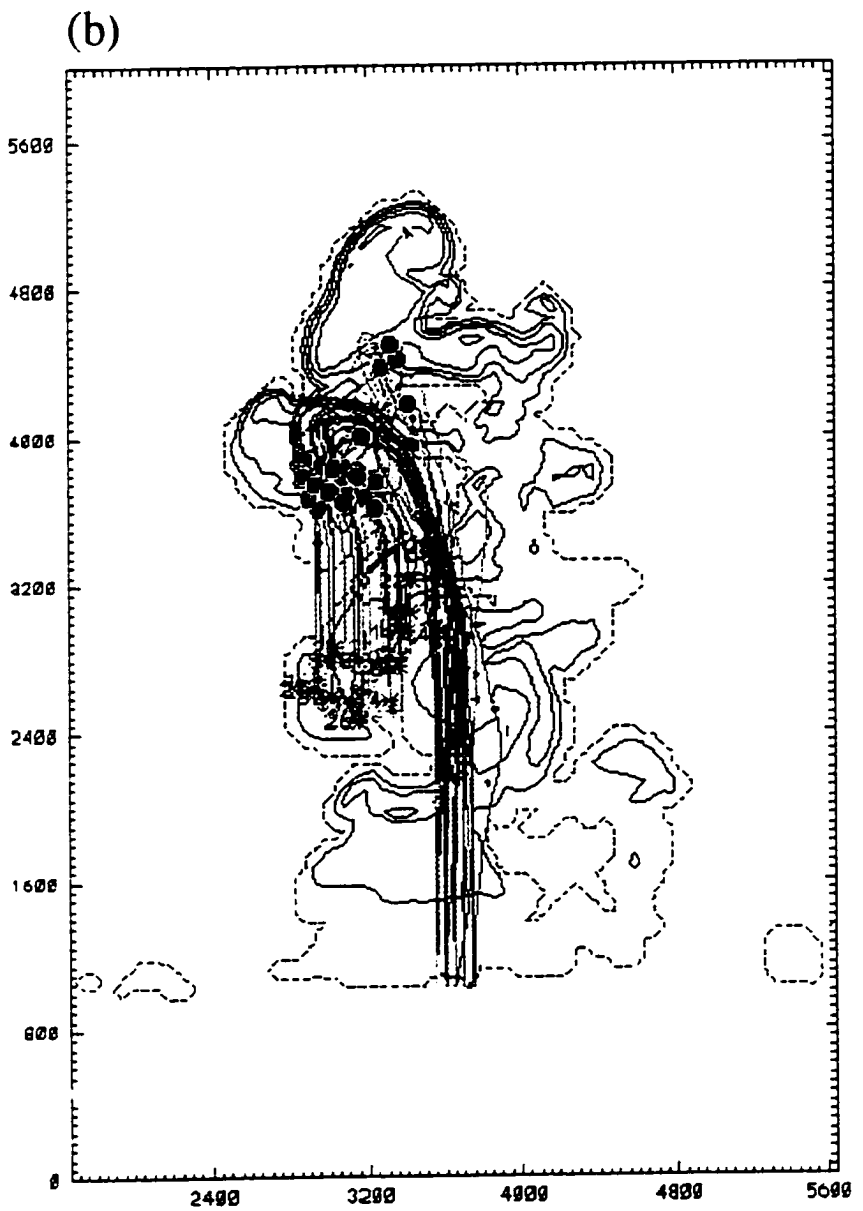


Figure 5.27 (continued).

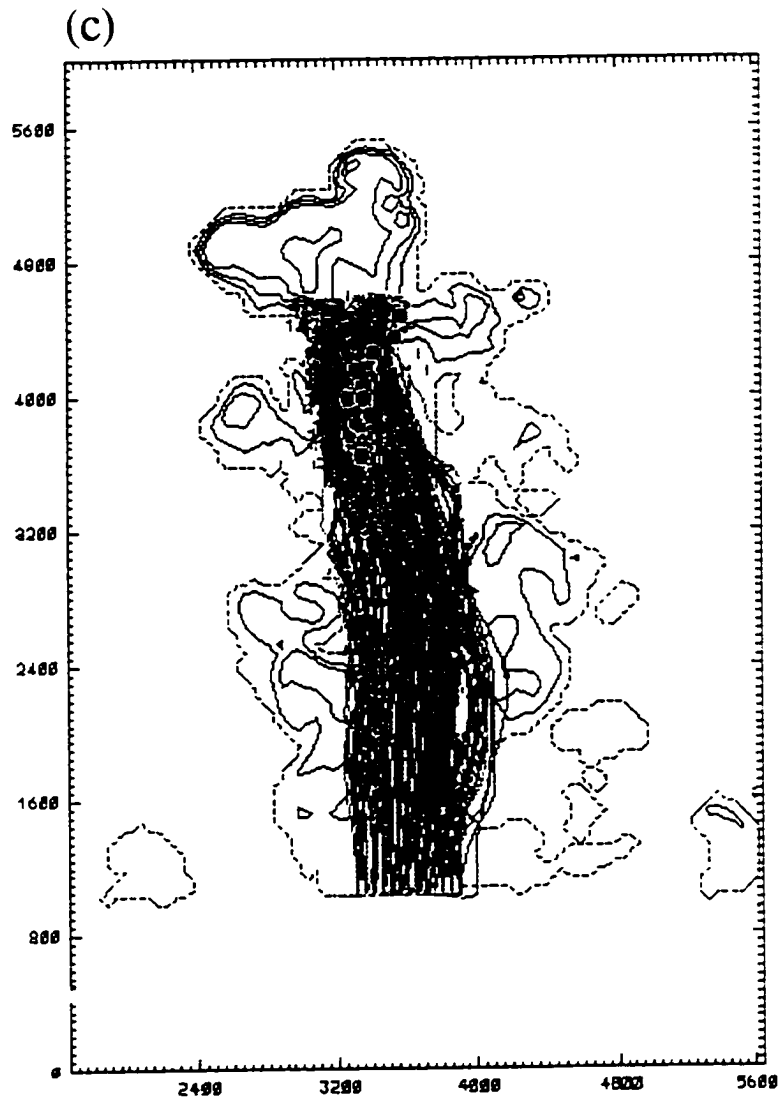


Figure 5.27 (continued).

twelve-minute period, drop recycling still did not occur because the entire cloud was descending (Fig. 5.28), quelling the new updraft that had been forming near cloud base, and preventing any additional ingest of particles.

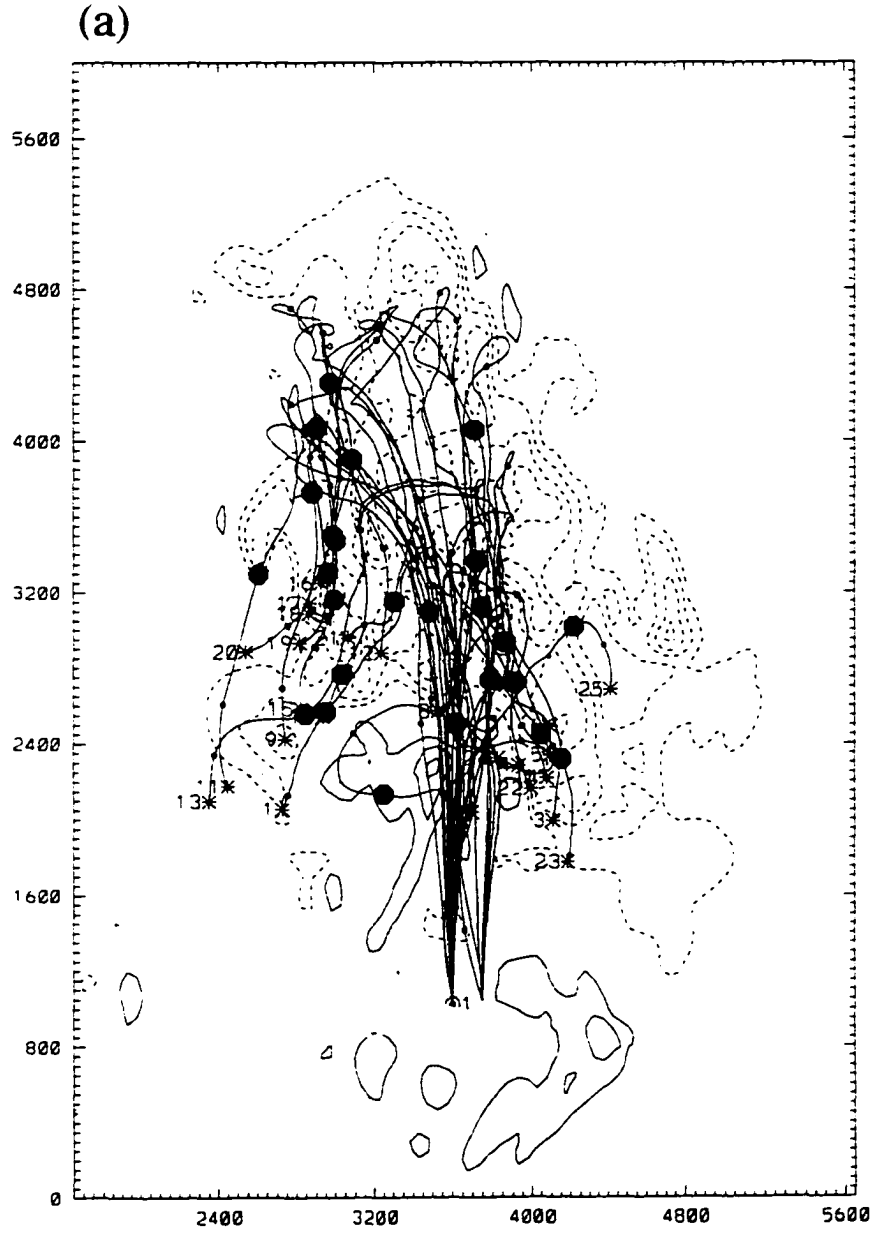


Figure 5.28 Vertical cross-section of simulated vertical velocity with some 25 μm UGA packet trajectories overlayed at (a) 14 minutes and (b) 17 minutes. Contour interval for vertical velocity is 2 m s^{-1}, with negative values indicated by dashed contours (zero contour not plotted).

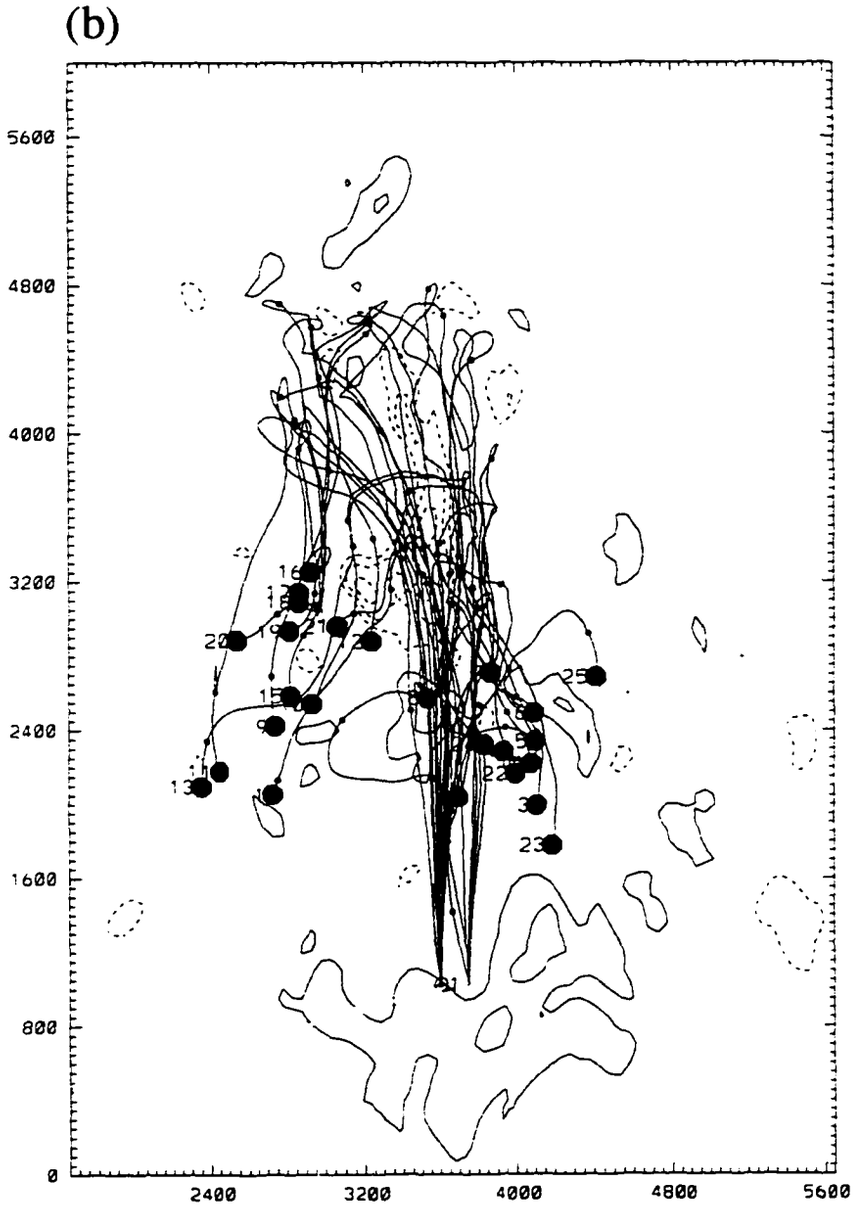


Figure 5.28 (continued).

6. DISCUSSION

A review of the literature has shown UGA are regular constituents of the atmospheric aerosol distribution, but the question concerning their affect upon warm rain formation has remained. The purpose of this study has been to model the growth of UGA within a warm continental cumulus to understand their potential for influencing warm rain. The findings of this study are now discussed to elucidate the importance of UGA for warm rain formation in the modeled cloud, as well as their potential importance in other cumuli.

6.1 General Importance of UGA

Some past studies (Ochs and Semonin 1979, Johnson 1982) have assessed the importance of UGA to warm rain formation by the amount of radar echo they produce. Use of the radar echo is convenient, because these observations are the easiest to acquire, but the radar echo may be misleading in determining the onset of significant precipitation, particularly when considering UGA. As evident in equation (5), the radar echo depends on the sixth power of the drop diameter, but only on the first power of the drop concentration. Thus drops grown on UGA, which can be very large but very few in number, can produce a large radar echo but result in little rainfall. This ambiguity of the radar echo must be kept in mind when judging the importance of UGA to warm rain formation.

Ultragiant aerosol can influence the warm rain process in two ways. First, each UGA can grow into a raindrop simply by collecting cloud water, if enough cloud water is available and the drops formed on the UGA remain in the cloud long enough. Observations have shown that UGA can be present near the ground in amounts of 10^3 to

10^4 m^{-3}, and if they are all ingested into a cloud they can produce this same number of raindrops. Another manner in which UGA may produce even more raindrops is by initiating a "chain-reaction" (Langmuir 1948) of collection and breakup throughout the cloud. Raindrops colliding with other raindrops (or even large cloud droplets) may be expected to produce satellite drops (Brazier-Smith *et al.* 1972, 1973), forming 1-8 fragments per collision, which may in turn grow by collection to breakup size[1]. Or, drops formed on UGA may breakup spontaneously[2], if their radii exceed 4.5 mm. Either of these breakup mechanisms, if active, can increase the number of raindrops formed as a result of UGA.

6.2 Discussion of Model Results

The nature of the cloud in this study has a strong influence upon the potential importance of UGA within it. The cloud is a dynamically-simple turret with a strong updraft and a high liquid water content. The simulated cloud has a strong updraft (up to 20 m s^{-1}) which prevents the largest drops formed on UGA from falling out almost immediately, as they would in a cloud with a weaker updraft. The high liquid water content of the simulated cloud allows the drops formed on UGA to grow very quickly, producing raindrops in concentrations of 150 m^{-3} and a radar echo of 10 dBZ within 8 min. By 12 min, raindrops occupy the upper parts of the cloud in concentrations of nearly 300 m^{-3} and the maximum radar echo has increased to over 40 dBZ.

Although the radar echo produced in the primary run is quite impressive, the amount of rain formed is not excessive. Obviously each UGA does not form a raindrop

---

[1]The sizes of raindrops over which collisional breakup is most frequent is for one drop to be at least 150 to 750 mm in radius, with the other drop having a radius 0.4 to 1.0 times the first drop.
[2]Spontaneous breakup of raindrops is usually attributed to the bag breakup mechanism, in which a depression forms in the base of the large, flattened drop as it falls and eventually leads to a thinning of the droplet in its center (like a bag with the open end pointed downward), before finally breaking into many smaller droplets.

within the twelve-minute period, because then raindrop concentrations would exceed 1000 m^{-3}. Breakup processes are of no help in increasing the production of raindrops by the UGA. Collisional breakup is not allowed in the model, but even if it were, estimates of collision times between such sparse particles exceed thousands of seconds, much longer than the 720 sec the model is run. Spontaneous breakup does not occur by the end of the twelve-minute period, because no drops exceed 4.5 mm radius (or were even close to this size). The few hundred per cubic meter of raindrops produced in the modeled cloud by the UGA, might be judged marginally significant in terms of precipitation efficiency, if the goal of cloud seeding is used as a measure of significance. Cloud seeding experiments attempt to achieve 0.1 to 1.0 ℓ^{-1} (100 to 1000 m^{-3}) graupel particles for high precipitation efficiency[3] (Silverman 1986), although the precipitation efficiency will also depend on the cloud lifetime as well (Cooper 1986). The short lifetime of this cloud and the little cloud water available for collection near the end of its lifetime suggest the raindrop concentration should be higher for a better precipitation efficiency. The short lifetime of the cloud also precludes the importance of drop recirculation (as discussed in Section 5.4), which would otherwise enhance raindrop formation.

6.3 Extension of Model Results to Other Cumuli

The sensitivity tests performed in this study enable some generalizations to be made about the growth of UGA in other clouds. The most important issues concerning the growth of UGA are cloud water content, updraft speed and cloud lifetime and, for longer-lived clouds, the organization of the airflow that may encourage or discourage

[3] Precipitation efficiency is usually defined as the percentage of condensed water in the cloud that falls out of the cloud as rain.

recirculation of hydrometeors. These characteristics of the cloud are of course interrelated, but will be addressed separately to facilitate discussion.

The amount of cloud water available for collection affects the growth rate of UGA the most. The cloud modeled here has an extremely high cloud water content (maximum over 5 g m^{-3}), and as a result the UGA grow very large drops and produce raindrops in concentrations of hundreds per cubic meter. When the cloud water is halved, the drops grown on UGA are much smaller, and the raindrop concentration decreases (barely reaching 100 m^{-3} by the end of the run), because the more numerous, smaller UGA are incapable of growing to raindrop size. These results are consistent with those of Takahashi (1976), who found giant salt particles to be unimportant to warm rain formation in his modeled cloud; his cloud had a cloud water content of only 1 g m^{-3}, which would have decreased the growth rate of the giant salt particles substantially. Thus, in clouds with less cloud water, such as those with higher cloud bases, limited vertical extent, or those growing in drier environments where entrainment may deplete cloud water substantially, UGA appear to be ineffective for warm rain formation, unless other characteristics of the cloud can compensate. For instance, UGA would require lower amounts of cloud water to produce raindrops if drop recirculation is prevalent. The cloud modeled in the present study had little or no drop recirculation, because the lifetime of the cloud was so short. If, however, a longer-lived cloud with less cloud water were capable of recirculating appreciable numbers of drops formed on UGA, then raindrops could form, although the time required to produce them would be longer than that modeled here[4].

Another cloud characteristic that has an affect on the importance of UGA to warm rain formation is the updraft speed. An explicit sensitivity test to updraft speed

[4]Note that the collection model used here could not be used for a longer-lived cloud. The use of the continuous collection model for UGA< 30 μm radius was only justifiable in the present case because the time frame was so short. As the modeling time is extended, the quasi-stochastic growth would need to be used for these UGA, in order not to severely underestimate their growth.

alone is not performed here, because the updraft speed is so closely linked to cloud top ascent rate and liquid water content. However, some influences of updraft speed can be enumerated. A greater updraft speed decreases the time required for the UGA to reach the higher cloud water regions, thereby producing larger drops more quickly. Hence, maximum echo and rain may be produced more quickly with a faster updraft. In addition, the greater the updraft speed, the larger the drops that can be suspended in the cloud. Johnson (1982) found similar results. As he increased the updraft speed of his parcel model, the time to produce a 10 dBZ echo from drops grown on UGA decreased, and the height of the echo in the cloud increased. Because the cloud modeled here has such a strong updraft, it is expected that other cumuli with weaker updrafts would require more time to produce drizzle.

The cloud in this study was simulated without wind shear, but many cumuli occur in highly-sheared environments. Wind shear would force the updraft to tilt with height, likely causing those drops exiting the top of the cloud to fall outside the updraft. It is possible that the end result would be much like the cloud modeled here, for different reasons. The drops formed on UGA in this study were not able to grow much on descent because most of the cloud water had evaporated by that time. In a sheared cloud, little growth might occur during descent as well, because the drops exiting the top would fall outside of the cloud.

6.4 Comparison of Model Results and Observations

A comparison of the model results to the observed cloud is made to test the importance of UGA in this particular cloud. A caveat that must accompany such a comparison is that both the model results and the observations are assumed valid. The continuous collection model itself is straightforward and representative for the present

situation where much fewer but larger drops are collecting much more numerous, smaller droplets. The cloud simulation has been validated as much as possible with the observations, and where there are great uncertainties such as with cloud water content sensitivity tests provide a variety of conditions with which to test the results. These sensitivity tests also aid in interpreting the comparison when observations are lacking, such as the number of UGA ingested by the cloud. The measurement uncertainties in the radar echo have been thoroughly studied and documented, and are believed accurate, although ambiguities in the source of the radar echo may cause larger errors. Much less confidence can be had in the aircraft measurements, where limited sampling makes the measurement uncertainties unknown, so they are only used loosely for comparison purposes.

The development of the modeled maximum echo from drops formed on UGA is different from that observed on radar. The observed X-band radar echo development between 0 and 10 dBZ (at heights up to 5 km within the cloud) is presumably (see below) due to drops formed by coalescence, and it is this radar echo evolution that is compared with the growth of the UGA. The UGA in the primary run produce a -1 dBZ echo (Fig. 6.1a) after 7 min at approximately 3.8 km height (Fig. 6.1b); the onset of this echo compares well with the appearance of the 0 dBZ echo on radar (recall the noise in the observed and modeled reflectivity each has been estimated at 2-3 dB), except that the modeled echo is 200 m lower in the cloud. One minute later, however, the modeled maximum echo jumps to over 9 dBZ, and unlike the radar observations, quickly grows to over 40 dBZ by 12 min. The height of the modeled maximum echo is always beneath 4.5 km height. Numerous experiments in which the radii or concentration of the collected cloud droplets is changed did little to decrease the modeled echoes.

A logical possibility is that fewer UGA are ingested by the real cloud than that used in the modeled cloud. The very high UGA number concentration used in the

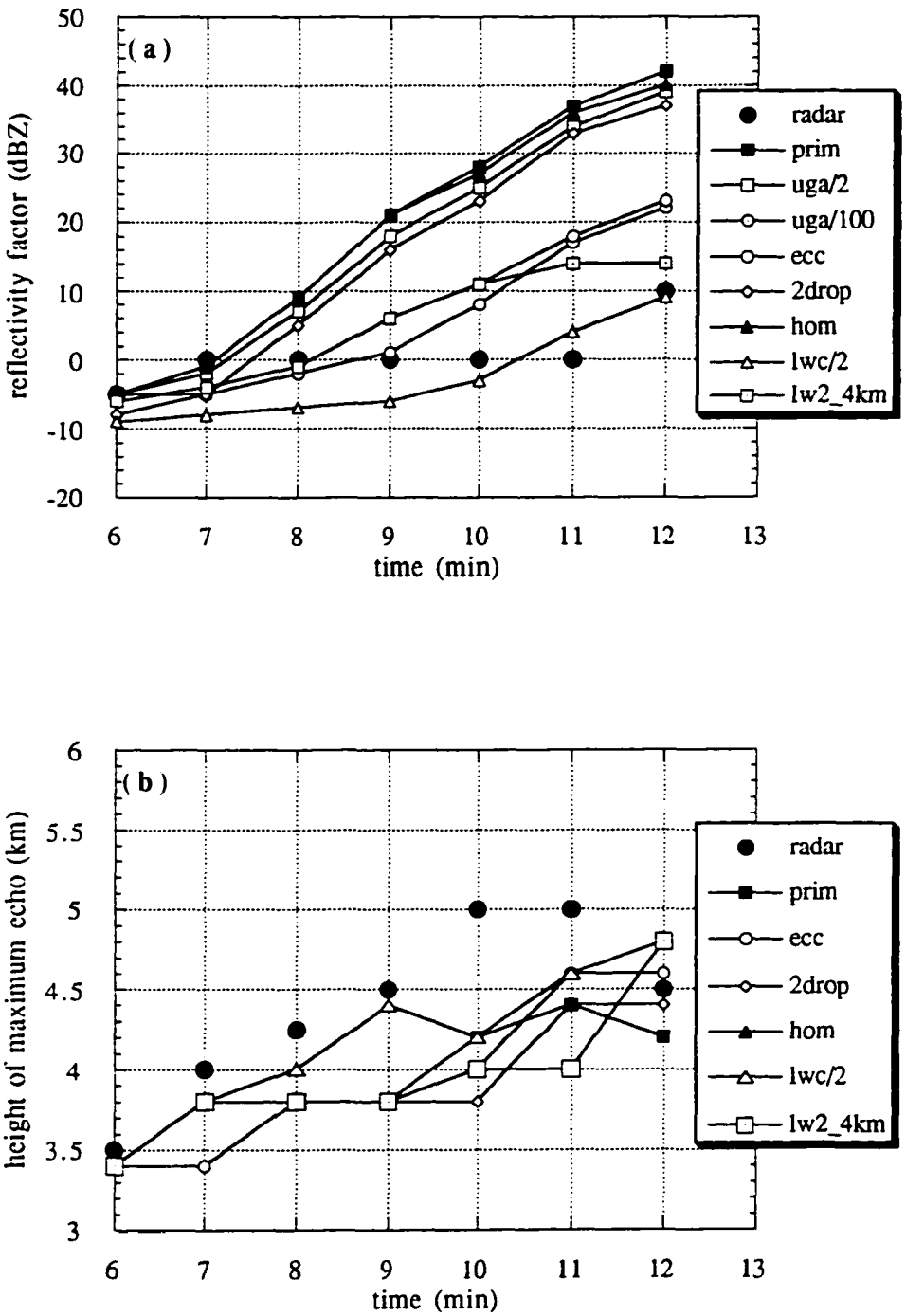


Figure 6.1 (a) Comparison of maximum echo, from radar and that calculated from cloud droplets and drops grown on UGA, for all experiments. (b) Height of maximum echo plotted in (a).

primary run has been measured at the ground by previous investigators, but the UGA concentrations are known to decrease with altitude. Reducing the number of UGA used in the model simply decreases the magnitude of the maximum echo, however, and does not affect its rate of growth (the slope of the curve in Fig. 6.1), as shown by the "uga/2" and "uga/100" tests. The number of UGA could be decreased further, to the point at which the modeled and observed echoes are equivalent by the end of the twelve-minute period, but the time of formation of the 0 dBZ echo would be substantially delayed. Changing the concentrations within different parts of the spectrum of UGA, as discussed in Section 5.1.4, also does not reproduce the observed echo development (Fig. 6.2). Those sizes of UGA necessary to create the 0 dBZ echo by 7 min (55-66 μm) are those responsible for the excessive echo (that is too low in the cloud) by 12 min, and those sizes (15-25 μm, or 85-95 μm) which could be used in lower concentrations to match the observed maximum echo at the end of the 12 min (albeit too low in the cloud) are incapable of producing a 0 dBZ echo much earlier. Using only 35-45 μm UGA produces results similar to the primary run, because they dominate at the later times in that run.

Another possibility - that the simulated cloud water is much higher than that which occurred in reality - has been tested and also fails to make the modeled echo match the observed echo development. As discussed earlier, the simulated cloud water does seem high, and so might be biasing the model results. When the cloud water is halved ('lwc/2', in Fig. 6.1), the final reflectivity agrees with that observed, but a delay in the appearance of the 0 dBZ echo again occurs, as was the case when the concentrations of UGA were greatly reduced. When the simulated cloud water is halved above 4 km (which maintains the time of formation of the 0 dBZ echo), the modeled echo ('lw2_4km", in Fig. 6.1) is still greater than that observed and forms much higher in the cloud.

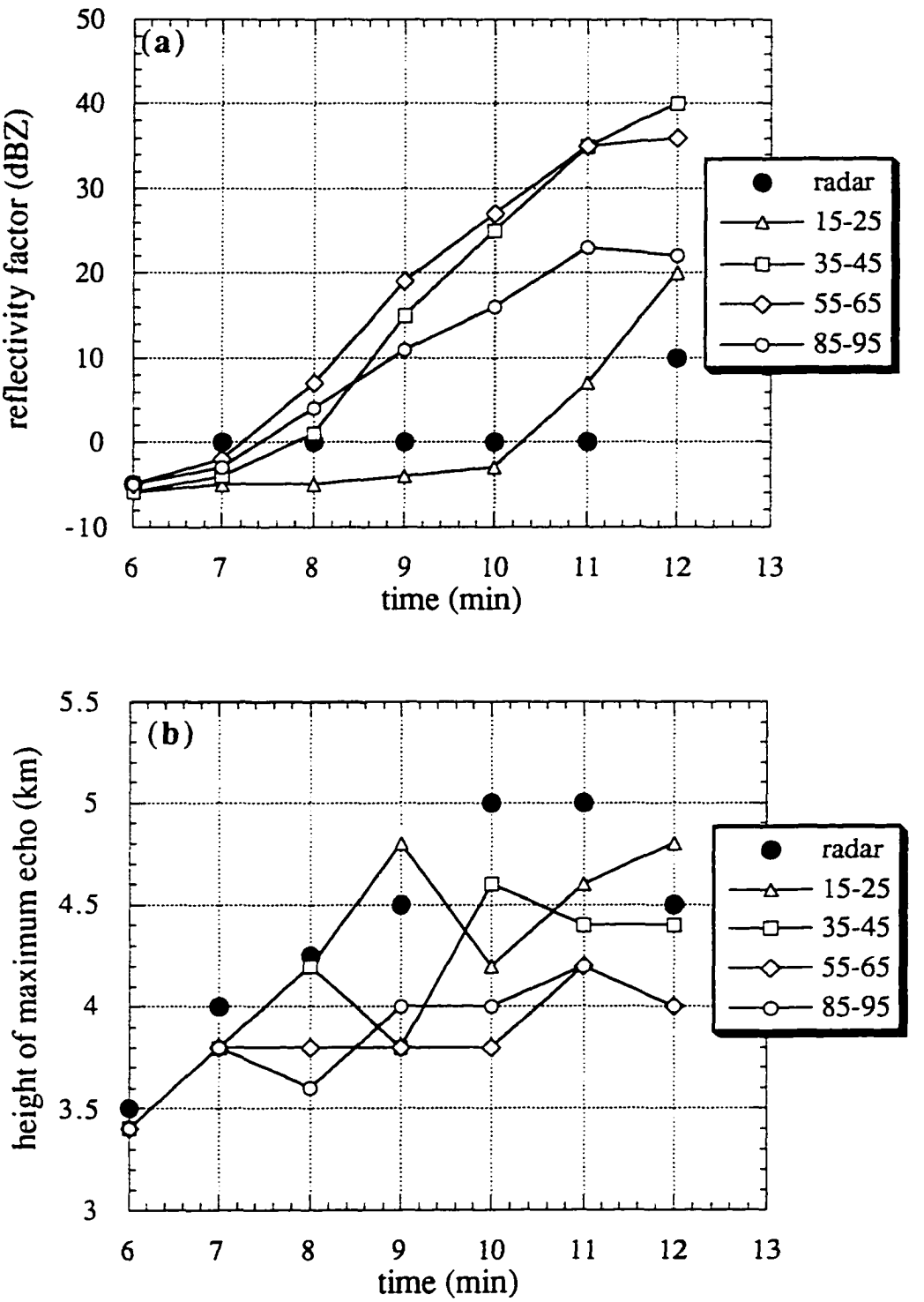


Figure 6.2 Maximum reflectivity factor calculated from cloud water and drops formed on specific size ranges of UGA. Maximum observed radar echo also plotted. (b) Height of maximum echo plotted in (a).

The argument against UGA as the initiators of coalescence in this cloud is weakened, however, by the possibility that the 0 dBZ echo on X-band is not purely from Rayleigh scattering of water droplets. As discussed earlier, if Bragg or some other type of scattering is contributing to the X-band echo, then the Rayleigh echo is less than the 0 dBZ value used in this analysis. If this is true, then the growth of the UGA would possibly agree with the observed radar echo if (i) the simulated cloud water is overestimated by a factor of two, or (ii) the number concentration of UGA is very low. These latter two possibilities have not been ruled out thus far.

Despite the uncertainty in the origin of the observed 0 dBZ echo, and thus the uncertainty of the discrepancy between the modeled and observed echo development, an analysis of the modeled and observed rain provides evidence against the importance of UGA in this cloud. Raindrops recorded by the 2D-P probe[5] during the two penetrations of the cloud, during the time of the 0 dBZ echo, indicate maximum concentrations of 100 to 150 m^{-3}. At the times corresponding to these aircraft observations, the modeled raindrop concentration is far less, never exceeding 20 m^{-3} at the height of the first penetration and 50 m^{-3} at the height of the second penetration. The modeled raindrop concentration (when the maximum number of UGA is used) is only as high as the observed concentrations at much higher altitudes within the cloud at this time (refer back to Fig. 5.13). The model has shown, however, that when the maximum number of UGA are present, the radar echo (in dBZ) would be four times greater than that observed. Because the observed radar echo is less, the size of the hydrometeors must be much smaller than those modeled with the UGA. Thus, the source of the raindrops at the early times and low heights observed in the cloud does not appear to be UGA.

[5]The 2D-P probe is an optical array probe, with a two-dimensional array of diodes that are illuminated by lasers. As the particles travel through the instrument, they shadow the diodes and the particles are sized by the number of diodes shadowed. The particles measured by this instrument have diameters between 200 and 6400 μm, and the sample volume is approximately 168 ℓ per 100 m of flight.

If UGA did not produce the observed raindrop concentrations or radar echo, then some other mechanism must be responsible. The design of this study has been tailored to studying the growth of UGA, however, and does not lend itself to investigating other mechanisms such as quasi-stochastic collection. (The present "packet" framework is useful when considering continuous collection because all the drops within the packet grow at the same rate; for quasi-stochastic collection the packets would have to be constantly breaking up into sub-packets as droplets grew at different rates, soon rendering the number of packets and trajectories unmanageable computationally). Other hypotheses for creating large drops capable of initiating coalescence, such as entrainment/mixing theories or stochastic condensation (see review article by Beard and Ochs 1993), also require a completely different model framework than that used here. A fully three-dimensional cloud model including explicit calculations of condensation and quasi-stochastic collection would be a more direct means of investigating these other mechanisms.

6.5 Future Work

Future work should include the testing of additional cases. Some cases should be continental cumuli, in order to have a better sample for the conclusions reached in the present study. Cumuli of a maritime nature, i.e., with much lower drop concentrations, were observed on several days during the SCMS, and should be examined for different responses to UGA. In addition, several clouds were observed during the SCMS to produce 10-40 dBZ radar echoes, when cloud top height was limited by an inversion to about 3 km; drop recirculation could influence the importance of UGA in these cases. And finally, investigating some cumuli growing in sheared environments would be

useful to test the speculations on the effect of shear on the growth of the UGA discussed earlier.

A top priority in future work also will be to determine the Rayleigh component of the early echo on the X-band radar. The unfortunate uncertainty in the radar reflectivity, namely, the type of scattering responsible for the 0 dBZ echo on the X-band radar, has left the conclusions about the importance of UGA to the 22 July cloud somewhat tentative. Determining the contribution to the 0 dBZ echo by Rayleigh scattering of water droplets is paramount to determining the importance of UGA in this cloud. If the 0 dBZ echo is in fact due to Rayleigh scattering of water droplets, then the ultragiant nucleus hypothesis is disproved in this case, and other mechanisms for producing warm rain will need to be considered.

In the future, observations could be made that would be more useful to testing the ultragiant nucleus hypothesis. For instance, testing the existence of UGA within the cloud inflow and sampling the cloud water content in the upper as well as lower parts of the cloud would provide the most crucial information for testing the ultragiant nucleus hypothesis. Both of these measurements are not only difficult to take, but also are troubled by instrument inadequacies. However, even rough estimates would provide more definite bounds on these quantities for the calculations, which are presently only loosely-bounded.

REFERENCES

Baker, B. A., 1992: Turbulent entrainment and mixing in clouds: A new observational approach. *J. Atmos. Sci.*, **49**,387-404.

Beard, K. V., 1976: Terminal velocity and shape of cloud and precipitation drops aloft. *J. Atmos. Sci.*, **33**, 851-864.

_____, and H. T. Ochs III, 1984: Collection and coalescence efficiencies for accretion. *J. Geophys. Res.*, **89**, 7165-7169.

_____, and _____, 1993: Warm-rain initiation: an overview of microphysical mechanisms. *J. Appl. Meteor.*, **32**, 608-625.

Brazier-Smith, P. R., S. G. Jennings and J. Latham, 1972: The interaction of falling water drops: coalescence. *Proc. Roy. Soc. London*, **A326**, 393-408.

_____, _____ and _____, 1973: Raindrop interactions and rainfall rates within clouds. *Quart. J. Roy. Meteor. Soc.*, **99**, 260-272.

Carpenter, R. L. Jr., 1994: *Entrainment and Detrainment in Numerically Simulated Cumulus Congestus Clouds*. Ph.D. dissertation, School of Meteorology, Univ. of Oklahoma, 256 pp.

Caylor, I. J. and A. J. Illingworth, 1987: Radar observations and modelling of warm rain initiation. *Quart. J. Roy. Meteor. Soc.*, **113**, 1171-1191.

_____, R. T. Bruintjes and G. K. Mather, 1997: Calculations pertaining to hygroscopic seeding with flares. *J. Appl. Meteor.*, **36**, 1449-1469.

Clark, T. L. and W. R. Farley, 1984: Severe downslope windstorm calculations in two and three spatial dimensions using anelastic grid nesting: A possible mechanism for gustiness. *J. Atmos. Sci.*, **41**, 329-350.

Cooper, W. A., 1986: "Ice initiation in natural clouds", from Precipitation Enhancement- A Scientfic Challenge. R. Braham Jr., (ed.), *Meteorological Monographs*, **21**, American Meteorological Society, Boston, MA, 29-32.

Gillespie, D. T., 1975: Three models for the coalescence growth of cloud drops. *J. Atmos. Sci.*, **32**, 600-607.

Hallett, J., R. I. Sax, D. Lamb and A. S. R. Murty, 1978: Aircraft measurements of ice in Florida cumuli. *Quart. J. Roy. Meteor. Soc.*, **104**, 631-651.

Houze, R. A., 1993: *Cloud Dynamics*. Academic Press, San Diego, 573 pp.

Illingworth, A. J., 1988: The formation of rain in convective clouds. *Nature*, **336**, 754-756.

Jaenicke, R. and C. Junge, 1967: Studien zur oberen grensgrosse des naturlichen aerosoles. *Beitr. Phys. Atmos.* **40**, 129-143.

Johnson, D. B., 1976: Ultragiant urban aerosol particles. *Science*, **194**, 941-942.

_____, 1982: The role of giant and ultragiant aeorsol particles in warm rain initiation. *J. Atmos. Sci.*, **39**, 448-460.

Junge, C. E., 1972: Our knowledge of the physico-chemistry of aerosols in the undisturbed marine environment. *J. Geophys. Res.*, **77**, 5183-5200.

Klett, J. D., and M. H. Davis, 1973: Theoretical collision efficiencies of cloud droplets at small Reynolds numbers. *J. Atmos. Sci.*, **30**, 107-117.

Klemp, J. B., and R. B. Wilhelmson, 1978: The simulation of three-dimensional convective storm dynamics. *J. Atmos. Sci.*, **35**, 1070-1096.

Knight, C. A., 1990: Lagrangian modeling of the ice process: A first echo case. *J. Appl. Meteor.*, **29** 418-428.

_____ and L. J. Miller, 1993b: First radar echoes from cumulus clouds. *Bull. Amer. Meteor. Soc.*, **74**, 179-188.

Kogan, Y. L., 1993: Drop size separation in numerically simulated convective clouds and its effect on warm rain formation. *J. Atmos. Sci.*, **50**, 1238-1253.

Langmuir, I., 1948: The production of rain by chain reaction in cumulus clouds at temperatures above freezing. *J. Meteor.*, **5**, 175-192.

Ludlam, F. H., 1951: The production of showers by the coalescence of cloud droplets. *Quart. J. Roy. Meteor. Soc.*, **77**, 402-417.

Mason, B. J., 1971: *The Physics of Clouds*. Oxford University Press, 671 pp.

Melzak, A. Z. and W. Hitschfeld, 1953: A mathematical treatment of random coalescence. McGill University, Stormy Weather Group Rep. MW-11, 28 pp.

Nelson, R. T., and N. R. Gokhale, 1968: Concentrations of giant particles below cloud bases. *Preprints First Nat. conf. Weather Modification*, Albany, Amer. Meteor. Soc., 89-98.

Noll, K. E. and M. J. Pilat, 1971: Size distribution of atmospheric giant particles. *Atmospheric Environment*, **5**, 527-540.

Ochs, H. T. III and R. G. Semonin, 1979: Sensitivity of a cloud microphysical model to an urban environment. *J. Appl. Meteor.*, **18**, 1118-1129.

Okita, T., 1955: Interaction between atmospheric aerosols and raindrops. *J. Meteor. Soc. Japan*, **33**, 220-226.

Paluch, I. R. and C. A. Knight, 1984: Mixing and the evolution of cloud droplet size spectra in a vigorous continental cumulus. *J. Atmos. Sci.*, **41**, 1801-1815.

_____, and _____, 1986: Does mixing promote cloud droplet growth? *J. Atmos. Sci.*, **43**, 1994-1998.

Pruppacher, H. R. and J. D. Klett, 1978: *Microphysics of clouds and precipitation.* D. Reidel, 714 pp.

Reitan, C. H., and R. R. Braham, 1954: Observations of salt nuclei over the midwestern United States. *J. Meteor.*, **11**, 503-506.

Rogers, R. R., and M. K. Yau, 1989: *A Short Course in Cloud Physics.* Pergamon Press, 3rd edition, Oxford, 290 pp.

Rosinski, J., 1966: Solid water-insoluble particles in hailstones and their geophysical significance. *J. Appl. Meteor.*, **5**, 481-491.

_____, 1967b: Insoluble particles in hail and rain. *J. Appl. Meteor.*, **6**, 1066-1074.

_____, and T. C. Kerrigan, 1969: The role of aerosol particles in the formation of raindrops and hailstones in severe thunderstorms. *J. Atmos. Sci.*, **26**, 695-726. (Corrigendum: *J. Atmos. Sci.*, **27**, 178-179).

Sánchez, O. D., D. J. Raymond, L. Libersky and A. . Petschek, 1989: The development of thermals from rest. *J. Atmos. Sci.*, **46**, 2280-2292.

Sax, R. I. and V. W. Keller, 1980: Water-ice and water-updraft relationships near -10°C within populations of Florida cumuli. *J. Appl. Meteor.*, **19**, 505-514.

Silverman, B. A., 1986: "Static mode seeding of summer cumuli- a review", from Precipitation Enhancement- A Scientfic Challenge. R. Braham Jr., (ed.), *Meteorological Monographs*, **21**, American Meteorological Society, Boston, MA, 7-24.

Soong, S., and Y. Ogura, 1973: A comparison between axisymmetric and slab-symmetric cumulus cloud models. *J. Atmos. Sci.*, **30**, 879-893.

Straka, J. M., and J. R. Anderson, 1993: Numerical simulations of microburst-producing storms: Some results from storms observed during COHMEX. *J. Atmos. Sci.*, **50**, 1329-1348.

Takahashi, T., 1976: Warm rain, giant nuclei and chemical balance- a numerical model. *J. Atmos. Sci.*, **33**, 269-286.

Telford, J. W., 1955: A new aspect of coalescence theory. *J. Meteor.*, **12**, 436-444.

Woodcock, A. H., 1952: Atmospheric salt particles and raindrops. *J. Meteor.*, **9**, 200-212.

_____, 1953: Salt nuclei in marine air as a function of altitude and wind force. *J. Meteor.*, **10**, 362-371.

_____, R. A. Duce and J. L. Moyers, 1971: Salt particles and raindrops in Hawaii. *J. Atmos. Sci.*, **28**, 1252-1257.

Young, K. C., 1975: The evolution of drop spectra due to condensation, coalescence and breakup. *J. Atmos. Sci.*, **32**, 965-973.

Appendix A. Cloud Model Equations

The model structure has been derived to a large extent from Klemp and Wilhelmson (1978) (hereafter, KW78), and the reader is directed there for additional information. Prognostic equations for the u, v and w velocity components, perturbation pressure (p'), potential temperature (θ'), water vapor (q_v') and cloud water (q_c') mixing ratios and subgrid-scale kinetic energy (e) are solved. (Actually, the eddy mixing coefficient, K_m, is predicted and the subgrid-scale kinetic energy is calculated from it). A hydrostatically-balanced base state

$$\frac{d\bar{p}}{dz} = -\bar{\rho} g, \tag{A1}$$

is subtracted from the vertical momentum equation to improve accuracy. (An overbar denotes the horizontally-uniform base state variables, ρ is the air density and g is the acceleration due to gravity). The momentum equations are

$$\frac{\partial u_i}{\partial t} = Adv_{u_i} - \frac{1}{\rho}\frac{\partial p'}{\partial x_i} + g\delta_{i3}\left[\frac{\theta'}{\bar{\theta}} + 0.608q'_v - q_c - \frac{p'}{\gamma \bar{p}}\right] + Turb_{u_i} + Filt_{u_i} \tag{A2}$$

where i= 1, 2, 3, primed variables represent variations from the base state, γ is the ratio of specific heats C_p/C_v, *Adv* denotes the advection terms, *Turb* denotes the turbulent mixing terms and *Filt* represents the filtering terms. Mass continuity is written in terms of the perturbation pressure as

$$\frac{\partial p'}{\partial t} = -c_s^2 \frac{\partial \bar{\rho} u_j}{\partial x_j} \tag{A3}$$

where c_s is a fictitious speed of sound, set to 150 m s^{-1} for this study. The use of a reduced speed of sound, called super-compressibility (Droegemeier and Davies-Jones 1987), allows those terms responsible for sound waves to be solved on a larger time step. In addition, the time-splitting procedure of KW78 allows terms not contributing to sound waves to be solved on an even larger timestep.

The prognostic equation for all scalars other than pressure is

$$\frac{\partial \phi}{\partial t} = Adv_\phi + Mphys_\phi + Turb_\phi + Filt_\phi \tag{A4}$$

where the parameterized microphysical terms are given by

$$Mphys_\theta = -\frac{L\bar{\theta}}{C_p \bar{T}} \frac{dq_{vs}}{dt} \tag{A5a}$$

$$Mphys_{q_v} = \frac{dq_{vs}}{dt} \tag{A5b}$$

$$Mphys_{q_c} = -\frac{dq_{vs}}{dt} \tag{A5c}$$

(here L is the latent heat of condensation, C_p is the specific heat at constant pressure, T is temperature and q_{vs} is the saturation water vapor mixing ratio).

The subgrid parameterization is the 1-1/2 order closure scheme of KW78. Turbulent mixing for scalars is represented as

$$Turb_\phi = -\frac{\partial}{\partial x_j}\left\langle u_j'' \phi_j'' \right\rangle = \frac{\partial}{\partial x_j}\left(K_H \frac{\partial \phi}{\partial x_j} \right) \tag{A6}$$

where angle brackets denote Reynolds averages, double primes represent subgrid-scale quantities and K_H is the eddy mixing coefficient for scalars. Turbulent mixing for momentum is represented as

$$Turb_{u_i} = -\frac{\partial}{\partial x_j}\left\langle u_i'' u_j'' \right\rangle \approx \frac{\partial}{\partial x_j}\left[K_M\left(\frac{\partial u_i}{\partial x_j} + \frac{\partial u_j}{\partial x_i} \right) + \frac{2}{3}\delta_{ij} e \right] \tag{A7}$$

where K_m is the eddy mixing coefficient for momentum and e is the subgrid-scale kinetic energy, related to K_m by

$$K_M = C_K e^{1/2} (\Delta x \Delta y \Delta z)^{1/3} \tag{A8}$$

where C_k is a constant. The equation used to solve for K_m in the model is

$$\begin{aligned} \frac{\partial K_m}{\partial t} = & -u\frac{\partial K_m}{\partial x} - v\frac{\partial K_m}{\partial y} - w\frac{\partial K_m}{\partial z} + \frac{C_m^2 l^2}{2K_m}(B+S) \\ & + \left(\frac{\partial}{\partial x^2} + \frac{\partial}{\partial y^2} + \frac{\partial}{\partial z^2} \right) K_m^2 - \frac{C_\varepsilon K_m^2}{2C_m l^2} \end{aligned} \tag{A9}$$

where C_ε and C_m are constants, the length scale l is given by

$$l = (\Delta x \Delta y \Delta z)^{1/3}, \tag{A10}$$

the buoyancy term B is

$$B = -g\frac{K_h}{\theta}\frac{\partial \theta}{\partial z} \quad \text{(unsaturated air)} \tag{A11a}$$

$$B = -gAK_h \frac{\partial \theta_e}{\partial z} + gK_h \frac{\partial q_l}{\partial z} \quad \text{(saturated air)} \qquad \text{(A11b)}$$

where q_l is liquid water mixing ratio, θ_e is equivalent potential temperature, and A is given by

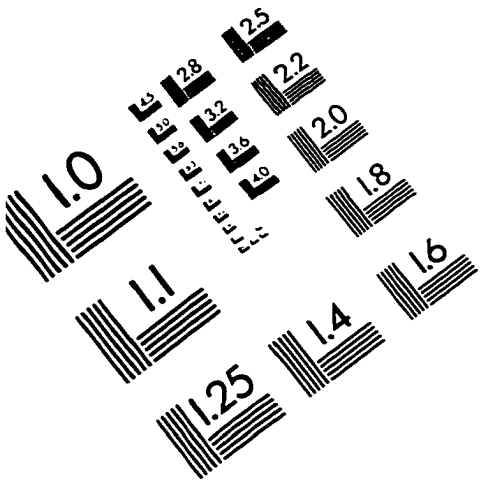
$$A = \frac{1}{\bar{\theta}} \left(\frac{1 + \frac{1.61 \varepsilon L q_v}{R_d T}}{1 + \frac{\varepsilon L^2 q_v}{C_p R_d T^2}} \right). \qquad \text{(A12)}$$

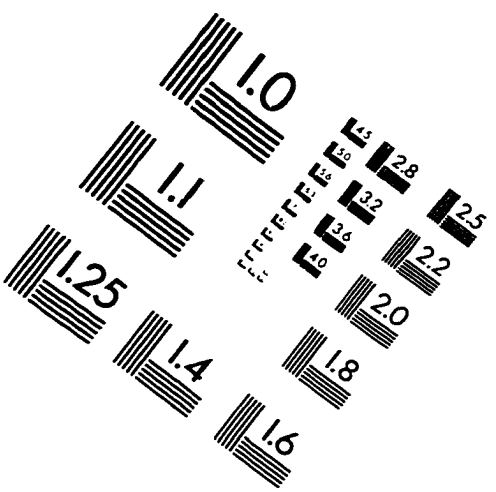
where R_d is the gas constant for dry air. The shear term S in (A9) is given by

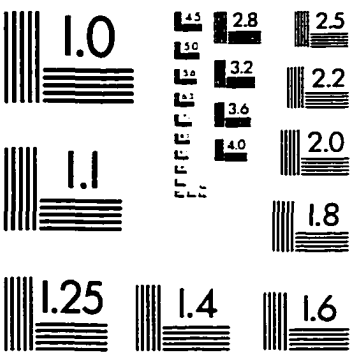
$$S = K_m \left[\left(\frac{\partial u}{\partial x} \right)^2 + \left(\frac{\partial v}{\partial y} \right)^2 + \left(\frac{\partial w}{\partial z} \right)^2 + \left(\frac{\partial v}{\partial x} + \frac{\partial u}{\partial y} \right)^2 + \left(\frac{\partial w}{\partial x} + \frac{\partial u}{\partial z} \right)^2 + \left(\frac{\partial w}{\partial y} + \frac{\partial v}{\partial z} \right)^2 \right]. \qquad \text{(A13)}$$

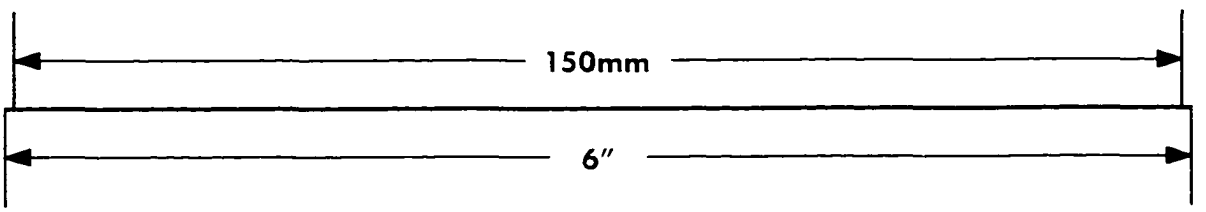
The values of all constants are listed in Table 3.1.

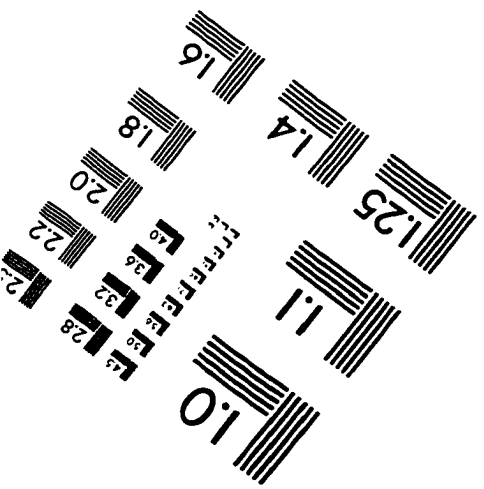
IMAGE EVALUATION
TEST TARGET (QA-3)

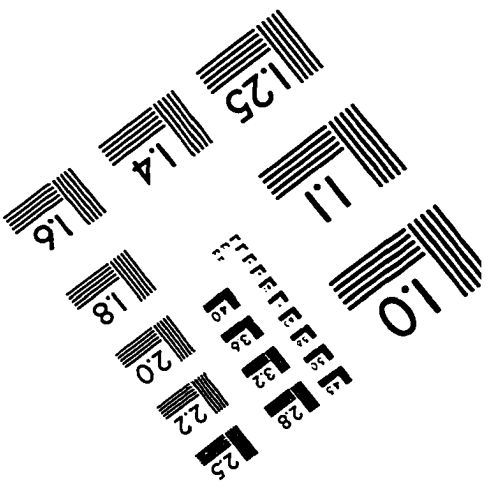












APPLIED IMAGE, Inc
1653 East Main Street
Rochester, NY 14609 USA
Phone: 716/482-0300
Fax: 716/288-5989

© 1993, Applied Image, Inc., All Rights Reserved